



**Università  
degli Studi  
di Ferrara**

**DOTTORATO DI RICERCA IN  
"SCIENZE DELL'INGEGNERIA"**

**CICLO XXXV**

**COORDINATORE Prof. Stefano Trillo**

***Mechanical Properties  
Characterization and Improvement  
of Fused-Filament-Fabricated Parts***

Settore Scientifico Disciplinare ING-IND/22

**Dottorando**

Dott. Malagutti Lorenzo

**Tutore**

Prof. Mollica Francesco

Anni 2020/2022







## ABSTRACT

Fused Deposition Modeling (FDM) or Fused Filament Fabrication (FFF) is the most popular 3D printing technique for thermoplastics. Initially used to produce prototypes of limited size, FFF can also be used for small-scale production and parts of larger size. In this case, a single screw extruder is recommended, fed with polymer pellets and equipped with a wider nozzle. The main advantages are higher flow rates, which in turn reduce the printing time, and greater versatility in terms of available materials at a lower price. The most common materials are also used in this Ph.D. thesis and are poly-lactic acid (PLA) and acrylonitrile butadiene styrene (ABS).

When using FFF for structural applications, the mechanical properties are lower than those of parts obtained by injection molding, due to the inevitable presence of voids and poor filament-to-filament welding properties. The goal of this Ph.D. project is to study the mechanical properties of 3D-printed parts, and possibly to find ways to improve them. Characterization strategies using different materials and techniques were employed in order to measure the mechanical properties of the materials.

In the first part of the work, an experimental 3D printer was developed and built. It is completely open-source and fully customizable with a build volume of 700mm x 700mm x 900mm in X, Y, and Z, respectively. This was used to print some samples and can be used as a test bench for future developments.

In the second part, the mechanical properties in bending of 3D-printed parts as a function of the bead volume were investigated, using a semicrystalline PLA as a model material. Three thermocouples were placed within the specimen during printing, and showed that bead size influenced crystallinity through a complex thermal history that is consequent of the printing process. Such differences in crystallinity distribution affected the mechanical properties directly: unexpectedly, though, more amorphous specimens exhibited higher mechanical properties, with the exception of stiffness.

In the third part, 3D-printed specimens were printed and characterized in tension using PLA filled with wood fibers as a model material. Young's modulus and strength of 3D-printed specimens were measured and successfully modeled using Classical Lamination Theory (CLT). Characterization started from unidirectional specimens, and then moved to different quasi-isotropic lay-ups that were tested for CLT validation. Predicted values were

in good agreement with the measured ones, especially if a contour line correction was applied.

In the last part two novel post-processing methods were described and tested for mechanical properties improvement. The first consists of compaction and remelting within a mold made of fine salt. Mechanical properties in tension were measured, using wood flour-filled polyester as a model material. Void reduction and an enhancement of the quality of bead-to-bead welding were found. Despite the longitudinal properties had a very limited increase, the transversal properties increased significantly, reaching the longitudinal ones, thus leading to a more isotropic behavior. This process, though, has limitations, such as dimensional distortion and a reduction in the thickness of the samples, which is proportional to the eliminated porosity.

The second post-processing method is a copper electroplating process that must be preceded by a treatment to make the material electroconductive, and this consisted of a thin layer of polypyrrole deposition. To evaluate the effectiveness, ABS samples were used. Mechanical properties in bending were measured and a significant increase in the rigidity and the maximum sustainable load was found. However, this technique also has disadvantages, such as a non-uniform plating and a significant increase in weight, especially for small parts.

# TABLE OF CONTENTS

## TABLE OF CONTENTS

<b>INTRODUCTION .....</b>	<b>1</b>
<b>1. BACKGROUND .....</b>	<b>3</b>
1.1 Additive Manufacturing .....	3
1.1.1 Main phases of AM process .....	3
1.1.2 AM Technologies .....	4
1.1.3 Benefits and drawbacks of 3D printing .....	7
1.2 FFF (filament and pellet).....	9
1.2.1 Parameters .....	10
1.2.2 Materials .....	14
1.2.3 Applications.....	17
1.2.4 Limitations and processing problems .....	18
1.3 Pellet extruder .....	19
1.3.1 Components and process.....	19
1.4 Classical lamination theory (CLT) .....	21
1.4.1 Types of laminate: .....	22
1.4.2 Theory .....	23
1.4.3 Unidirectional lamina characterization.....	28
1.4.4 Contour correction .....	29
<b>2. EXPERIMENTAL LARGE FRAME 3D PRINTER .....</b>	<b>32</b>
2.1 Building of the 3D printer .....	32
2.2 Results .....	37
2.3 Conclusions .....	38
<b>3. THERMAL HISTORIES DEPENDENCIES IN A 3D-PRINTED PLA PART .....</b>	<b>39</b>
3.1 Experimental .....	40
3.1.1 Materials .....	40
3.1.2 Compression molding samples.....	40
3.1.3 3D printing .....	41
3.1.4 Quasi-static bending test .....	45
3.1.5 Thermocouple measurements in 3D printed object .....	45
3.1.6 Differential Scanning Calorimetry (DSC) .....	46
3.2 Results .....	49
3.2.1 Set and measured unitary bead .....	49
3.2.2 DSC.....	50
3.2.3 Thermal history .....	55

3.2.4 Bending tests.....	58
3.3 Conclusions .....	61
<b>4. MATHEMATICAL MODELLING THROUGH CLT OF 3D PRINTED PLA FILLED WOOD SAMPLES ...</b>	<b>62</b>
4.1 Experimental.....	62
4.1.1 Filament material .....	62
4.1.2 3D Printing .....	62
4.1.2.1 3D Printer .....	62
4.1.2.1.1 Calibration test .....	63
4.1.2.2 3D printing parameters.....	63
4.1.3 Digital Image Correlation (DIC) .....	64
4.1.4 Quasi-static tensile test .....	65
4.1.5 Testing equipment.....	66
4.1.6 Density measurements.....	67
4.2 Results of tensile test and CLT validation .....	68
4.3 Conclusions .....	71
<b>5. COMPACTION AND REMELTING .....</b>	<b>72</b>
5.1 Experimental.....	73
5.1.1 Filament material and instruments .....	73
5.1.2 Remelting procedure .....	73
5.1.3 Compression molding part.....	74
5.1.4 Quasi-static tensile test .....	75
5.1.5 3D printing .....	75
5.2 Results .....	76
5.3 Conclusions .....	80
<b>6. COPPER ELECTROPLATING POST-PROCESS OF 3D-PRINTED PART.....</b>	<b>81</b>
6.1 Copper electroplating process .....	82
6.1.1 Faraday's law.....	84
6.2 Experimental.....	85
6.2.1 Materials and instrumentations.....	85
6.2.2 3D printing .....	85
6.2.4 Electroplating process.....	88
6.2.5 Quasi-static bending test .....	90
6.3 Results .....	91
6.3.1 ABS as printed with 100% infill.....	91
6.3.2 ABS plated with 100% infill .....	93
6.3.3 ABS with variable raster infill .....	95
6.3.3 Plated ABS with variable raster infill .....	97



6.4 Conclusions .....	100
<b>7. GENERAL CONCLUSIONS AND FUTURE PERSPECTIVES.....</b>	<b>101</b>
<b>REFERENCES .....</b>	<b>103</b>
<b>APPENDIX A.....</b>	<b>109</b>
<b>APPENDIX B.....</b>	<b>113</b>

## LIST OF TABLES

Table 1. Classification of the AM processes .....	5
Table 2. Parameters present in Ultimaker Cura and their subdivision in category .....	10
Table 3. Classification of infill patterns and their features .....	12
Table 4. Chamber, bed, and extruder reference temperature for each different material .....	15
Table 5. Bill of materials of 3D printer .....	33
Table 6. Geometric parameters for each sample type .....	44
Table 7. DSC thermal cycles .....	47
Table 8. Measured geometric parameters for each printed sample .....	50
Table 9. The processing parameters to print various samples. ....	63
Table 10. List of tested laminates and their characteristics, the standard deviation is indicated in parenthesis .....	64
Table 11. Experimental results of the tensile tests on the filament and lay-ups and the contour line corrected values that are used for laminates characterization. The numbers in parenthesis represent standard deviation .....	69
Table 12. The seven independent parameters that characterize the unidirectional lamina .....	70
Table 13. Comparison between experimental data, and predictions of classical lamination theory, including contour correction .....	71
Table 14. List of tested laminates and their characteristics, the standard deviation is indicated in parenthesis .....	75
Table 15. Processing parameters to print various samples .....	86
Table 16. Experimental results of the bending tests on the as-printed laminates with 100% infill density: Young's modulus, strength and strain at break. The numbers in parenthesis represent standard deviation .....	92
Table 17. Density and voids of the as-printed laminates with 100% infill density at different raster angle. The numbers in parenthesis represent standard deviation .....	92
Table 18. Experimental results of as-printed and post-processed unidirectional 0° and 90° laminates with 100% infill density: Young's modulus, strength, strain at break and weight. The numbers in parenthesis represent standard deviation .....	94
Table 19. Experimental results of the bending tests on the as-printed laminates with different infill density percentage: Rigidity, maximum load, displacement at break and weight. The numbers in parenthesis represent standard deviation .....	96
Table 20. Experimental results of the bending tests on the post-processed laminates with different infill density percentage: Rigidity, maximum load, total weight and copper weight. The numbers in parenthesis represent standard deviation .....	98

## LIST OF FIGURES

Figure 1. Steps required for AM process. ....	3
Figure 2. The evolution of 3D printing techniques: resolutions and compatible materials [10] .....	4
Figure 3. Schematic representation of a typical FFF setup .....	9
Figure 4. Several types of infill pattern, direction and density .....	12
Figure 5. Different types of build plate adhesion: Raft, skirt, brim. ....	13
Figure 6. Classification of 3D printing thermoplastic .....	14
Figure 7. Extruder components and zones of the screw .....	19
Figure 8. Different types of laminates.....	22
Figure 9. Reference system of laminate and laminae.....	23
Figure 10. Cross-section of the laminate.....	25
Figure 11. Algorithm of ULF: inputs are in yellow parallelograms, instructions in blue rectangles, conditionals in green diamonds .....	28
Figure 12. Definition of “lamina”, “laminata”, “layer” and “lay-up” .....	30
Figure 13. CAD of 3D printer frame.....	34
Figure 14. Cross-section of aluminum profile (45mm x 135mm) .....	34
Figure 15. 3D printer during printing.....	35
Figure 16. Wiring diagram of 3D printer .....	36
Figure 17. Measurements of bead width and cube along directions x,y, and z .....	37
Figure 18. Cube during and after printing .....	37
Figure 19. High degree of crystallinity and amorphous compression molded specimens .....	41
Figure 20. 3D pellet extruder robot arm during printing.....	42
Figure 21. Customized extruder printing path.....	43
Figure 22. Thermocouples locations in the middle cross-section of the sample .....	45
Figure 23. Schematic representation of the 2 thermal protocols applied on pellets a) with different cooling rates, b) with different isothermal temperatures and c) the thermal protocol applied on compression moulded and 3D printed sample.....	48
Figure 24. Idealized bead cross-section .....	49
Figure 25. Degree of crystallinity on pellets depending on thermal protocol A.....	51
Figure 26. Degree of crystallinity on pellets depending on thermal protocol B.....	52
Figure 27. Crystallinity on 3D printed samples at T1, T2, T3 measured through thermal protocol C .....	53
Figure 28. The cross sections of the various 3D printed samples for each BS.....	54
Figure 29. Thermal histories T1, T2, T3 during printing until cooling down for (a) N3_BS2.9; (b) N5_BS9.1; (c) N5_BS13.4; (d) N8_BS60.2.....	56
Figure 30. Stress vs strain curves for compression molded samples and a selection of 3D printed specimens .....	58
Figure 31. Mechanical properties for compression molded and 3D printed samples at different BS. a) Young’s modulus, b) Stress at break and c) strain at break.....	59
Figure 32. Hardware DANTEC 3D Q-400.....	64
Figure 33. Samples painted for DIC acquisition.....	65
Figure 34. Testing machine INSTRON 4467 .....	66
Figure 35. Balance Mettler model AE 420 and Adventure PRO AV4102C .....	66
Figure 36. Micrometre Mitutoyo 293.....	67
Figure 37. Representative tensile test of the wood flour filled filament and 3D-printed lay-ups.....	68
Figure 38. Post-process procedure.....	74
Figure 39. Compression molded specimens of PLA filled with wood .....	74
Figure 40. Representative tensile test of the post-processed laminates and compression molded sample .....	76

Figure 41. Young Modulus and stress at break of each laminate both post-processed and as printed and compression molded samples. The error bars represent the standard deviation. ....	77
Figure 42. Histogram of the density for each laminate and compression molded samples. The error bars represent the standard deviation. ....	77
Figure 43. Fracture surface of a quasi-isotropic specimen: (a) as printed (b) post-processed.....	78
Figure 44. Tensile test comparison between post-processed and as printed of the lay – ups: a) unidirectional 0° , b) Quasi – isotropic and (c) unidirectionally 90° .....	79
Figure 45. Electrolytic cell: components and reactions .....	82
Figure 46. Anycubic i3 Mega S 3D printer .....	86
Figure 47. Polymerization of Py in PPy .....	87
Figure 48. Sample as-printed and coated with a layer of PPy .....	88
Figure 49. Electrolytic cell .....	89
Figure 50. 3D-printed electroplated part .....	90
Figure 51. Representative stress-strain of the as-printed laminates with 100% infill at different raster angle .....	91
Figure 52. Representative stress-strain of as-printed and post-processed unidirectional 0° and 90° laminates with 100% infill density .....	93
<i>Figure 53. Representative load-displacement of the as-printed laminates with different infill density percentage and raster angle of 45° .....</i>	<i>95</i>
Figure 54. Laminates with different infill density from 30% to 70% .....	96
Figure 55. Representative load-displacement of the post-processed laminates with different infill density percentage and raster angle of 45° .....	97
Figure 56. Cross-section of plated laminates at different infill density percentage .....	98
Figure 57. Top and bottom surface of plated laminates at different infill density percentage .....	99





## INTRODUCTION

Among additive manufacturing technologies (AM), fused deposition modeling (FDM) or Fused Filament Fabrication (FFF) is one of the most common. FFF shows great technological advantages and is a viable alternative for both industry and research centers thanks to the possibility to build objects with complex shapes, with no need to use molds, thus allowing manufacturing at a reasonable price and speed. In this process, a thermoplastic polymer filament is extruded at a temperature above its glass transition or melting temperature through a nozzle and deposited layer-by-layer to form the final object. The use of a slicing software is necessary, in which all the parameters are divided into three macro-categories [1] named extruder-related, process-related, and structural parameters.

The FFF process is not straightforward to understand and shows also several drawbacks: a spool of filament costs up to 10 times more than thermoplastic pellets of the same material, the dimensional accuracy is about 0.1mm but the major drawback, if this technology is used for industrial production, is the limited mechanical properties of the 3D-printed parts compared to injection molded ones. A 3D-printed object necessarily presents voids and poor mechanical characteristics of filament-to-filament welding. In this work, the way the main printing parameters influence the mechanical properties has been studied, and then two post-process methods have been developed to increase the performance of 3D-printed parts obtained by FFF.

A large experimental 3D printer has been developed and built to print some samples and can be used as a test bench for future developments. It is completely open-source and fully customizable with a build volume of 700mm x 700mm x 900mm in X, Y, and Z, respectively.

The mechanical properties in bending of 3D-printed parts as a function of the bead volume have been investigated, using a semicrystalline PLA as a model material and different nozzle diameters. In fact, not only the structural parameters category but also extruder-related and process-related can influence the mechanical properties of the 3D-printed object. Different bead volumes affect the thermal history of the 3D printed part, which in turn for a semi-crystalline material can greatly vary the mechanical properties.

The mechanical properties of the printed object are anisotropic and highly dependent on processing parameters. FFF 3D printed parts can be thought of as laminates and modeled using classical lamination theory (CLT), considering a raster-filled layer as a unidirectional

---

lamina. Mechanical properties can be predetermined using CLT and in this work, both stiffness and strength are studied.

To increase the performance of 3D-printed parts obtained by FFF two post-processing methods have been developed and tested. The first one consists in compaction and remelting of the object in fine powdered salt. The second method is copper electroplating of a 3D-printed part. To evaluate the effect of these post-process methods, the properties have been evaluated on the samples obtained by compression molding, filament, and 3D-printed parts. The mechanical properties have been determined through quasi-static tensile and bending tests, to evaluate Young's modulus, strength, and strain at break.

The thesis is organized as follows:

- In Chapter I the FFF process, the features of a pellet extruder, and the classical lamination theory (CLT) will be described.
- In Chapter II the build of an experimental large 3D printer with a build volume up to 700mmx700mmx900mm in X, Y, and Z, respectively, will be described.
- In Chapter III the effect of the bead volume on the mechanical properties of PLA parts built with a large-scale robot 3D printer will be explained
- In Chapter IV the complete characterization in terms of Young's modulus and strength of a 3D-printed part using the CLT will be proposed
- In Chapter V the evaluation of a novel post-process that consists in two phases, compaction and remelting, will be presented
- In Chapter VI the study of plated 3D-printed parts through copper electroplating will be described
- In Chapter VII general conclusions are summarized and discussed



# CHAPTER I

## 1. BACKGROUND

### 1.1 Additive Manufacturing

Additive manufacturing (AM), also known as 3D printing or rapid prototyping, is a technology used to create three-dimensional objects by depositing layers one by one based on computer-aided design (CAD) [2, 3, 4]. Originally developed for the fabrication of prototypes, now it is becoming more and more interesting also for industrial batches of small scale that do not justify investments in expensive tools [5]. AM changes completely the way parts are built and thanks to the freedom of shapes that can be obtained, new types of objects that are difficult or impossible to make with other manufacturing techniques can be created, revolutionizing the way objects are thought.

The pioneer of 3D printing is Chuck Hull [6], who invented the stereolithography process in the 1980s while working for the company 3D Systems Corp. In this process, a liquid photopolymer is used and through a laser it is selective photopolymerized creating a layer. Among all AM techniques for thermoplastics, fused deposition modeling (FDM), also known as fused filament fabrication (FFF), is the most common one, mainly due to its simplicity and the inexpensiveness of the printing apparatus.

#### 1.1.1 Main phases of AM process

Despite there are quite a few AM techniques, all of them share a similar pathway for creating an object. The main steps [7] are listed in Fig. 1.

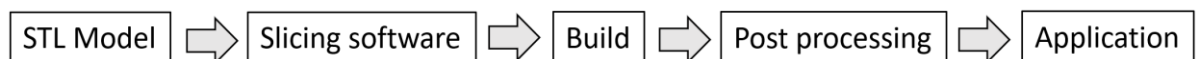


*Figure 1. Steps required for AM process.*

The starting point of each AM process is a 3D geometric model, typically in Stereo Lithography interface format (STL), which describes the external closed surface and can be exported from any CAD software. Many CAD softwares are available for this aim e.g. commercial ones such as SolidWorks, Catia, Inventor, or open-source like OpenSCAD. When the reconstruction of an existing real object is needed, a previous step called Reverse Engineering (RE) is required, which consists in obtaining a geometric model from the real part by acquiring the points belonging to the surface of the real part. This is possible by

using 3D scans or Coordinate Measuring Machines (CMM). The STL file is then input into a slicing software (or CAM software). In the slicing software, the user must set up properly the printing parameters, such as build parameters, the temperature of the process, energy source, timings, speed, etc. This software generates a G-Code file that is sent to the printer, containing all the instructions that the machine must follow to build the 3D object. Once the part is reproduced, it is removed from the machine, and it is ready for post processing, that consists of simple operations such as removing support structures, and surface finishing like sanding or vapor smoothing or painting to decrease the surface roughness [8]. In some cases, more advanced operations are required like thermal treatments, and milling operations to ensure geometrical tolerances. After post-processing, the 3D printed part can be tested in its application and if not suitable, it can be redesigned, re-printed, and tested in a short period of time.

### 1.1.2 AM Technologies

AM techniques are based on additive deposition layer by layer but have also some important differences in the manufacturing method. The evolutions of 3D printing techniques are reported in Fig. 2 since its birth in 1986. Among the different classifications of AM processes, the one proposed by ASTM Committee is chosen and classified the AM processes into seven areas [9], which are reported in Tab. 1 and described below. Each process can achieve its accuracy and uses a starting material in different forms such as liquid, solid filament and powder, as reported in Fig. 2.

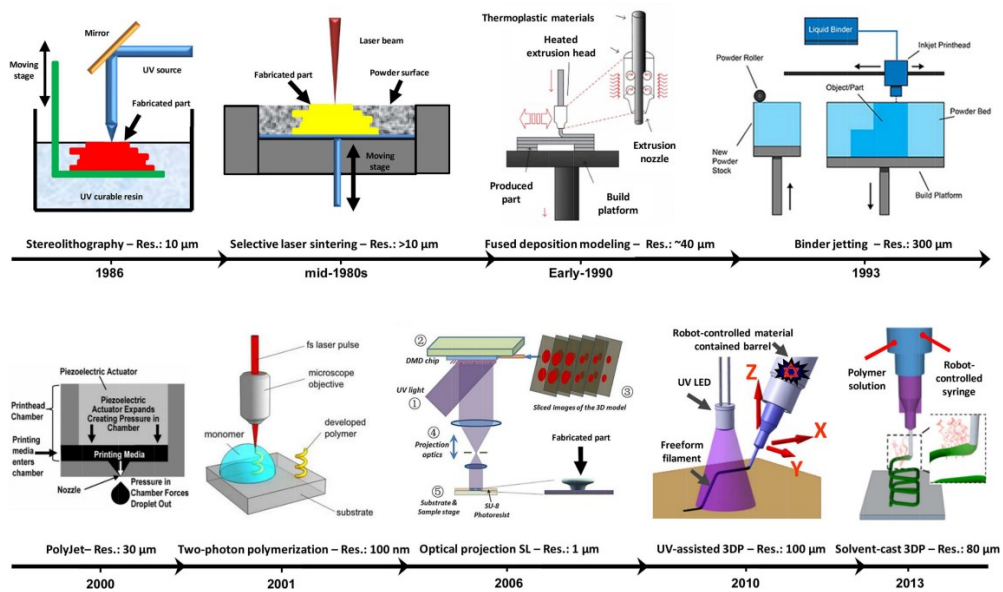


Figure 2. The evolution of 3D printing techniques: resolutions and compatible materials

[10]

*Table 1. Classification of the AM processes*

<b>Process</b>	<b>Related technologies</b>
Material Extrusion	Fused Filament Fabrication (FFF)
Vat Photopolymerization	Stereolithography (SLA), Masked stereolithography (MSLA), Digital light processing (DLP), Continuous liquid interface production (CLIP)
Sheet Lamination	Laminated object manufacturing (LOM), Ultrasonic Additive Manufacturing (UAM)
Powder Bed Fusion	Selective laser sintering (SLS), Electron beam melting (EBM)
Material Jetting	Multi-jet modeling (MJM)
Binder Jetting	Powder bed and inkjet heat (PBIH)
Directed Energy Deposition	Laser metal deposition (LMD)

- 1. Material extrusion:** this is one of the most common processes of AM, also known as FFF. This was trademarked by Stratasys Inc., and hence the separate FFF is used to avoid copyright infringement issues. FFF is an extrusion-based 3D printing technique that utilizes thermoplastics as printing materials. The details of FFF will be described in Section 1.2.
- 2. Vat photopolymerization:** is the other most common process and includes different technologies according to the type of light source and the interface between the vat and the resin, such as stereolithography (SLA), mask stereolithography (MSLA), digital light processing (DLP), and continuous liquid interface production (CLIP). The process consists of a vat filled with liquid photosensitive polymeric resin. The resin is exposed to UV light and the geometry of the object to be printed is traced out. The exposed resin hardens forming a solid layer and this continues till the complete object is finished.

- 
3. **Sheet lamination:** includes two types of manufacturing techniques, ultrasound additive manufacturing (UAM) and laminated object manufacturing (LOM). In UAM sheets of metal are welded together using ultrasonic welding, while sheets of paper and adhesives are used in LOM. Objects 3D printed with LOM can only be used for aesthetical purposes.
  4. **Powder bed fusion:** in this technique powdered material is molten to additively build 3D objects. Powder-bed fusion process uses a laser or an electron beam to sinter the powdered materials. After the first layer is hardened, the powder dispensing unit spreads a new layer of powder onto the build platform and the process is repeated until the 3D part is obtained.
  5. **Material jetting:** photosensitive polymer in the form of liquid droplets is dispensed from multiple printheads and hardens on exposure to UV light thereby building the part layer-by-layer. This process builds parts with high dimensional accuracy and is also capable of full-color printing.
  6. **Binder jetting:** powder bed 3D printing technique, developed by Emanuel Sachs at Massachusetts Institute of Technology in the 1990s. The binder jetting uses the liquid adhesive to selectively deposit to join powder particles. After each layer, the build chamber drops down and a new layer of powder is spread on top of the previous layer and the printhead again traces the cross-section of the object and binds the previous and current layer together until the part is completed.
  7. **Directed energy deposition:** is used for 3D printing metals like Titanium and Cobalt Chrome alloys. A wire is fed through a nozzle and an electron beam projector, focusing thermal energy, and fusing the feed as it moves across while tracing the cross-section of the object. This is repeated until the part is printed.

---

### 1.1.3 Benefits and drawbacks of 3D printing

Additive manufacturing can revolutionize most of today's business, minimize materials and energy and compress supply chains [6]. Below, a list of some benefits of AM technology [10] is reported:

- Freedom of form: novel geometries that are impossible to achieve using another manufacturing process can be 3D-printed, leading to new engineering performance.
- Part optimization and light-weighting: due to the ability to create a complex part, through a topological simulation, the material can be placed into the object only where it is needed to support the load. In this way, a lighter part can be obtained. Thanks to the nature of the process also the number of components in a product can be reduced, meaning less labor and time required for assembly.
- Customized product: AM allows parts that can be 3D printed on demand and fully customizable. In fact, unlike other manufacturing techniques, with AM the same piece with different details can be produced with very low effort reducing the need for stockpiles and complex supply chain.
- Reduced time to market: prototypes and successive iterations can be produced without expensive tools or molds, drastically decreasing cost and accessibility to manufacture items.
- Lower material and energy waste: AM reduces energy use by 25% and cuts waste and material costs by up to 90% compared to traditional manufacturing methods [11].

Despite there are quite a few benefits in 3D printing technologies, there are also some drawbacks, and a list is reported below:

- Time: Objects produced through 3D printing technology take much longer time than traditional techniques such as injection molding due to the nature of the process. Based on the parts to be printed and their characteristics, there are additive techniques that are more suitable and faster than others.
- Price of feedstock material: concerning resins and filaments, it can range from tens of euros up to hundreds for technical materials for each kilo of material, while for powder is around 100 – 200 euro. Compared to injection molding, the cost of the raw material plays an important role in the price of the product.

- 
- Range material: not all metals and plastics can be temperature controlled enough to print a good part (e.g. PET for FFF). Many of these cannot be recycled and very few are food safe, also due to the porosities that are inevitable in the 3D printing process.
  - Part structure: a 3D printed part is produced layer by layer, so a weld is present between each layer that can break, leading to a delamination. This phenomenon is more present in the parts printed with FFF technology.
  - Dimensional accuracy: each process has its own accuracy (Fig. 2), also depending on the type of machine used, so the final part may differ from the CAD one up to 0.1mm – 0.2 mm.
  - Post-processing: 3D printed parts need to remove support material, cleaning and smooth the surface to achieve the required finish. Post processing methods include waterjetting, sanding, a chemical soak and rinse, air or heat drying, assembly and others.
  - Volumes of production: 3D printing are more cost effective in prototypes or in small batch production, due to a lower initial investment. Once scaled up to large volumes for mass production, the unit cost does not reduce as other conventional technique like injection moulding.

## 1.2 FFF (filament and pellet)

Among AM methods, FFF is one of the most common techniques, due to the continuous decrease of the related costs, in fact, the price of an entry level FFF printer may be as low as 500 euro. Due to its low cost and variety of compatible materials, this technique is very useful for research communities and industries. The basic functioning of FFF is illustrated in Fig. 3 [1]. A thermoplastic filament is continuously fed into a hotend, with a temperature that can be varied depending on the printing material. In the hotend, the plastic melts and then is extruded through a nozzle and deposited layer-wise on a heated bed, following the pattern contained in the G-Code file. The pressure needed to force the filament through the nozzle is given by a mechanical system formed by two opposite rolls, with knurls for a proper filament grip, that are connected to a stepper motor. With a direct drive setup, the extruder pushes the filament directly into the hotend. Instead, in a Bowden setup, the extruder is mounted on the printer's frame and pushes filament through a long PTFE tube (called Bowden tube). To obtain a regular flow of material, the extrusion pressure and so the print speed should be maintained as constant as possible during all deposition phases. The FFF printing process depends on a large number of parameters, which are described in Subsection 1.2.1. Commonly, the thermoplastic material is found in the form of filament collected in the spool, but in recent years the interest in 3D printers with pellet extruders is growing and will be described in depth in Section 1.3.

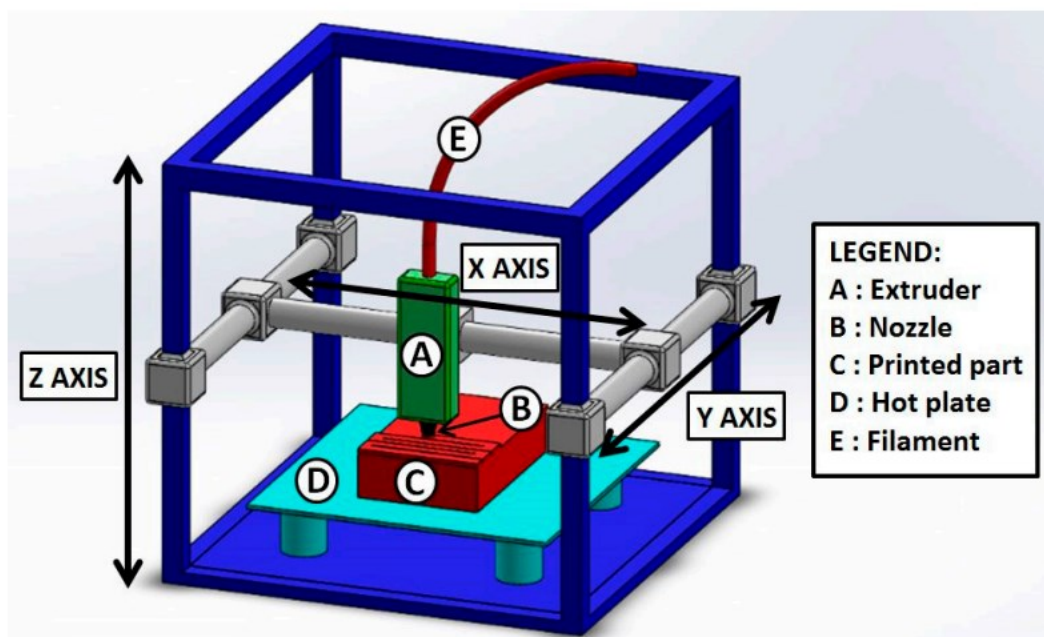


Figure 3. Schematic representation of a typical FFF setup

### 1.2.1 Parameters

FFF is a complicated process containing a large number of parameters. These parameters will influence the part quality and properties (e.g. mechanical properties). FFF can potentially deliver good part quality, safety, low manufacturing cost and short lead time. In order to reach such objectives, proper process parameters must be assessed. On the market there are various types of slicers, some open source and others subject to payment, such as Ultimaker Cura, Simplify 3D, Slic3r, KISSlicer, PrusaSlicer, and Repetier. Among all, Ultimaker Cura is used in this work as it is open source, allowing a wider choice of parameters to set, and has been developed for a longer time with a large community. In Tab. 2 the principal setting parameters and their subdivisions present within Ultimaker Cura are reported.

*Table 2. Parameters present in Ultimaker Cura and their subdivision in category*

<b>Category</b>	<b>Parameters</b>
Quality	Layer height Line width
Shell	Wall thickness Top/bottom layers Zseam
Infill	Infill density Infill pattern infill line direction Infill overlap
Material	Printing temperature build plate temperature Flow
Speed	Print speed Travel speed
Travel	Retraction Z Hop
Cooling	Enable print cooling Fan speed
Support	Generate support
Build plate adhesion	Build plate adhesion type
Dual extrusion	
Mesh fixes	
Special modes	Print sequence Spiralize outer contour
Experimental	



For simplicity, these can be grouped into three macro-categories [1] that are described below:

1. **extruder-related:** these are parameters of the hardware, i.e., nozzle and filament diameters. In filament 3D printers the nozzle diameter is between 0.4mm – 1.2mm while in pellet extruders it can be up to 20mm. Usually, the filament diameter is either 1.75mm or 2.85mm.
2. **process-related:** These parameters are present in the material, speed, and cooling categories of Tab. 2. Based on the material to print, the different temperatures must be set both for the extruder and the heated build plate. Other important parameters are the fan, travel, and print speed. Print speed is the speed when the melt flows through the nozzle, while travels when there is no extrusion of molten plastic. It can also regulate the fan speed to obtain a better adhesion between two consecutive layers or to allow overhangs.
3. **structural parameters:** these are the most important parameters and can greatly affect the mechanical properties. These parameters belong to the quality, shell, and infill categories and are listed below:
  - Layer height: the thickness of the layer deposited by the nozzle.
  - Line width: the width of a deposited bead.
  - Wall thickness: the thickness of the wall in the horizontal direction; it should be a multiple of the line width.
  - Top/bottom layers: number of top or bottom layers, which can have settings that are different from the other layers.
  - Infill density: the density of the infill of the print. It ranges between 0% and 100%. Usually, a good compromise between mechanical and aesthetic properties is around 20% – 30%.
  - Infill pattern: the pattern of the infill. There are several types of patterns and are reported in Tab. 3 and Fig. 4. For each of these patterns the mechanical properties of the object change, thus based on the aim of the part, the right pattern can be chosen.
  - Infill line direction: also called infill angle, specifies the deposition angle of the infill. It is particularly useful if a 3D object that behaves like a composite needs to be created. In fact, the behavior of FFF parts can be modeled using classical lamination theory (CLT) [12, 13].

- Infill overlap: the amount of overlap between infill and walls. A slight overlap allows the infill to be connected better to the walls leading to an increase in strength.

*Table 3. Classification of infill patterns and their features*

<b>Infill pattern</b>	<b>Feature</b>
Grid	
Triangles	Strong 2D
Tri-Hexagon	
Lines	Quick 2D
Cubic	
Octet	Strong 3D
Quarter cubic	
Concentric	
Cross	Flexible 3D
Cross 3D	
Gyroid	

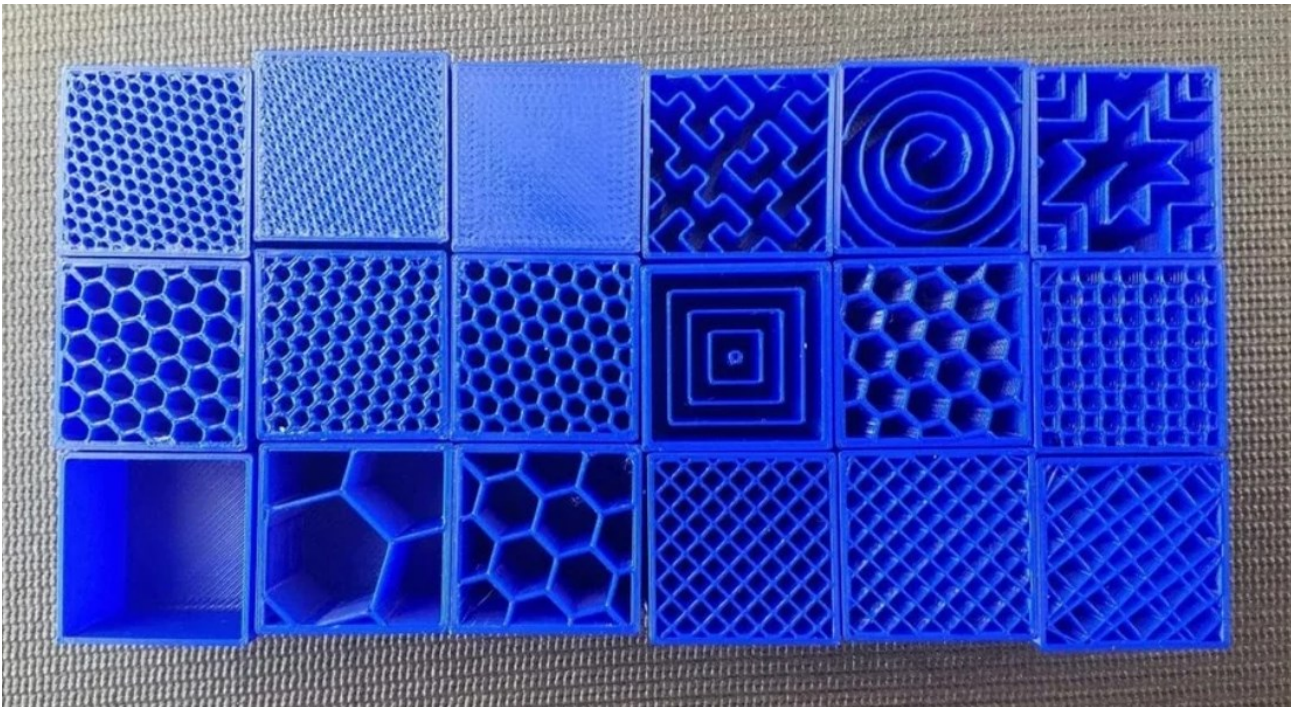


*Figure 4. Several types of infill pattern, direction and density*

The other parameters present in Tab. 2 that don't affect the mechanical properties of 3D printed objects directly but are important for the quality and success of a print are:

- Flow: based on the material, the extruder can be controlled using this parameter to ensure the right flow rate.
- Retraction: extruder retracts the filament when the extruder is moving on a non-printed area.
- Z seam: it is located where the extruder begins to lay a new bead. In each layer multiple Z-seam can be present due to multiple retractions. Preferably, it is positioned in an internal portion of the part to hidden or make it less visible.
- Z hop: when retraction occurs, the build plate is lowered to allow clearance between the nozzle and the printed object.
- Generate support: generate structures to support parts of the model which have overhangs. Can be controlled the gap between the part and the supports to allow a better detachment. Without these structures, the overhang part of the object can collapse during printing.
- Build plate adhesion type: different options that help to print the first layer are pictured in Fig. 5. Raft adds a thick grid with a roof below the model and helps with warping and stabilizing models with small footprints. A skirt is a line or more printed around the model but not connected to it and it is useful because it primes the filament establishing a smooth flow. Brim adds a single layer flat area around the base of the model to hold down the edges of 3D printed part, which can prevent warping and help with bed adhesion.
- Print sequence: if multiple parts are present on the build plate, it can be chosen to print all models one layer at a time or wait for one part to finish before printing the next.
- Spiralize outer contour: when a model with only one single perimeter contour must be printed, if this parameter is activated, a steady Z increase over the whole print is created.

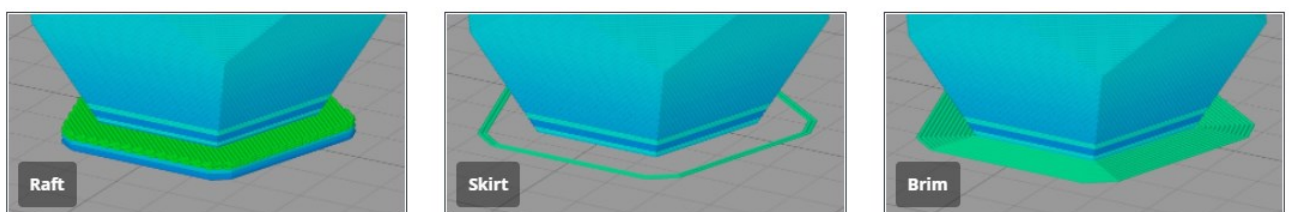


Figure 5. Different types of build plate adhesion: Raft, skirt, brim.

The dual extrusion category is used when two extruders are installed on the printer. One extruder has the material of the final part while the other one is for the support material.

In the category of mesh fixes we can control the meshes of the object if it is formed by too many points, the resolution can be decreased, and it is particularly useful when a big 3D pellet printer is used. The latter, unlike the filament ones, does not allow quick control of the flow rate and for this reason during the path of the extruder abrupt/strong accelerations should be avoided.

In the experimental category, there is a series of features that can be tested but their function is not fully assured.

### 1.2.2 Materials

One of the key advantages of FFF is the wide range of thermoplastic materials that can be processed. Thermoplastic polymers are formed by linear or slightly branched chains, not linked to each other by strong bonds, therefore it is sufficient to increase the temperature to bring them to a viscous state and thus be able to be printed it. This operation can't be performed with thermosetting polymers.

There are several polymeric materials available for FFF and selections are dependent on the general properties to be achieved. A classification of 3D printing thermoplastic based on structure (semicrystalline or not), mechanical properties and hardware required to print it, are reported in Fig. 6.

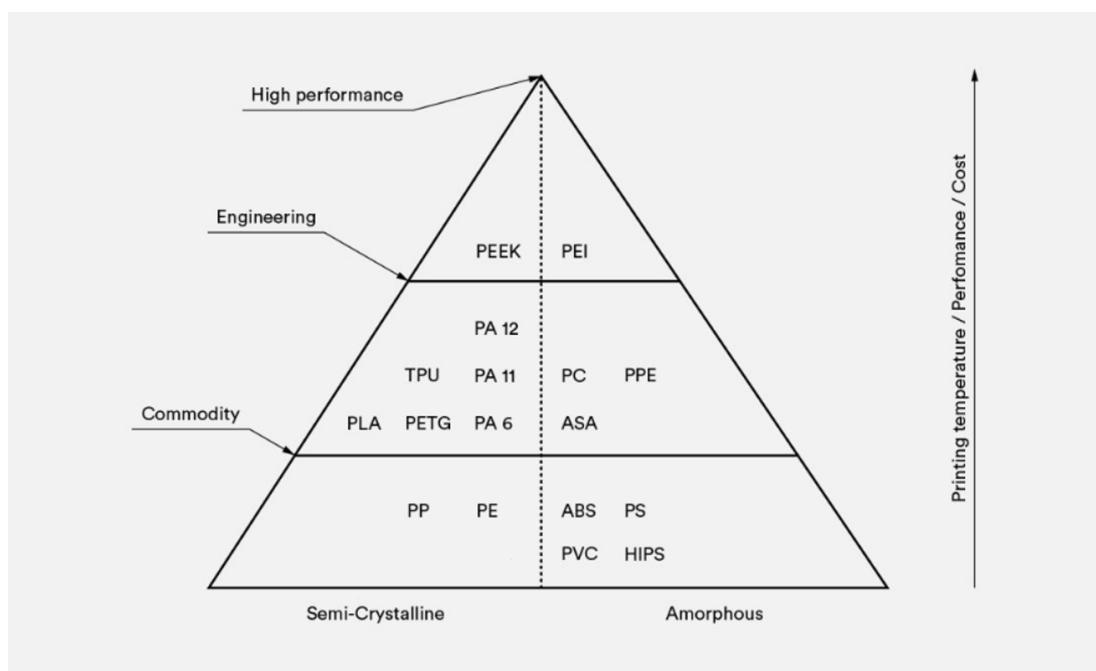


Figure 6. Classification of 3D printing thermoplastic

Poly(lactic acid) (PLA) and acrylonitrile butadiene styrene (ABS) are the most common printable materials, among the engineering material there are polyamides (PA), thermoplastic polyurethanes (TPU), Acrylonitrile styrene acrylate (ASA), and Polyethylene terephthalate glycol modified (PETG) while high-performance thermoplastics include Polyetheretherketon (PEEK) and Polyetherimide (PEI). A reference for extruder, bed, and chamber temperature is reported for each material in Tab. 4. Moving from common to technical materials, the required temperatures increase as the cost of the printer to be able to print those materials. In fact, for some materials a heated chamber is required to obtain the best possible result. When working with amorphous or semicrystalline materials like PEI, ASA, ABS, or PEEK, it is important to keep the environment surrounding the material at optimal temperature. In many cases, the optimal temperature for the heated chamber is close to the  $T_g$  of the polymer being printed, ensuring a steady cool down, and avoiding some issues, like internal stress that led to lower mechanical properties and warping effects.

*Table 4. Chamber, bed, and extruder reference temperature for each different material*

Material	Temperature (°C)			
	Chamber	Bed	Extruder	
Semicrystalline	PLA	/	50 - 60	190 - 220
	PP	/	85 - 115	240 - 260
	PA	/	70 - 90	220 - 260
	TPU	/	60	210 - 240
	PETG	/	70 - 90	220 - 250
	PEEK	120 - 150	120 - 160	360 - 450
Amorphous	ABS	70 - 80	90 - 110	220 - 260
	HIPS	/	90 - 115	220 - 240
	ASA	110	90 - 110	220 - 250
	PC	/	120 - 150	260 - 310
	PEI	100	120 - 160	360 - 390

---

Below the materials that can be 3D printed with their features are listed:

- 1. Polylactic acid (PLA):** is the most common material used in desktop FFF printers. It is a bio-based plastic material, commonly made from renewable agriculture-based materials like corn starch. The monomer is usually made from fermented plant starch. This material is a thermoplastic aliphatic polyester. PLA is a compostable thermoplastic polymer consisting of renewable raw materials. PLA plastic material is easy-to-use and offers some interesting mechanical properties. It is very easy to print, and low cost but has low heat resistance, is very brittle, and is prone to oozing.
- 2. Acrylonitrile butadiene styrene (ABS):** is another common 3D printing material and it is used also for industrial parts. It is a tough material with medium mechanical properties, and it can warp during printing. To prevent the last problem, it should be printed with a heated chamber to maintain the temperature constant around the print.
- 3. Polyethylene terephthalate glycol modified (PETG):** is accessible, easy to print, and has slightly better properties than PLA and ABS. In particular, it's stronger than PLA, and warps less than ABS, in fact, due to its sticky nature offers one of the best adhesions between layers among all materials. It is used for prototyping but also for functional parts, so it covers a wide range of applications.
- 4. Thermoplastic polyurethane (TPU):** is very flexible and it is used where impact resistance or shock absorption is required. It isn't an easy material to print because it can break and clog often due to its fragility and it is recommended to print it with a direct extruder.
- 5. Polyamide (PA):** called also Nylon is very strong and impact resistant, owing to its flexibility. Two common FFF Nylon types are Nylon 6, and Nylon 12 and exhibit great strength and suit many applications. It's very hygroscopic, so it must always be dried before and during printing to avoid hydrolysis. Nylon 3D printing materials are often used to create strong prototypes, as well as for creating high-performance parts like gears, hinges, screws, and some parts in which a bit of flexibility is required.
- 6. High impact polystyrene (HIPS):** is the ideal support material for ABS because it has similar properties, prints at similar temperatures, and can also be dissolved away in limonene leading to parts with few surface finish imperfections.
- 7. Acrylonitrile styrene acrylate (ASA):** is very similar to ABS, with almost identical print settings, but has better mechanical properties and environmental resistance. It's more expensive than ABS but it is more durable and lasts longer, in fact, it can be used for outside applications because is UV-resistant.

- 
- 8. Polycarbonate (PC):** has high mechanical properties and it is temperature resistant. Polycarbonate is commonly used to 3D print engineering parts, as well as other accessories where strength is important. These materials usually are filled with additives that change their properties, making them particularly useful for industrial needs like chemical resistance, high impact strength, biocompatibility, and thermal stability.
  - 9. Polyetheretherketone (PEEK):** it is the most expensive material for 3D printing and can cost up to 600 euro/kg, it is very difficult to print and only with very expensive 3D printers. It is used for high-strength part production for industrial and medical applications, and is particularly useful in the metal replacement process and offers a better strength-to-weight ratio than aluminum.
  - 10. Polyetherimide (PEI):** it has good thermal stability and is temperature resistant, at a temperature above 200°C. It is difficult to print but requires a lower printing experience than PEEK. PEI is commercially known as ULTEM, and it is highly resilient and resistant to many chemicals.

### 1.2.3 Applications

The main application of FFF in the industry is rapid prototyping. It is very important to perform a preliminary form and fit evaluation directly from the 3D model. Many engineers like to create sample prototypes to validate their work before creating the actual product. In the last years, due to a new, fast, and precise process, FFF can be used also to obtain the final products.

The most important applications [14] are reported below:

- Aerospace: the potentiality in the aircraft industry is mainly due to the low volume of production and the possibility of printing complex components that with traditional manufacturing must be separated into smaller parts and then assembled.
- Automotive: FFF cannot compete with the traditional methods for mass production but is used more and more frequently for high-end, specialized automobile components such as Formula 1 race cars.
- Custom orthodontics, prosthesis, and other biomedical parts: using 3D scan data it is possible to create customized biomedical objects. For example, since traditional prosthetics are heavy, costly, and take a long time to be manufactured, FFF 3D printed prosthetics are largely seen as a revolution.

- 
- Household items or gifting: They can easily design, iterate, redesign and print a part according to their needs and requirements. Additionally, the FFF 3D printed parts can also be post-processed in multiple ways which helps in creating aesthetically appealing products.

#### **1.2.4 Limitations and processing problems**

Despite the many advantages of FFF for many industrial users, this technology has also some drawbacks, like building speed, accuracy, and materials density. The average layer thickness is in the range of 0.1-0.3 mm, and the higher level of resolution (about 0.040 mm) can only be provided by the highly-costing machines and with longer build times. For these reasons FFF is inefficient in mass production and provides a surface of the model with more roughness than traditional technologies such as injection molding. The cost of an FFF printed part is higher than an injection molded one due to the time to build it layer by layer, and also the cost of the raw material. The dimensional accuracy is about 0.1mm based on different printing parameters used in the slicing software. Some fillers can add to the material to increase dimensional stability after solidification, decrease the shrinkage, and reduce the cost of the filament. During printing, several types of undesired processing problems could occur such as clogging, not sticking to the build plate, extrusion flow, string or oozing, overheating, layer shifting, warping, and cracking.

An important consideration when printing with FFF is to consider the build orientation. The biggest issue is the mechanical properties of the 3D-printed parts. Even at 100% infill, stiffness and strength are relatively low, if compared to parts obtained by injection molding [15, 16], and this is due to the poor bead-to-bead welding and presence of voids. The mechanical properties of the printed object are anisotropic and highly dependent on processing parameters. The FFF parts usually behave as isotropic in the XY plane, but when deposited microfilaments along with a particular direction preferentially, they behave as anisotropic. Moreover, the strength of FFF parts builds in Z-direction is lower than those in the XY plane [17, 18, 19]. For this reason, the major stress axes of the 3D printed part must be oriented in the XY plane rather than in the Z direction. The adhesion between layers is possible because the material is in a range of temperatures where molecular movement is allowed leading to thermal diffusion of the adjacent layers inside the printed object. For successful bonding, accurate control of the thermal environment, around the glass transition temperature of the material being deposited, is necessary especially for high-grade materials.



### 1.3 Pellet extruder

Although additive manufacturing, and FFF in particular, was borne mainly to produce prototypes of small size, it is gaining more and more market shares for parts of larger size [20]. In this case, it is beneficial to substitute the classical filament extruder with a single screw extruder that is fed with polymer pellets and has a larger nozzle (e.g. of a few millimeters diameter) mounted as the extruder die [21]. With a pellet extruder, larger flow rates are achievable, reducing printing time. Moreover, pellets are cheaper than filaments and offer greater versatility in terms of printable materials. On the other hand, with larger nozzles, it can be difficult to respect tolerances [22]. To solve this problem, the part can be printed slightly larger and then trimmed at the right geometrical measure through a CNC mill.

#### 1.3.1 Components and process

The main components of an extruder [23] are reported in Fig. 7 and listed below:

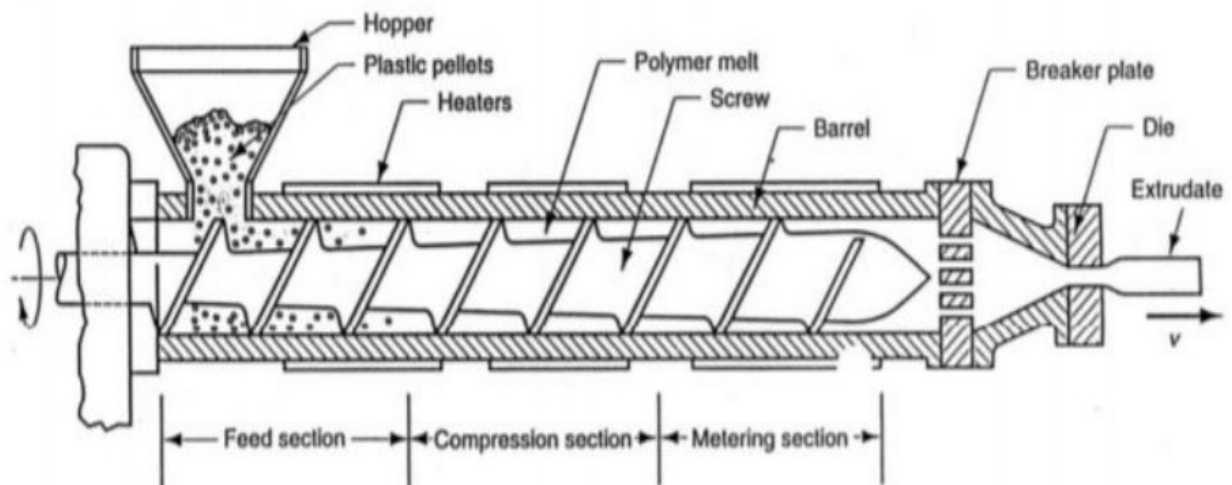


Figure 7. Extruder components and zones of the screw

1. **Drive system:** can be direct or indirect and it is used to transfer motor power to the screw. A direct drive system uses a gearbox while an indirect one runs with pulleys. The thrust bearing is located between the screw shaft and the drive output shaft, and its load is proportional to the head pressure and the screw diameter.
2. **Hopper:** this is where the pellet is fed and often maintained warm. To minimize heat transfer from the barrel a good insulator barrier and a water-cooling system are

---

installed between the barrel and the feed section. The feeding system can be of two types. Flood fed, in which the feeding zone is full of pellets and the flow rate is proportional to the RPM of the extruder screw. Starve fed, in which the pellets in the feeding zone are regulated by an auger. Here, the pellets mass flow rate is determined by the velocity of the feeder screw.

3. **Barrel:** are fabricated from strong carbon steel and the surface is hardened with post-treatment, such as nitriding, or with a bi-metallic coating. Heaters are present around the barrel to heat it, and they can be of three different types: mica, ceramic, and cast. To better control the temperature also fans are present, usually one for each heater, and if it is not sufficient, cooling can be done through oil or water.
4. **Screw:** it is the most important part that allows the melt of polymer pellets, and in the simple case is divided into three zones:
  - a) Feeding or solid conveying zone: the pellets are pushed forward by the rotation of the screw, so it works like an auger. Geometrically is characterized by constant pitch and channel depth. It can also be shown that the pressure acting on the granules, by friction, grows exponentially, but in a way that is still quite bland. The material starts slowly to melt, but the largest percentage is still in the solid state. In this area, therefore, it presents a pre-heating of pellets. Specifically, heat exchange is absent in the first two threads present below the hopper, independent of the screw pitch. Subsequently, the heat exchange becomes greater, and a phase of preheating occur, which leads to the formation of the first layer of the molten film above the solid group.
  - b) Melting zone: unlike the previous one, the channel depth of the screw decreases its section from the start to the end of this zone, so the part in which the polymer moves is reduced, increasing consequently the frictional forces on the solid material that starts to melt. The ratio between feed and meter depth is the compression ratio and each polymer has its recommended ratio. The material should start to melt before the melting zone as it may cause the block of the extruder. There is also a gradual reduction of the volumetric flow rate that, due to the melting of the plastic material, reduces its apparent volume.
  - c) Metering or fluid transport zone: as in the solid conveying zone, the screw has pitch and depth channel of screw constant and equal to the final values of the compression zone. Here, the material is completely melted and is

---

processed to homogenize its characteristics, in particular the necessary pressure is created to extrude the molten polymer through the filter and die.

- 5. Die:** is the last component of an extruder and its section determines the shape of the extrudate and usually for 3D printer it is circular.

The main processing variables are screw rotation speed and barrel temperature. The main geometric variables are the screw diameter  $D$ , the screw length  $L$ , the ratio  $L/D$ , the compression ratio, and the screw height of the end of the feeding zone.

#### **1.4 Classical lamination theory (CLT)**

Even at 100% infill, mechanical properties are relatively low, if compared to parts obtained by injection molding, and this is due to the inevitable presence of voids [24, 25] and the poor mechanical characteristics of the filament-to-filament welding. Moreover, mechanical properties are maximum along the printing direction and minimum in all directions that are normal to the printing direction, thus the material is transversely isotropic [24]. Moreover, anisotropy increases in the case of materials that are filled with reinforcement fibers, as these tend to align preferentially in the printing [1, 17, 26]. For these reasons, the behavior of FFF parts have been modeled using classical lamination theory (CLT) [13, 14], that are typical for composite materials: a raster filled layer can be considered like a unidirectional lamina and therefore FFF parts can be thought of as laminates. The first paper in which CLT was applied to FFF parts is due to Kulkarni and Dutta [27]. Here, it was found that CLT is effective in predicting stiffness for several polyamide lay-ups, and the same holds also for ABS [28, 29, 30] and poly-lactic acid (PLA) [31]. CLT works well also for the case of short [32, 33] and continuous [34, 35] carbon fiber-reinforced polymers, and even in the case of bi-material parts [36, 37].

**1.4.1 Types of laminate:**

The sequence of packing or lay-up of the laminate is specified through a conventional designation, in which the orientations of the different layers are reported in the order in which they appear along the thickness. There are several notable cases, and they are reported below and pictured in Fig. 8:

- Symmetric: for each lamina with orientation  $\vartheta$  there is another with the same orientation in a symmetrical position with respect to the middle plane. The subscript S is used after indicating half of the lamina. In the case that the middle plane crosses a lamina, this is indicated with a line on this lamina.
- Antisymmetric: for each lamina with inclination  $+\vartheta$  there is another  $-\vartheta$  in a symmetrical position concerning the middle plane. The subscript Q is used after indicating half of the laminae.
- Balanced: for each lamina with orientation  $+\vartheta$  there is another with orientation  $-\vartheta$  in any position.
- Cross ply: laminates consisting of an alternation of laminae at  $0^\circ$  and  $90^\circ$ .
- Angle ply: laminates consisting of an alternation of laminae with orientation at  $+\vartheta$  and  $-\vartheta$ .
- Quasi-isotropic: laminates consisting of six or more identical orthotropic laminae, which are oriented at the same angle relative to adjacent laminae. It is a laminate which behaves like an isotropic material if it is loaded in the plane.

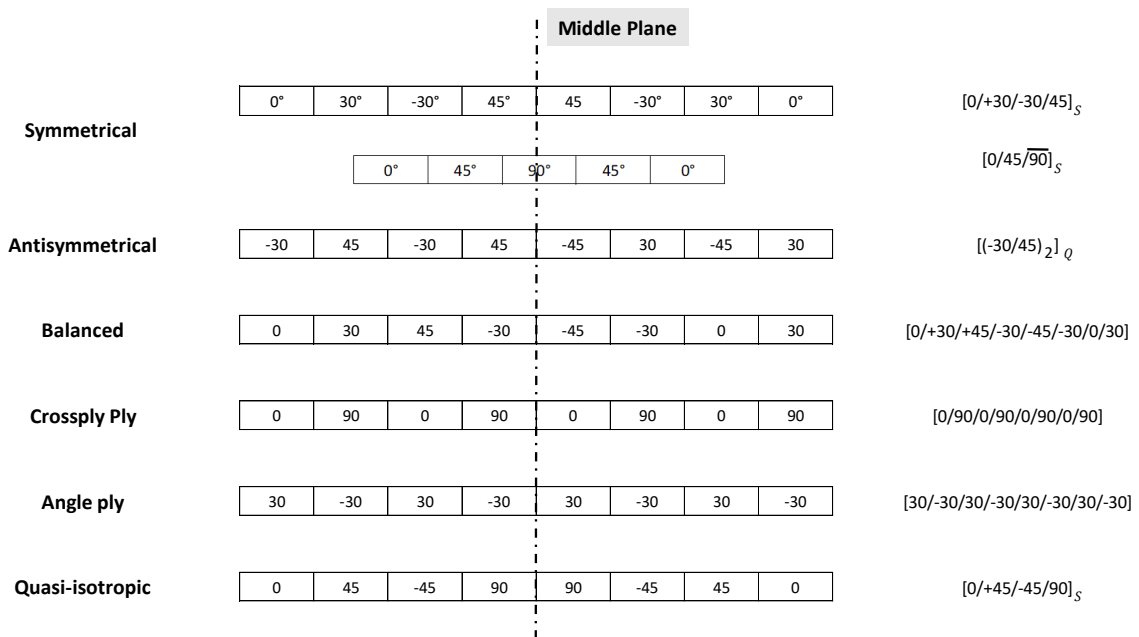


Figure 8. Different types of laminates

### 1.4.2 Theory

In this chapter, we will briefly describe the CLT. In this work some simplifying hypotheses on laminate deformation kinematics and on the stress state of the individual laminae, that greatly reduce the mathematical treatment are applied and listed below:

- Perfect adhesion between laminae
- laminate is supposed to be constituted by orthotropic unidirectional laminae
- thickness of each lamina  $t$  is constant and very small if compared to width and length, therefore only a plane stress loading will be considered
- Each layer follows Hooke's law, so the material is linearly elastic
- Small displacements
- Theory of Kirchoff-Love, so transverse shear deformation is considered negligible.

Transverse shear stresses are eliminated on surfaces of the plate defined by  $z = \pm \frac{t}{2}$

The reference system of a lamina is considered  $(x_1, x_2, x_3)$  where  $x_1$  is directed along the fiber direction,  $x_2$  lays on the plane of the lamina and oriented in the transverse direction, and  $x_3$  is normal to the plane of the lamina. This reference system just described differs from the laminated reference system  $(x, y, z)$ , and is rotated by an angle  $\vartheta$ , as shown in Fig. 9.

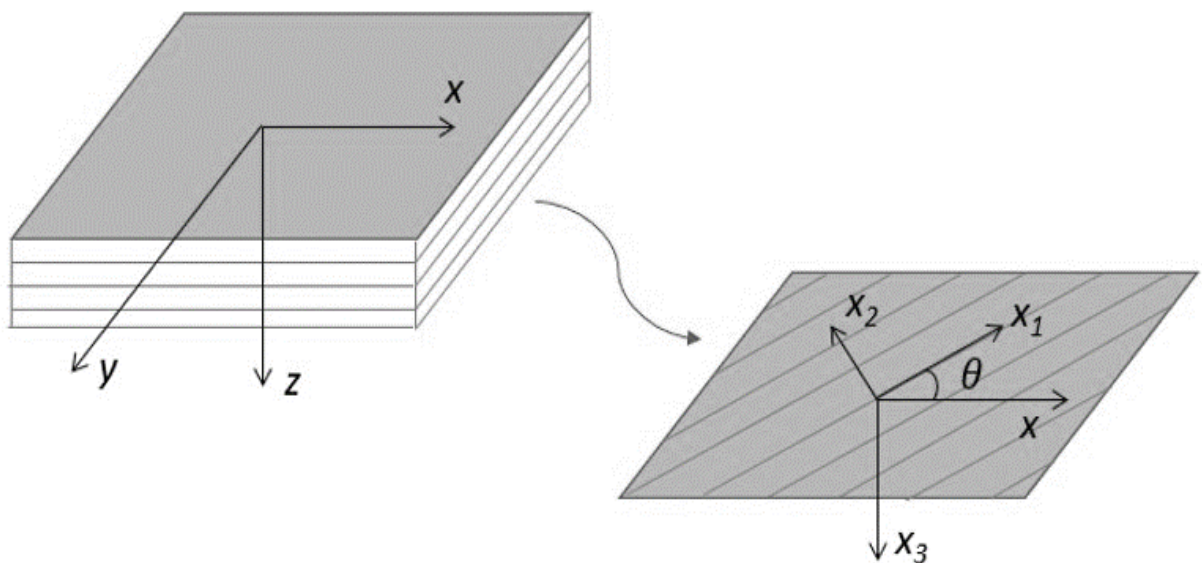


Figure 9. Reference system of laminate and laminae

The stress state of the single lamina is related to the state of deformation by the Eq. (1-1):

$$\{\sigma\} = [Q]\{\varepsilon\} \quad (1-1)$$

Applying a state of plane stress, the Eq. (1-1) becomes Eq. (1-2):

$$\begin{Bmatrix} \sigma_1 \\ \sigma_2 \\ \sigma_6 \end{Bmatrix} = \begin{bmatrix} Q_{11} & Q_{12} & 0 \\ Q_{12} & Q_{22} & 0 \\ 0 & 0 & Q_{66} \end{bmatrix} \begin{Bmatrix} \varepsilon_1 \\ \varepsilon_2 \\ \varepsilon_6 \end{Bmatrix} \quad (1-2)$$

Where  $\sigma_1, \sigma_2$  and  $\varepsilon_1, \varepsilon_2$  are normal stresses and deformations in direction  $x_1, x_2$ , respectively. Instead,  $\sigma_6$  and  $\varepsilon_6$  represent the shear stress and deformation in the plane.

The matrix  $[Q]$  is the stiffness of the laminae and can be written in the form of engineering constants, as reported below:

$$Q_{11} = \frac{E_1}{1-\nu_{12}\nu_{21}}, \quad Q_{22} = \frac{E_2}{1-\nu_{12}\nu_{21}}, \quad Q_{12} = \frac{\nu_{12}E_2}{1-\nu_{12}\nu_{21}}, \quad Q_{66} = G_{12}, \quad \nu_{21} = \nu_{12} \frac{E_2}{E_1} \quad (1-3)$$

In which  $E_1$  and  $E_2$  are the Young's moduli in the longitudinal direction  $x_1$  and transversal direction  $x_2$ , respectively.  $G_{12}$  is the shear modulus and  $\nu_{12}$  and  $\nu_{21}$  are coefficient of Poisson.

According to CLT, all laminae will be subject to the same strain state  $\{\varepsilon_x, \varepsilon_y, \varepsilon_s\}$  in the laminate reference system, consisting of normal deformations in the directions, x and y, and engineering shear deformation in the XY plane, respectively. All laminae are made of the same material, but may be rotated in their plane by a generic angle  $\vartheta$  concerning the x direction; considering the generic k-th lamina, Eq. (1-2) in the reference system of the laminate becomes Eq. (1-4):

$$\begin{Bmatrix} \sigma_x \\ \sigma_y \\ \sigma_s \end{Bmatrix}^k = \begin{bmatrix} Q_{11}^\vartheta & Q_{12}^\vartheta & Q_{16}^\vartheta \\ Q_{12}^\vartheta & Q_{22}^\vartheta & Q_{26}^\vartheta \\ Q_{16}^\vartheta & Q_{26}^\vartheta & Q_{66}^\vartheta \end{bmatrix}^k \begin{Bmatrix} \varepsilon_x \\ \varepsilon_y \\ \varepsilon_s \end{Bmatrix} \quad (1-4)$$

Where the stiffness matrix  $[Q^\vartheta]$  depends on the angle  $\theta$  and the stiffness matrix  $[Q]$  by following system of equations (1-5):

$$\begin{aligned} Q_{11}^\vartheta &= Q_{11} \cos^4 \vartheta + Q_{22} \sin^4 \vartheta + 2(Q_{12} + 2Q_{66}) \cos^2 \vartheta \sin^2 \vartheta \\ Q_{22}^\vartheta &= Q_{11} \sin^4 \vartheta + Q_{22} \cos^4 \vartheta + 2(Q_{12} + 2Q_{66}) \cos^2 \vartheta \sin^2 \vartheta \\ Q_{12}^\vartheta &= (Q_{11} + Q_{22} - 4Q_{66}) \cos^2 \vartheta \sin^2 \vartheta + Q_{12}(\cos^4 \vartheta + \sin^4 \vartheta) \\ Q_{16}^\vartheta &= (Q_{11} - Q_{12} - 2Q_{66}) \cos^3 \vartheta \sin \vartheta - (Q_{22} - Q_{12} - 2Q_{66}) \sin^3 \vartheta \cos \vartheta \\ Q_{26}^\vartheta &= (Q_{11} - Q_{12} - 2Q_{66}) \cos \vartheta \sin^3 \vartheta - (Q_{22} - Q_{12} - 2Q_{66}) \sin \vartheta \cos^3 \vartheta \\ Q_{66}^\vartheta &= (Q_{11} + Q_{22} - 2Q_{12}) \cos^2 \vartheta \sin^2 \vartheta + Q_{66}(\cos^2 \vartheta - \sin^2 \vartheta)^2 \end{aligned} \quad (1-5)$$

The axial loads and pure bending per unit length applied to the laminate  $N_x, N_y, N_s, M_x, M_y, M_s$  are related to the midplane strains and curvatures  $\varepsilon^0_x, \varepsilon^0_y, \varepsilon^0_s, k_x, k_y, k_s$  through the Eq. (1-6):

$$\underbrace{\begin{Bmatrix} N \\ M \end{Bmatrix}}_{\text{Stresses}} = \underbrace{\begin{bmatrix} A & B \\ B & D \end{bmatrix}}_{\substack{\text{Stiffness} \\ \text{Matrix}}} \underbrace{\begin{Bmatrix} \varepsilon^0 \\ k \end{Bmatrix}}_{\substack{\text{Strains} \\ \text{Curvatures}}} \quad (1-6)$$

Where  $\{\varepsilon^0\}$  represents the strain vector ( $\varepsilon^0_x, \varepsilon^0_y, \varepsilon^0_s$ ) and  $\{k\}$  the curvature vector ( $k_x, k_y, k_s$ ). The stiffness matrix of the laminate is represented by Eq. (1-7):

$$A_{ij} = \sum_{k=1}^N Q_{ij}^k (z_k - z_{k-1}) = \sum_{k=1}^N Q_{ij}^k t^k \Rightarrow [A] = [MPa \cdot mm]$$

$$B_{ij} = \frac{1}{2} \sum_{k=1}^N Q_{ij}^k (z_k^2 - z_{k-1}^2) \Rightarrow [B] = [MPa \cdot mm^2] \quad (1-7)$$

$$D_{ij} = \frac{1}{3} \sum_{k=1}^N Q_{ij}^k (z_k^3 - z_{k-1}^3) \Rightarrow [D] = [MPa \cdot mm^3]$$

while  $z_k$  is the position of the face to consider in the case for each individual layer, as shown in Fig. 10. In fact, it is necessary to evaluate the top and bottom of each individual layer.

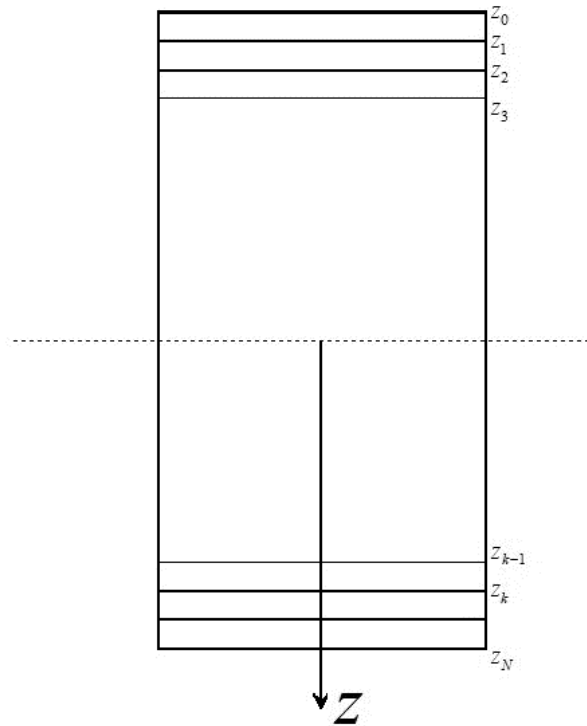


Figure 10. Cross-section of the laminate

Considering the external stresses ( $N, M$ ) and the stiffness matrix known, since it depends only on the characteristics of the material and the orientation of the lamina, reversing the Eq. (1-6) gives the state of deformation of the laminate:

$$\begin{pmatrix} \varepsilon_x \\ \varepsilon_y \\ \varepsilon_z \end{pmatrix} = \begin{pmatrix} \varepsilon_x^0 \\ \varepsilon_y^0 \\ \varepsilon_z^0 \end{pmatrix} + z \begin{pmatrix} k_x \\ k_y \\ k_z \end{pmatrix} \quad (1-8)$$

In the case of tensile test and symmetry of the lamination sequence, only the in-plane laminate stiffness describes the material behavior. This will be indicated with matrix  $[A]$ , and if the laminate is made of  $N$  unidirectional laminae of equal thickness  $t$ , Eq. (1-9) is obtained:

$$[A] = t \sum_{k=1}^N [Q^\theta]^k \quad (1-9)$$

Where the subscript  $k$  refers to  $k$ -th lamina. Thus, Eq. (1-6) can be simplified as follows, obtaining Eq. (1-10):

$$\begin{pmatrix} N_x \\ N_y \\ N_s \end{pmatrix}^k = \begin{bmatrix} A_{11} & A_{12} & A_{16} \\ A_{12} & A_{22} & A_{26} \\ A_{16} & A_{26} & A_{66} \end{bmatrix}^k \begin{pmatrix} \varepsilon_x \\ \varepsilon_y \\ \varepsilon_s \end{pmatrix} \quad (1-10)$$

A quasi – isotropic laminate has characteristics of the laminate that do not vary with the direction of loading concerning the in-plane properties and by definition is symmetric and balanced and must follow Eq. (1-11):

$$A_{11} = A_{22} \quad , \quad A_{66} = \frac{A_{11} - A_{12}}{2} \quad , \quad A_{16} = A_{26} = 0 \quad (1-11)$$

Thus, if the external forces are known, the laminate strains can be found by inverting Eq. (1-10). The stresses for each lamina can then be obtained through Eq. (1-4) and Eq. (1-5), but to use a failure criterion, they must be rotated to the lamina coordinate system through Eq. (1-12):

$$\begin{pmatrix} \sigma_1 \\ \sigma_2 \\ \sigma_6 \end{pmatrix} = \begin{bmatrix} \cos^2 \vartheta & \sin^2 \vartheta & 2 \cos \vartheta \sin \vartheta \\ \sin^2 \vartheta & \cos^2 \vartheta & -2 \cos \vartheta \sin \vartheta \\ -\cos \vartheta \sin \vartheta & \cos \vartheta \sin \vartheta & \cos^2 \vartheta - \sin^2 \vartheta \end{bmatrix} \begin{pmatrix} \sigma_x \\ \sigma_y \\ \sigma_s \end{pmatrix} \quad (1-12)$$

Now, can be applied a failure criterion. The Tsai-Hill criterion has been chosen, which appears to be quite effective also for 3D printed parts (Casavola et al., 2016) and is reported in Eq. (1-13):

$$\frac{\sigma_1^2}{S_L^2} - \frac{\sigma_1 \sigma_2}{S_L^2} + \frac{\sigma_2^2}{S_T^2} + \frac{\sigma_6^2}{S_{LT}^2} \leq 1 \quad (1-13)$$



---

Where  $S_L$ ,  $S_T$ , and  $S_{LT}$  are the strength in the longitudinal direction, transversal direction, and shear, respectively.

Failure of the lamina occurs as the left-hand side of Eq. (1-13) equals or exceeds unity. Considering the Eq. (1-2), Eq. (1-3) and Eq. (1-13), each unidirectional lamina can be completely characterized by 7 quantities that must be evaluated experimentally and they are  $E_1, E_2, \nu_{12}, S_L, S_T, G_{12}$  and  $S_{LT}$ .

Both the first ply failure (FPF) and ultimate laminate failure (ULF) methods can be used. The FPF is more conservative because the laminate breaks as soon as any lamina inside the laminate is broken, regardless of the presence of all the others. So, FPF predicts failure as soon as the weakest ply fails, thus it is typically used for design purposes. In our case, to describe complete laminate failure, ULF must be used, as it considers the failure sequence of all laminae. ULF procedure is pictured in Fig. 11 as an algorithm. The procedure starts with the computation of matrix  $[A]$  given the lamination sequence, the mechanical properties of the single laminae, their thicknesses, and their orientations. Using Eq. (1-10) knowing the external loads, the strains can be calculated. At this point, Eq. (1-4) and Eq. (1-12) can be used to obtain the stresses in each lamina reference frame, i.e.  $\sigma_1, \sigma_2$  and  $\sigma_6$ , which can be substituted into Eq. (1-13) to know whether each lamina fails or not. If no lamina fails, then the external load can be increased, while if some laminae fail, they must be removed from the lamination sequence. In this case, the procedure continues, calculating a new matrix  $[A]$  until no laminae are left. The external load at which the last lamina fails is the ULF load. ULF still underestimates laminate strength because with this algorithm when a lamina breaks it is removed from the laminate but in reality, it is partially able to carry the applied external load.

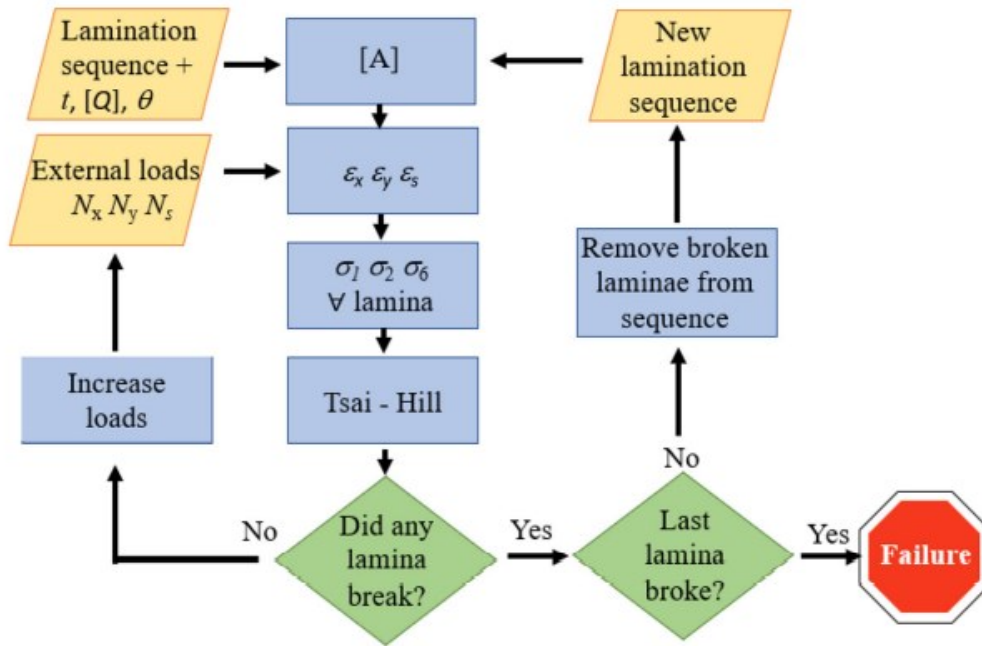


Figure 11. Algorithm of ULF: inputs are in yellow parallelograms, instructions in blue rectangles, conditionals in green diamonds

### 1.4.3 Unidirectional lamina characterization

A 3D printed part is made up of a different sequence of layers. To characterize tensile material, at least three different samples must be tested. In order to evaluate  $E_1$ ,  $\nu_{12}$  and  $S_L$ , is required a 3D printed laminate with the bead deposited along the axes where the load is applied. Instead to measure  $E_2$  and  $S_T$  a laminate with the bead deposited transversal to the axes where the load is applied must be tested. These laminates should be printed and tested according to ASTM D3039 in order to estimate  $E_1$ ,  $E_2$ ,  $\nu_{12}$ ,  $S_L$  and  $S_T$ .

Regarding the shear properties, these can be determined with the symmetric and balanced  $[45/-45]_{2s}$  laminates, in agreement with ASTM D3518. Briefly, if  $E_{45}$  and  $\nu_{45}$  are the Young's modulus and the Poisson's ratio of the  $[45/-45]_{2s}$  laminate, the shear modulus  $G_{12}$  follows Eq. (1-14):

$$G_{12} = \frac{E_{45}}{2(1+\nu_{45})} \quad (1-14)$$

Concerning the shear strength  $S_{LT}$ , assuming that the Tsai Hill criterion is valid, SLT can be obtained once  $S_L$  and  $S_T$  are known. If the tensile strength of the  $[45/-45]_{2s}$  in the x direction is indicated with  $S_{45}$ , it can be shown that as the laminate fractures:

$$\begin{aligned}\sigma_x &= S_{45} \\ \sigma_y &= 0 \\ \sigma_s &= \frac{1}{2} \frac{E_1 - E_2}{E_1 + E_2(1 + 2\nu_{12})} S_{45}\end{aligned}\tag{1-15}$$

and applying Eq. (1-10), Eq. (1-16) is obtained:

$$\begin{aligned}\sigma_1 &= \frac{E_1 + \nu_{12}E_2}{E_1 + E_2(1 + 2\nu_{12})} S_{45} \\ \sigma_2 &= \frac{E_2(1 + \nu_{12})}{E_1 + E_2(1 + 2\nu_{12})} S_{45} \\ \sigma_6 &= \pm \frac{S_{45}}{2}\end{aligned}\tag{1-16}$$

in which  $\sigma_6$  is intended to be negative in the  $+45^\circ$  laminae and positive in the  $-45^\circ$  laminae. Combining Eq. (1-16) with the Tsai-Hill Eq. (1-13), one obtains the value of the only unknown  $S_{LT}$ .

#### 1.4.4 Contour correction

In an FFF 3D printed part, each layer usually has some perimeter lines, indicated in the slicer software as a wall. These enhance the mechanical properties and improve the aesthetic appearance. Hence, a single layer is composed of a raster infill surrounded by the contour lines, as pictured in Fig. 12. The FFF part is then obtained by a sequence of such layers, thus in this work, we will indicate:

- Lamina: The interior unidirectional raster filling.
- Layer: The composition of the lamina together with the contour lines.
- Laminate: is the set of all the laminae.

The contribution of the contour lines can be seen as an additional material arranged in parallel to the whole laminate, which increase the stiffness and strength, as reported by Melenka and Schofield (2015) and by Choi and Kortschot (2020).

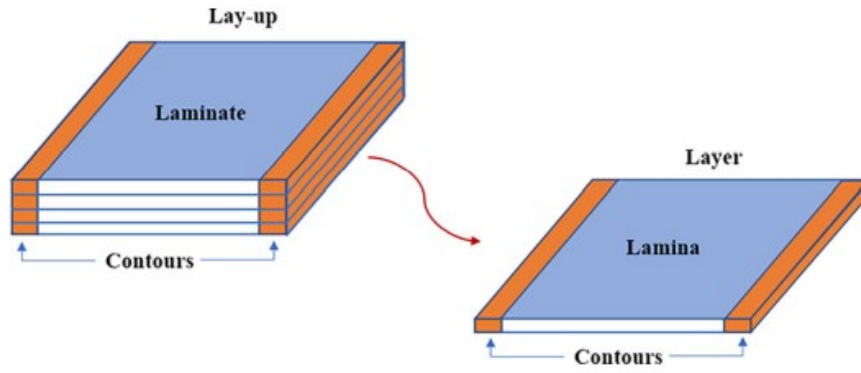


Figure 12. Definition of “lamina”, “laminata”, “layer” and “lay-up”

The same strain is supposed to be applied to the laminate and contour lines, thus the rule of mixtures in parallel can be applied. The Young’s modulus  $E$  and the Poisson’s ratio of the lay-up follow Eq. (1-17) or Eq.(1-18):

$$E = \frac{E_{lam}A_{lam} + E_{con}A_{con}}{A}$$

$$v = \frac{v_{lam}A_{lam} + v_{con}A_{con}}{A} \quad (1-17)$$

Where,  $E_{lam}$  is the laminate modulus,  $E_{con}$  is the modulus of the contour line, which is equal to the longitudinal modulus of the lamina. In Eq. (1-17)  $v_{lam}$  and  $v_{con}$  are the Poisson’s ratio of the laminate and the contour line, respectively. In both equations,  $A$ ,  $A_{lam}$  and  $A_{con}$  represent the lay-up, laminate and contour lines cross-sectional areas, respectively.

$$E = E_{lam} \frac{A_{lam}}{A} + E_{con} \frac{A_{con}}{A} = E_{lam} \Phi_{lam} + E_{con} \Phi_{con}$$

$$v = v_{lam} \frac{A_{lam}}{A} + v_{con} \frac{A_{con}}{A} = v_{lam} \Phi_{lam} + v_{con} \Phi_{con} \quad (1-18)$$

In Eq. (1-18),  $\Phi_{lam}$  and  $\Phi_{con}$  are the volume fraction of the laminate and the contour lines, respectively. In the case of unidirectional  $0^\circ$  lay-ups the correction has no effect.

A similar procedure can be applied to the strength, but here there is a further hypothesis that the ultimate strain of the contours is higher than the laminate, and that failure of the whole specimen occurs as the laminate fractures. The laminate strength  $S_{lam}$  can be obtained and is represented by Eq. (1-19):

$$S_{lam} = E_{lam} \varepsilon_f \quad (1-19)$$

---

Here,  $\varepsilon_f$  the failure strain. if  $S_{con} = E_{con} \varepsilon_f$ , is the stress in the contour lines when the laminate (and lay-up) is about to fracture, applying the rule of mixtures, the lay-up strength  $S$  follows Eq. (1-20):

$$S = \frac{S_{lam}A_{lam} + S_{con}A_{con}}{A} = S_{lam} \left( \phi_{lam} + \phi_{con} \frac{E_{con}}{E_{lam}} \right) \quad (1-20)$$

Eq. (1-20) can be used to obtain the laminate strength  $S_{lam}$ , once the strength of the lay-up  $S$  has been measured.

## CHAPTER II

### 2. EXPERIMENTAL LARGE FRAME 3D PRINTER

A commercial 3D printer with about 1m<sup>3</sup> of build volume that prints non-high-level filament costs at least 15000 up to even 50000 euros. However, even the most expensive ones have limitations such as closed software and a belt system movement, which is unsuitable for supporting equipment with masses of more than a few kg. For these reasons, during the first year of this doctorate, a 3D printer has been developed, in order to overcome these problems. This 3D printer can be used as a test bench for new ideas and equipment such as a pellet extruder. In addition, it can print both small- and large-scale prototypes and products to be used in an industrial environment. This can be achieved by using industrial components and state of the art open-source 3D printing control systems. The different components that are used in the building of the 3D printer are explained in the next chapter.

#### 2.1 Building of the 3D printer

To build the 3D printer all the materials that have been used are reported in the bill of materials (B.O.M) in Tab. 5. A schematic representation of the 3D printer is pictured in Fig. 13 as a CAD model. To build the frame of the 3D printer, aluminium profiles purchased by Dierre (Spezzano di Fiorano, MO), pictured in Fig. 14, with a cross-section of 45mmx135mm have been used. These profiles ensure a maximum displacement in the center of the most stressed profile, the one to which the extruder is mounted, of about 0.02mm with an extruder weight of about 20kg.

Among different types of 3D printer movements, a cartesian one is chosen. It moves components linearly along the X, Y, and Z axes to position the printhead and print within three-dimensional space. Hiwin industrial-grade components have been used both for linear rail and guide and for ball screws and nuts with their bearings. The extruder moves in X and Y for 80cm, while the build plate in Z for 90cm. The build plate can have a dimension up to 70cm x 70cm and consists of a plate of aluminum of 8mm thickness with a heated silicone mat, that heats the surface. NEMA 23 stepper motors are used to move the axes and they have a torque of about 1Nm at 24V.

*Table 5. Bill of materials of 3D printer*

<b>Part no.</b>	<b>Part name</b>	<b>Quantity</b>	<b>Size (mm)</b>
1	Aluminium profiles	20	45x135x1208
2	Corner bracket M6	55	18x40
3	Plate Feet M10	4	45x90
4	Feet M10	4	D=80, H=100
5	Rubber Feet	4	D=80
6	Nuts with spring M6	360	13.5x20
7	All screw, nuts M4,M5,M6	1	M4, M5, M6
8	Ball-screws R16	5	L=1100
9	BK 12 bearings	5	
10	BF 12 bearings	5	
11	Connector shaft flexible	5	L =60, multi-radius
12	Linear guide rail HGR20	8	L=1000
13	Linear guide block HGH20	8	
14	Plate aluminium	1	60x10x6000
15	Plate aluminium	1	140x10x6000
16	Nema 23 motor	5	
17	Power supply	1	
18	Connector power supply	2	
19	Duet 3D mainboard	1	
20	Raspberry pi 4	1	
21	Endstop	6	
22	Bl touch	1	
23	Printer bed surface	1	220x220x5
24	Heated silicone mat	1	200x200
25	Cables and connectors	1	
26	Fan	3	
27	Ethernet cable		L=10000
28	Led strip and driver	2	L=1000
29	Box for electronic	1	700x460x260
30	Magnetothermic	1	
31	Cable tray	2	
32	E3D SuperVolcano hotend	1	
33	Bondtech QR extruder	1	
34	Nozzles	1	0.6 - 1.2 mm
35	Extra and spare parts	1	

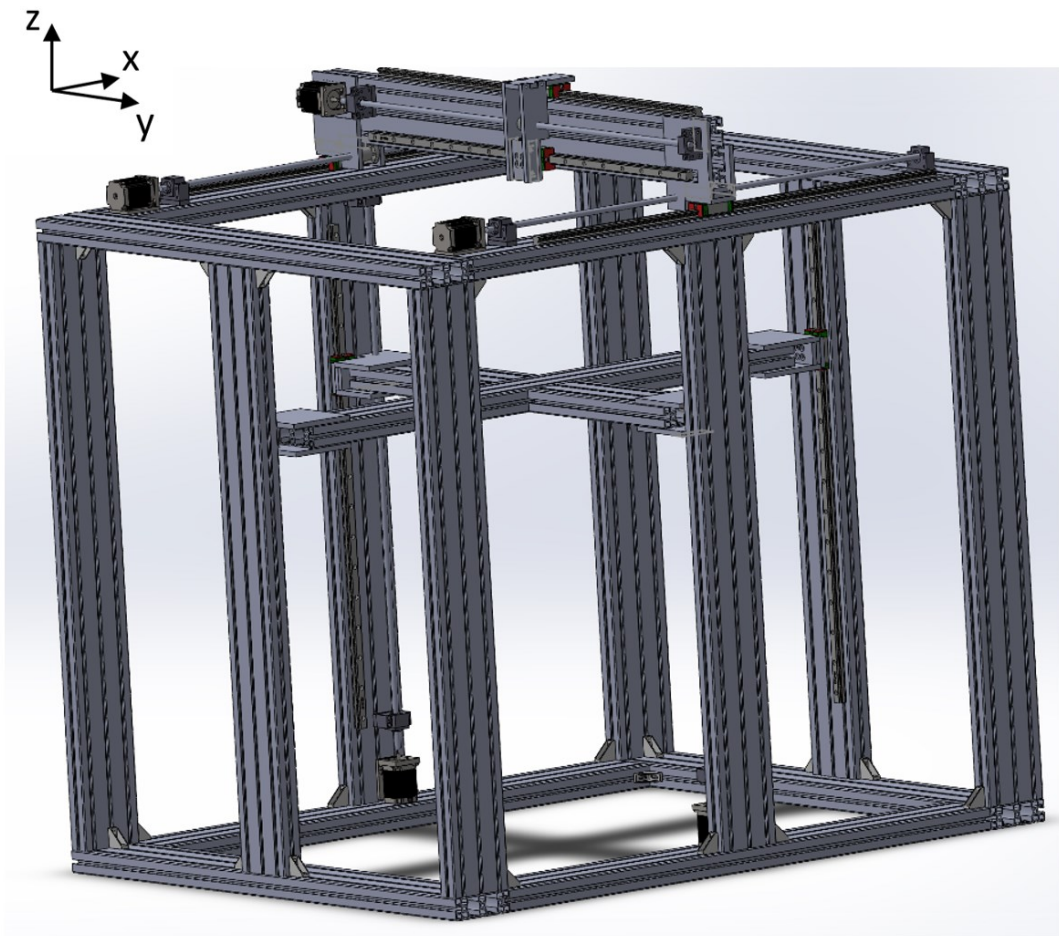


*Figure 13. CAD of 3D printer frame*

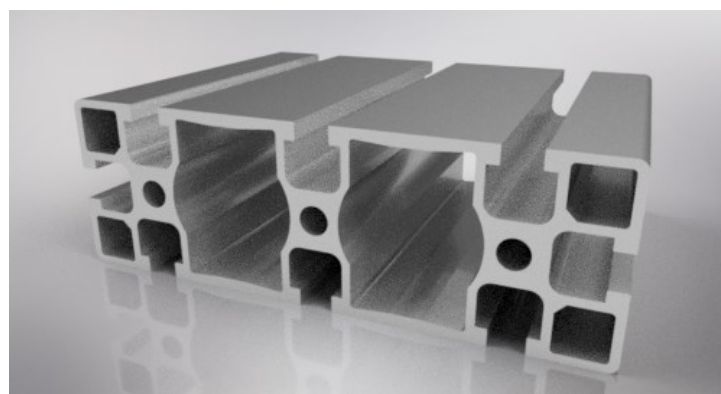


*Figure 14. Cross-section of aluminum profile (45mm x 135mm)*



The printhead consists of a hotend SuperVolcano and an extruder bondtech QR to feed the filament. The SuperVolcano hotend is high performance and can extrude also high-grade materials, such as PEEK. It can mount different nozzle diameters from 0.4mm to 1.2mm depending on the different accuracy of the part to be printed. The printer has also two fans, one to cool down the cold zone of the extruder and the second one to cool down the filament that is being deposited. To fully automate the process, a probe (Bl touch) is mounted on the printhead to perform if needed a mesh bed levelling compensation, therefore if the build plate is not perfectly flat or horizontal, the first layer will be well deposited anyway. The 3D printer with a build plate of 22cm x 22cm is shown in Fig. 15.

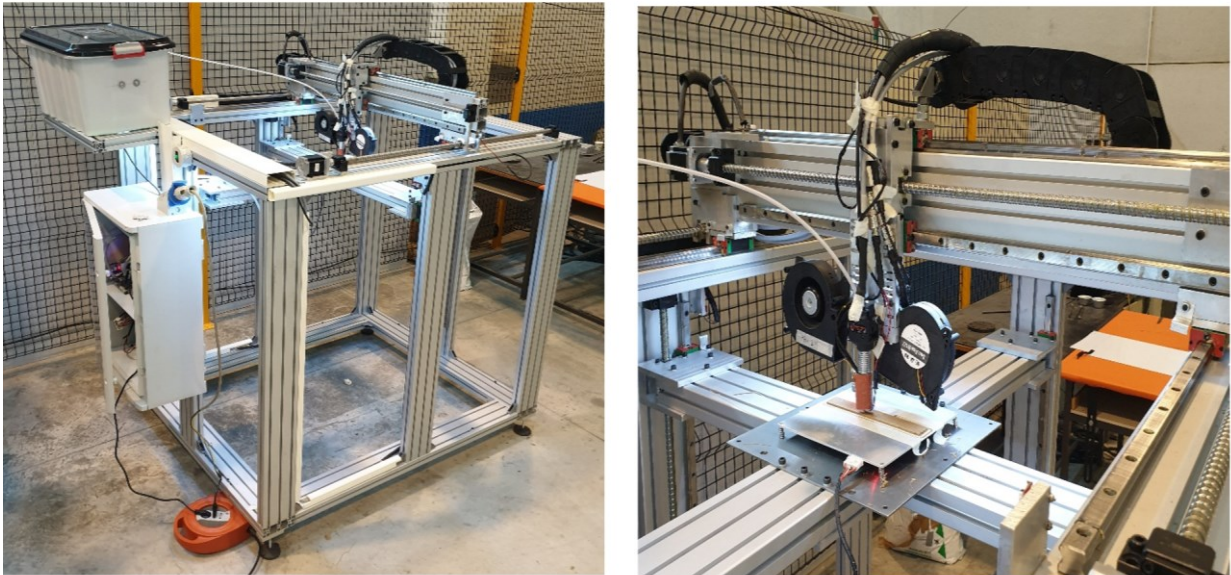


*Figure 15. 3D printer during printing*

To control all electronic components, an open-source 3D printing main board Duet 3 6HC has been used due to its open nature, connected to a Raspberry pi 4 to have a Wi-Fi connection. For our purposes, it is very important to not have any software constraints and the ability to configure it according to the instruments that are mounted on the 3D printer. As the main source, a Mean Well power supply 24V 1600W has been chosen. The wiring diagram of the printer is shown in Fig. 16. Printer-specific configuration files are listed in Appendix A.

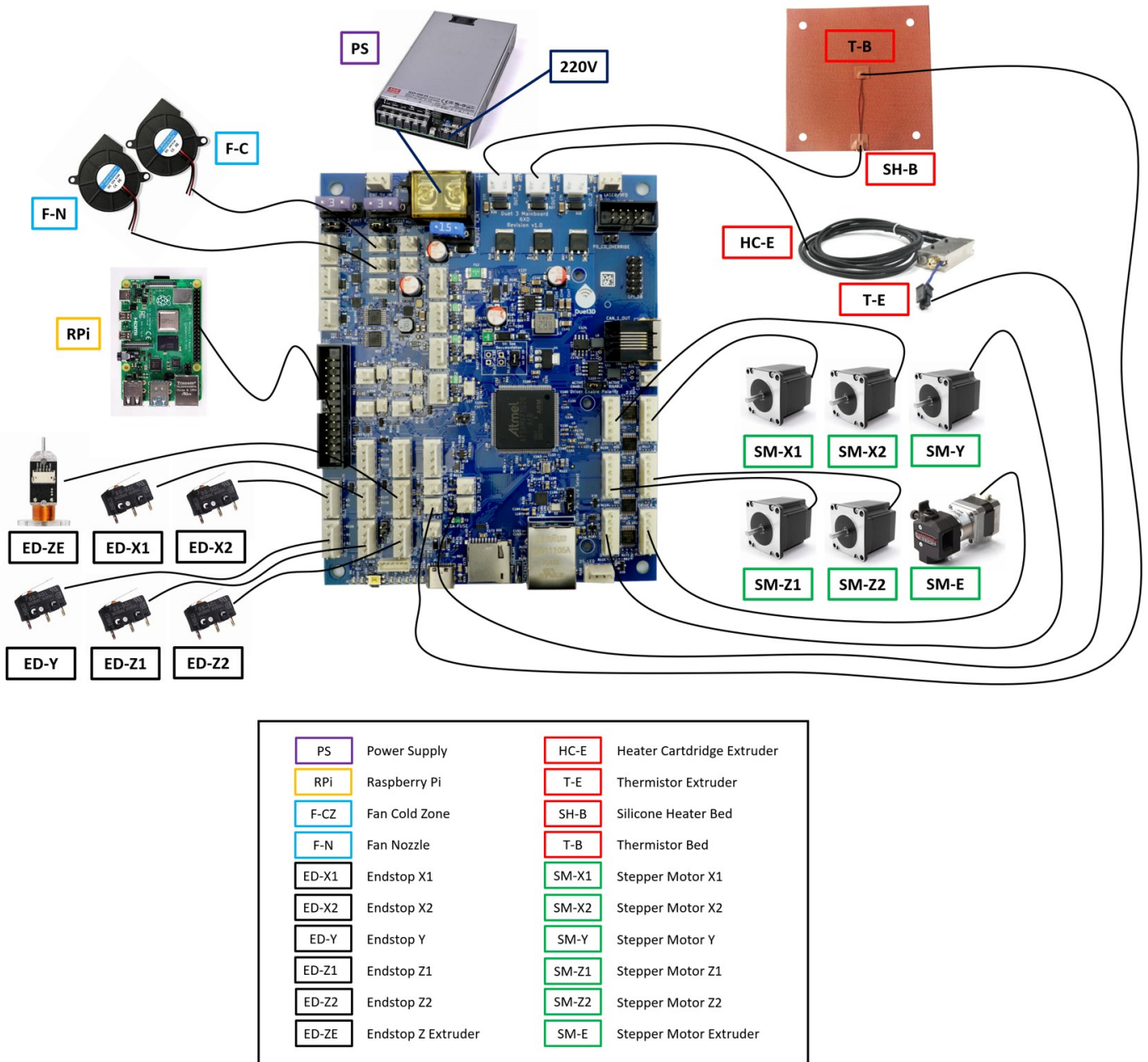


Figure 16. Wiring diagram of 3D printer

## 2.2 Results

The printer has been tested with different types of filaments, such as PLA, wood-filled PLA, and ABS, and has always managed to print them with good results. To achieve this, a calibration test must always be carried out to correctly calibrate the extruder flow. This test consists in printing only one outer wall of a cube and measuring it with a caliper, as seen in Fig. 17. In this case, a line width of 1.1mm has been set in the slicer while 1.13mm has been measured. The line width set in the slicer software should be equal to the measured one, otherwise, the flow parameter must be adjusted.



*Figure 17. Measurements of bead width and cube along directions x,y, and z*

Then to check the dimensional accuracy, a reference object is printed, a 40mm x 40mm x 40mm cube has been chosen and it is visible during and after printing in Fig. 18. In Fig. 17 the measurements in the three directions x, y, and z of the 3D-printed cube are pictured and a good level of accuracy can be achieved by calibrating the printer. The accuracy of the 3D-printed object is around 0.1mm. The 3D printer can print at different speeds, but a good compromise between time and quality is around 25mm/s, while the maximum speed is 100mm/s.

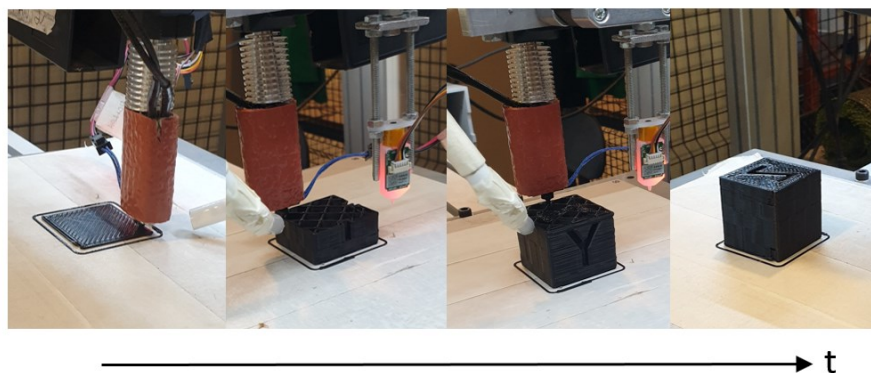


*Figure 18. Cube during and after printing*

### **2.3 Conclusions**

The result of the project is an FFF 3D printer with a build volume up to 700mm x 700mm x 900mm in X, Y, and Z, respectively, capable of printing with an accuracy of 0.1mm and a velocity of 25mm/s. With this printer, many specimens have been printed and tested. Thanks to open-source control software, the printer can be used as a test bench for any innovative tools, to verify its functionality. The printer is in the continuous development phase and the next step will be the assembly of a pellet extruder.

## CHAPTER III

### 3. THERMAL HISTORIES DEPENDENCIES IN A 3D-PRINTED PLA PART

Although additive manufacturing, and FFF in particular, has been developed to produce mainly prototypes of limited size, it is gaining more and more market shares for small scale production and even for parts of larger size [20]. In this case, it is beneficial to substitute the classical filament extruder with a single screw extruder that is fed with polymer pellets and equipped with a wider nozzle mounted as the extruder die [21]. This is convenient, since it allows higher flow rates and this in turn reduces the printing time of large parts. Moreover, pellets are cheaper than filaments and offer a greater versatility in terms of available materials. On the other hand, with larger nozzles it can be difficult to respect tolerances [22].

It has been found that the main parameters influencing the mechanical properties are the infill percentage, the raster angle [26], the build orientation, and the air gap [38, 39, 40, 41, 42]. All of these papers considered only the case of traditional filament fed extruders, characterized by small diameter nozzles (0.4 – 1.0 mm). In the case of small nozzles, the mechanical properties increase with the nozzle size, both in tension [40, 43, 44, 45, 46] and bending [46, 47] and this can be easily justified by the smaller number of deposited beads in a layer, which in turn decreases the number of intralayer bonds.

In the case of a larger nozzle, the heat capacity of the deposited beads is greater. This implies that under the same printing conditions the slower cooling rate will keep temperatures higher over a longer time. Moreover, due to the bead deposition procedure, a non-trivial thermal history is generated that consists of a succession of heating and cooling. Based on the particular location within the sample, the thermal history varies, due to different boundary conditions that are applied locally. For example, the middle of the sample is expected to remain hotter for a longer time if compared to the external surface that is in direct contact with air. A semicrystalline PLA has been used to print the samples because the crystalline structure of the polymer is highly dependent on thermal conditions [48, 49] and the extent to which crystallization occurs is a function of process characteristic temperatures and times [50, 51]. The consequent differences in crystallinity have a direct influence on the mechanical properties of the printed material [51]. Mechanical properties will be measured in bending rather than tension, because bending loads are often more dangerous for structural integrity of mechanical parts. The mechanical

properties have been correlated to the thermal history and the crystallinity of the sample measured at 3 locations of interest.

### 3.1 Experimental

#### 3.1.1 Materials

A semicrystalline PLA must be chosen because it can be evaluated based on the 3D print process parameters how these affects the crystallinity of the samples. Semicrystalline PLA pellet that has been used in this work is a poly(L-lactic acid) purchased from Natureplast (Arago, France) named PLE 005, which features a density of 1.25 g/cm<sup>3</sup>, a melt flow index of 7 g/10min (190 °C, 2.16 kg) and a melting temperature of 165°C. Before printing, the pellets have been dried at 55°C for 24 hours in a drier (FASTI KOCH ERD Xpert+, Koch Technik) and the material has been fed directly from the drier to the extruder through a compressor to avoid hydrolysis.

#### 3.1.2 Compression molding samples

After drying the pellets in an oven at 15 – 20°C below  $T_g$  for 24h, compression molded samples have been obtained using semicrystalline PLA. The specimens for the three-point bending test have been made [52] using Dolouets 383 thermo-molding press (France), heating pellets for 10 minutes at 200°C under atmospheric pressure in the mold and then applying a pressure of 150 bar for 5 minutes. Two types of specimens have been obtained according to ISO 178 standard with length, width, and thickness of 80mm, 10mm, and 4mm, respectively. Amorphous specimens have been obtained by quenching the material and submerging the mould in water. Instead, high degree of crystallinity specimens have been made by applying a slow cooling rate (i.e. less than 1°C/min), turning off the heaters of the compression molding machine, and holding in the mold before demolding to maintain dimensional tolerances. The difference between these two types of specimens in terms of aspect is visible in Fig. 19, in fact, the amorphous specimen on the right is transparent, while the other one is completely white.

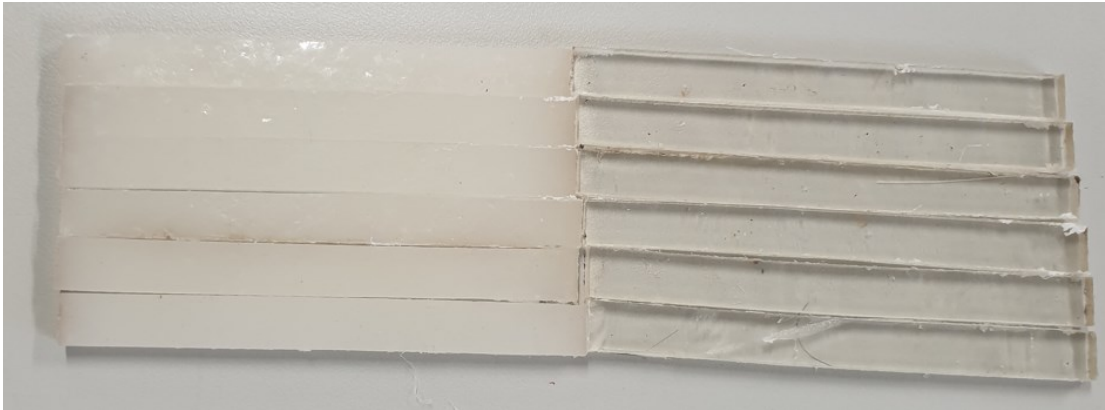


*Figure 19. High degree of crystallinity and amorphous compression molded specimens*

### **3.1.3 3D printing**

#### **3.1.3.1 3D printer**

The 3D printer is a self-assembled 3D printing platform called LASCALA. It consists of one pellet-fed single screw extruder mounted on a Stäubli TX200 robot arm, self-mounted on a 7 m length rail with a printing volume of 2m x 5m x 1m, in x, y, and z respectively. The printer is pictured in Fig. 20. The build plate is granite top and in order to enhance adhesion of the polymer beads, 3M Scotch-brand 2090 painter's tape has been used to cover the build plate. The tape was particularly useful since the plate was not heated. The extruder is fed with pellets through compressed air, taking them directly from a dryer. The extruder barrel has a diameter of 22mm, length over diameter ratio of 11 and it allows to mount nozzles of various diameters, i.e., 1mm,3mm,5mm,8mm, and 10mm. The maximum screw velocity is 250RPM and the maximum throughput is around 4kg/h.



*Figure 20. 3D pellet extruder robot arm during printing*

### 3.1.3.2 Custom extruder 3D printing path

To increase the productivity, reliability, and accuracy of the 3D printed part, a G-code that has been written directly using a MATLAB script (Appendix B) has been used instead of a standard slicing software. The input parameters that have to be specified are the bead width and height, the number of beads per layer and the number of layers. The extruder path is also an important input of the G-code file. This is pictured in Fig. 21: after complete deposition in the longitudinal direction of a single bead, the nozzle was led onto two brushes to clean it and remove the residuals coming from stringing. The deposition continued just beside the bead that was previously deposited in an analogous way until the layer was completed and so on for all the layers. Such a procedure ensured the same deposition time between two consecutive beads in the same layer, independent of the position. A sort of skirt, i.e. a line along the entire sample next to it, is printed to purge the nozzle and ensure a uniform output. Once a G-code has been obtained through this MATLAB script, containing all the movement of the extruder, it must be converted into a language that can be interpreted by the robot through the software, Acquarese. Here, printing speed, travel speed and temperatures of the different zones of the extruder are set and overwrite those contained within the G-code if present.



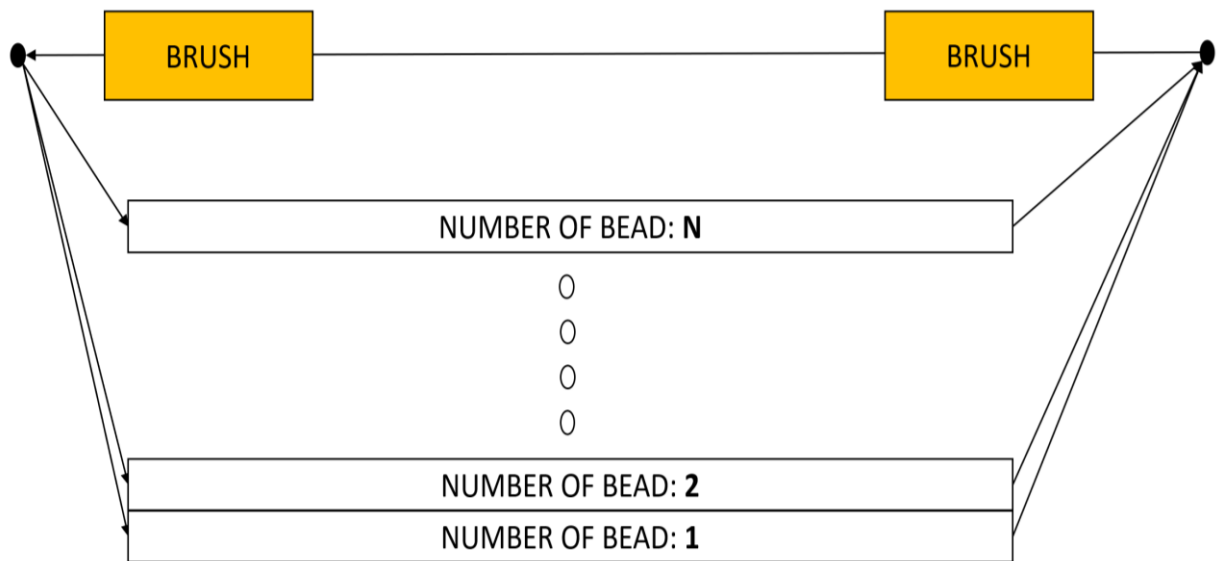


*Figure 21. Customized extruder printing path*

### 3.1.3.3 Calibration test

There may be differences, especially in the first layer, due to the large size of the printing plate. For this reason, the printing area is constrained only to a small part of the build plate to reduce this problem. Calibration is necessary and aims at achieving a bead dimension as similar as possible to the desired one. Using the same MATLAB program to generate the G-code described in the previous section, four layers of three equidistant beads in the area of interest of the build plate have been printed as a test. Next, these 3D printed specimens have been measured with a digital centesimal caliper to obtain the measured width and layer thickness of a single bead. Based on these measurements compared to the dimensions that should be obtained, the layer height to set in MATLAB software or the revolutions per minute (RPM) of the extruder screw could be changed:

- Layer height: decrease if measured bead width is less than reference or if the layer height is too high.
- RPM of the extruder screw: decrease if measured bead width is more than reference.

### 3.1.3.4 Printing parameters

Samples have been printed using a 3D pellet extruder equipped with nozzle diameters of 3, 5, and 8 mm. For each nozzle, the specimens have been printed with four different bead

widths, namely 100%, 125%, 175%, and 250% of the nozzle diameter. Regarding compression molded samples, the ISO 178 standard has been chosen, with sample dimensions of 80x10x4mm. Instead, for parts obtained using a pellet extruder, 3D printed PLA parts, the same standard ISO 178 have been used in a modified way. Samples size, in fact, has been scaled up by a factor of about 4, thus with a cross-section of approximately 40x16mm and a length of 320 mm. The specimen width has been chosen to be able to accommodate at least two beads per layer in the case of the largest bead width, which is 250% of the 8mm nozzle, i.e. 20mm.

The G-Code of the 3D-printed specimens is created using a MATLAB script (Subsection 3.1.3.2) that requires some input parameters, which are reported in Tab. 6. Some of the processing parameters are constant for all specimens, i.e. overlap, printing speed, and travel speed and these are equal to 0.3mm, 20mm/s, and 100mm/s, respectively. Such a procedure ensures the same deposition time between two consecutive beads in the same layer, independent of the position, which in this case is equal to 41s since travel and print speed has been selected as 100mm/s and 20mm/s, respectively. Further printing parameters are the processing temperatures and the three zones of the extruder and have been fixed at 220, 185, and 190°C, from the feeding zone to the die, respectively. Lastly, the screw speeds depend on the specimen type that is being printed and are reported in Tab. 6. The calibration test has been performed for each printing condition.

*Table 6. Geometric parameters for each sample type*

<b>Nozzle (mm)</b>	<b>Reference bead width (mm)</b>	<b>Number of beads per layer</b>	<b>Number of layers</b>	<b>Screw speed (RPM)</b>
3	3	15	15	6
	3.75	11	13	9
	5.25	8	12	15
	7.5	6	11	22
5	5	8	11	16
	6.25	7	11	19
	8.75	5	10	29
	12.5	3	7	61
8	8	5	8	33
	10	4	8	40
	14	3	6	73
	20	2	5	134

### 3.1.4 Quasi-static bending test

Bending tests have been performed on 3D printed samples and compression molded at room temperature at 2mm/min crosshead speed with a 10kN load cell using a universal testing machine (Instron 1185, INSTRON, USA). Before testing, the samples have been conditioned for 24h at 21.5°C and 50% relative humidity. The span of the 3D printed samples and compression molded ones have been fixed at 256mm and 64mm, respectively. A D5/400AG LVDT sensor (RDP Electronics) has been used to measure the displacement at the middle cross-section.

### 3.1.5 Thermocouple measurements in 3D printed object

Type K thermocouples (TC Direct) have been used to measure the thermal histories of the 3D printed specimens. These sensors have a diameter of 0.8mm and a tiny tip to minimize measurement errors. Temperatures have been acquired through a National Instrument data acquisition module (NI 9213) and recorded on a PC using the software LabView. Before each acquisition, the thermocouples have been calibrated using a Mettler FP 80 oven.

Thermal history has been measured from their deposition to ambient temperature in the central cross-section of each sample, i.e. at 160mm from both ends. Measurement has been performed at three different locations within the cross-section, pictured in Fig. 22 as T1, T2, and T3. The T1 and T2 thermocouples have been placed on the build plate to record the temperatures of the first layer, while the T3 thermocouple reads the temperature of the specimen center.

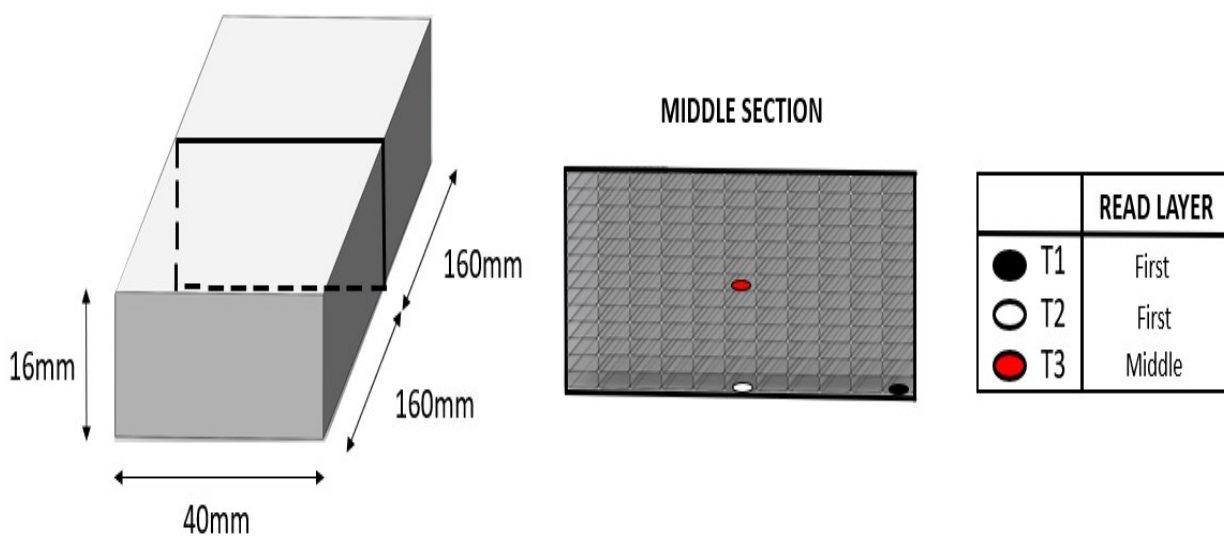


Figure 22. Thermocouples locations in the middle cross-section of the sample

### 3.1.6 Differential Scanning Calorimetry (DSC)

To study the thermal properties of PLA specimens, Differential Scanning Calorimetry (DSC) has been performed using a DSC (Mettler Toledo, Switzerland). Approximately 7 mg samples have been cut from the original specimens or pellets and sealed in an aluminum pan. Nitrogen has been fluxed to prevent polymer degradation. The crystallinity  $\chi_c$  of the specimens have been calculated as follows:

$$\chi_c = \frac{(\Delta H_m - \Delta H_{cc})}{\Delta H_m^0} \quad (3-1)$$

where  $\Delta H_m$  and  $\Delta H_{cc}$  are the enthalpies of melting and cold crystallization, respectively, while  $\Delta H_m^0$  the melting enthalpy of a theoretical 100% crystalline PLA. This value was taken equal to 97.3 J/g [53].

DSC has been performed on several samples using the different thermal protocols that are reported in Tab. 7 and in Fig. 23. Two different thermal protocols, named A and B, have been applied on pellets. Using thermal protocol A, the degree of crystallinity due to different cooling rates, ranging between 0.5 and 20°C/min (in particular,  $V_{cool} = 0.5, 1, 2.5, 5, 10$  and 20°C/min), has been measured during the second heating. A first heating has been performed to remove the previous thermal history, the sample has been then cooled down from 250 to -40°C at various cooling rates  $V_{cool}$ . Finally, the sample has been re-heated to 250°C at 10°C/min to determine the degree of crystallinity.

Thermal protocol B has been applied to determine the temperature range at which crystallization can occur. After the first heating, samples have been quenched at 100°C/min and maintained at an isothermal temperature  $T_{iso}$  for 1 hour. Such a time interval has been chosen based on the average time that is needed to 3D print the specimens that were described previously.  $T_{iso}$  has been chosen in the range 150°C down to 60°C in 10°C steps. After the isothermal step, the sample was quenched at 100°C/min from  $T_{iso}$  to -40°C and immediately re-heated from -40 to 250°C at 10°C/min to calculate its degree of crystallinity reached after the isothermal step.

Concerning compression molded and 3D printed samples, these have been just heated until 250°C at 10°C/min to determine their degree of crystallinity, and this thermal protocol is named C. The printed samples, built without the insertion of the thermocouples, were cut to extract small portions corresponding to the three virtual locations of the T1, T2 and T3 thermocouples. This allowed to correlate the evolution of bead temperature with the degree of crystallinity of the polymer at the 3 locations of interest in the printed part.

Table 7. DSC thermal cycles

MATERIAL	TYPE	NUMBER OF STEPS			
		1	2	3	4
Pellet	A	Heating from -40 to 250°C at 10°C/min	Cooling until -40°C cooling rate 0.5 - 20 °C/min	Heating to 250°C at 10°C/min	
Pellet	B	Heating from -40 to 250°C at 10°C/min	Cooling until Tiso at 100°C/min, Tiso= 60 - 150°C maintain for 1h	Cooling until - 40°C at 100°C/min	Heating to 250°C at 10°C/min
Compression molding and 3D printed	C	Heating from -40 to 250°C at 10°C/min			

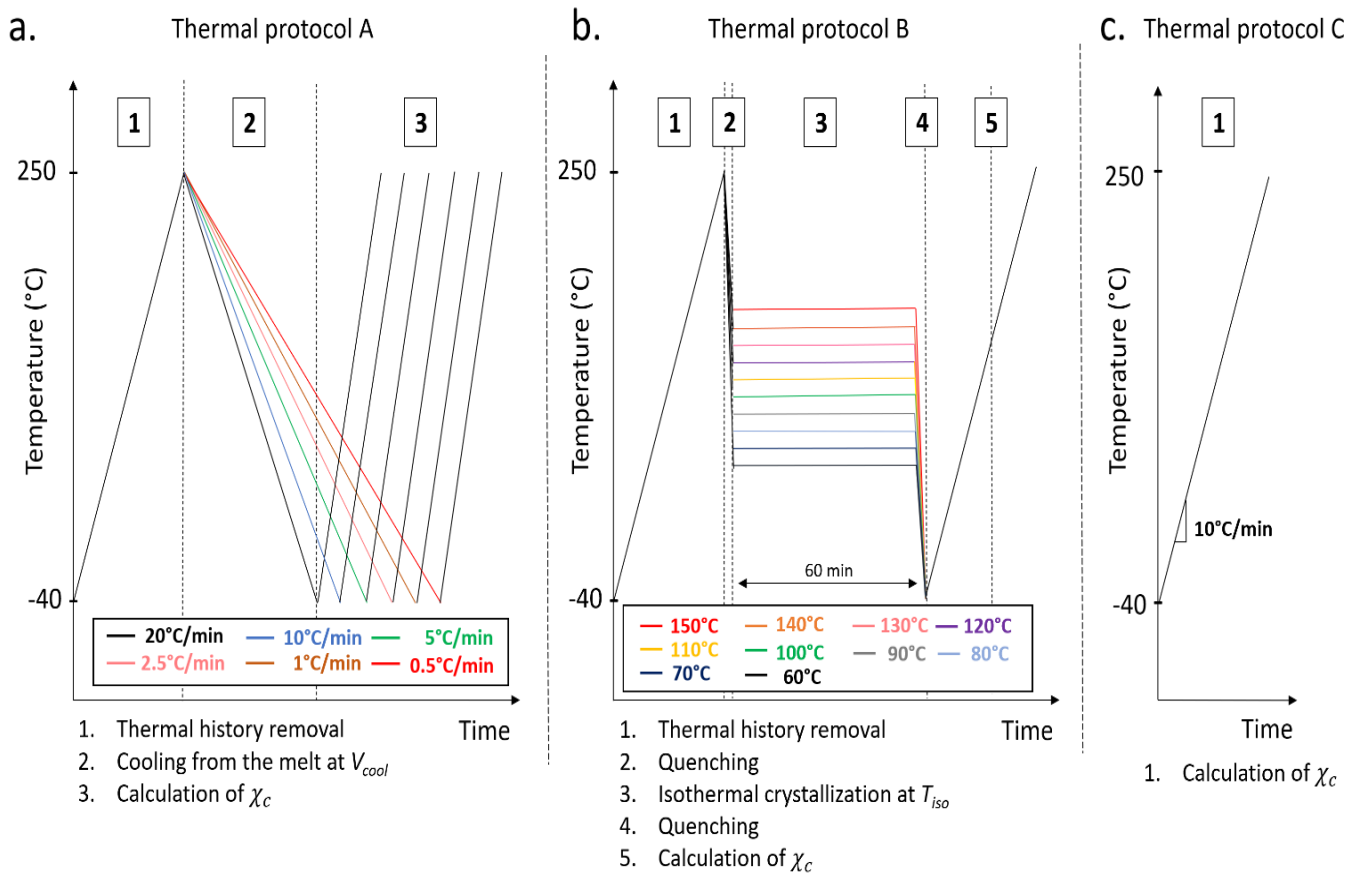


Figure 23. Schematic representation of the 2 thermal protocols applied on pellets a) with different cooling rates, b) with different isothermal temperatures and c) the thermal protocol applied on compression moulded and 3D printed sample

## 3.2 Results

### 3.2.1 Set and measured unitary bead

Despite the set bead width being supposed to be equal to the nozzle diameter ( $N$ ) multiplied by 1, 1.25, 1.75 and 2, the samples have been printed with a slightly different bead width, which has been measured after printing. For each bead, width corresponds to its height and both are listed in Tab. 8. An idealized bead transversal cross-section (Fig. 24) has been used to approximately describe bead surface (BS), can be obtained using the following equation:

$$BS = (w - h) h + \pi \left(\frac{h}{2}\right)^2 \quad (3-2)$$

where  $w$  and  $h$  are the bead width and height, respectively. After measurement, the  $BS$  value for each printing condition is then reported in Tab. 8. All the 3D printed specimens are identified with the code  $NX\_BSYY.Y$ , with the  $X$  digit representing the nozzle diameter in mm that was used, while  $YY.Y$  is the  $BS$  area in  $\text{mm}^2$ .

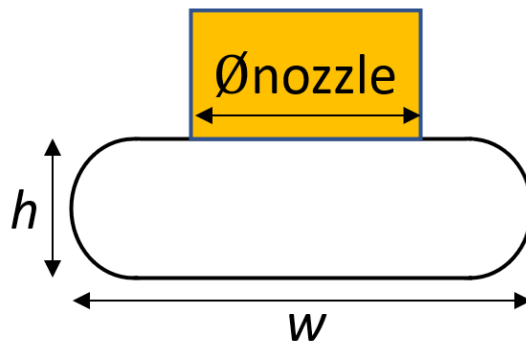


Figure 24. Idealized bead cross-section

Tab. 8 shows that thanks to a good calibration test, the measured bead widths are in good agreement with the set ones, as they differ at most by 0.5 mm.

*Table 8. Measured geometric parameters for each printed sample.*

Sample	Nozzle diameter (mm)	Reference bead width (mm)	Measured bead width (mm)	Measured Bead height (mm)	Measured Bead section (mm <sup>2</sup> )
N3_BS2.9	3	3	3.0 ± 0.04	1.05 ± 0.02	2.91
N3_BS4.4		3.75	3.8 ± 0.05	1.23 ± 0.02	4.35
N3_BS6.4		5.25	5.2 ± 0.06	1.31 ± 0.03	6.44
N3_BS10.4		7.5	7.5 ± 0.06	1.45 ± 0.03	10.42
N5_BS7.3	5	5	5.2 ± 0.05	1.50 ± 0.03	7.32
N5_BS9.1		6.25	6.4 ± 0.04	1.50 ± 0.04	9.12
N5_BS13.4		8.75	9.0 ± 0.06	1.55 ± 0.04	13.43
N5_BS29.1		12.5	12.4 ± 0.06	2.45 ± 0.06	29.09
N8_BS15.7	8	8	8.3 ± 0.05	2.00 ± 0.05	15.74
N8_BS20.1		10	10.5 ± 0.06	2.00 ± 0.05	20.14
N8_BS33.2		14	13.8 ± 0.07	2.50 ± 0.06	33.16
N8_BS60.2		20	19.5 ± 0.07	3.20 ± 0.07	60.20

### 3.2.2 DSC

Using the three different thermal protocols reported in Section 3.1.6, different results have been found and reported below in different sections.

During a print, the PLA beads undergo many heating-cooling steps at different heating and cooling rates leading to a different degree of crystallinity. Thus, thermal protocol A has been used to study the ability of the PLA to crystallize at different cooling rates  $V_{cool}$  from the melt (Subsection 3.2.2.1).

Moreover, it can be expected that the variation of the bead temperature reaches almost a plateau after the deposition of a few layers, thus the temperature could be assumed as constant. PLA could continue its crystallization at this temperature and to study this phenomenon at different isothermal temperatures  $T_{iso}$  has been applied thermal protocol B (Subsection 3.2.2.2).

The thermal protocol C has been used to estimate the degree of crystallinity of compression moulded and 3D printed samples, reported in Subsection 3.2.2.3 and Subsection 3.2.2.4, respectively.



**3.2.2.1 Degree of crystallinity of PLA pellets at a different cooling rate**

The glass transition temperature of the pellet has been evaluated at around 60°C, while the melting temperature is around 172°C, performing a common heating-cooling-heating thermal protocol at 10°C/min. In agreement with the technical data sheet of the material, the PLA that was investigated is a semicrystalline material, with crystallinity  $\chi_c$  that can be greater than 50%. In particular, using thermal protocol A, the maximum degree of crystallinity is 57% with the slowest cooling rate (i.e. 0.5°C/min), while a cooling rate equal to or higher than 5°C/min yields a basically amorphous material, as reported in Fig. 25.

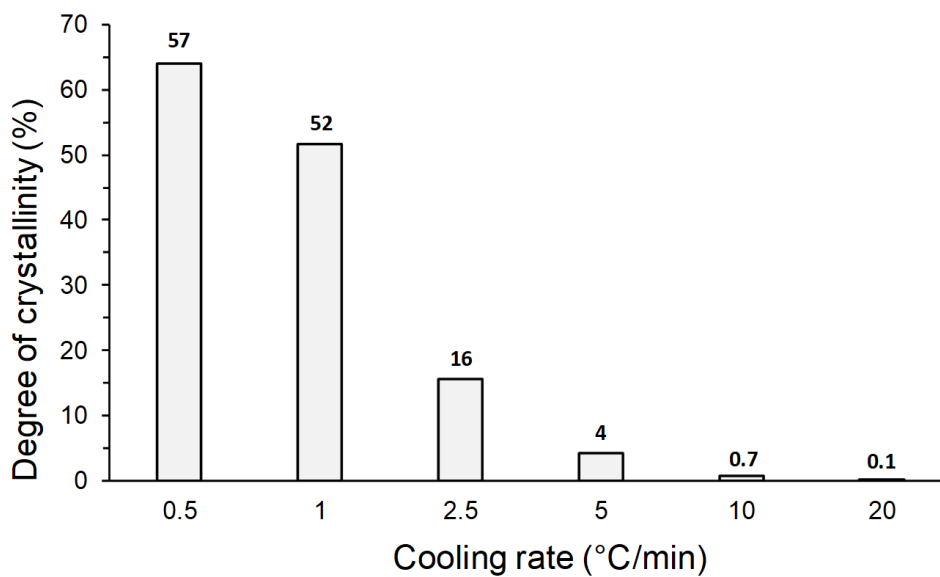


Figure 25. Degree of crystallinity on pellets depending on thermal protocol A

**3.2.2.2 Degree of crystallinity of PLA at different isothermal temperature  $T_{iso}$** 

Applying the isothermal DSC (thermal protocol B), it has been found that in one hour the temperature range at which crystallization occurs is in the interval of 90 - 140°C (Fig. 26). In all other condition thermal conditions, the PLA does not crystallize from the molten to the solid state. As expected, this range is between the glass transition and the melting temperature of the material. The maximum degree of crystallization is reached at the midpoint of such a range, i.e. around 120 – 130°C. The results are in good agreement with those obtained in Fig. 25 relative to the effects of the cooling rate in terms of the highest crystallinity obtainable (i.e.;  $\chi_c = 58\%$ ).

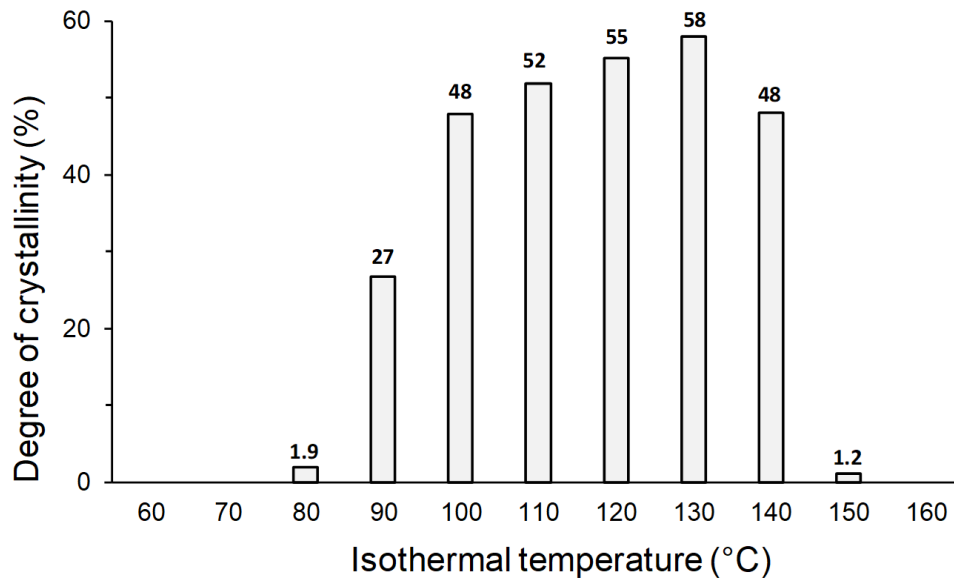


Figure 26. Degree of crystallinity on pellets depending on thermal protocol B

Summing everything up, the material is able to crystallize only if the cooling rate is lower than 10°C/min and if the constant temperature is between 90 and 140°C for a sufficient period of time. In all other thermal conditions PLA does not crystallize and remains amorphous.

### 3.2.2.3 Degree of crystallinity of the PLA in compression-moulding samples

Two compression molded samples have been produced and tested with simple heating from room temperature (thermal protocol C). Those that were quenched presented a 3% crystallinity, thus virtually completely amorphous as expected, while specimens that were slowly cooled after compression molding had  $\chi_c = 55\%$ .

### 3.2.2.4 Degree of crystallinity of the PLA in 3D printed samples

Concerning the 3D printed samples, three different DSC have been performed for each BS, taking a portion of the sample at the T1, T2, and T3 locations. DSC has been performed following thermal protocol C. The degrees of crystallinity  $\chi_c$  are reported in the histogram of Fig. 27 and displayed as a function of the various BS. The bead section seems to affect  $\chi_c$  independent of the nozzle diameter, in the sense that a higher crystallinity is obtained at greater BS. Nevertheless, the behavior is not monotonous, but it is quite clear from Fig. 27 that a BS threshold  $BS_T$  can be identified for each location, at which crystallinity increases sharply. Three different  $BS_T$  named  $BS_{T1}$ ,  $BS_{T2}$ , and  $BS_{T3}$  can be found in the histogram for the locations T1, T2, and T3, respectively.

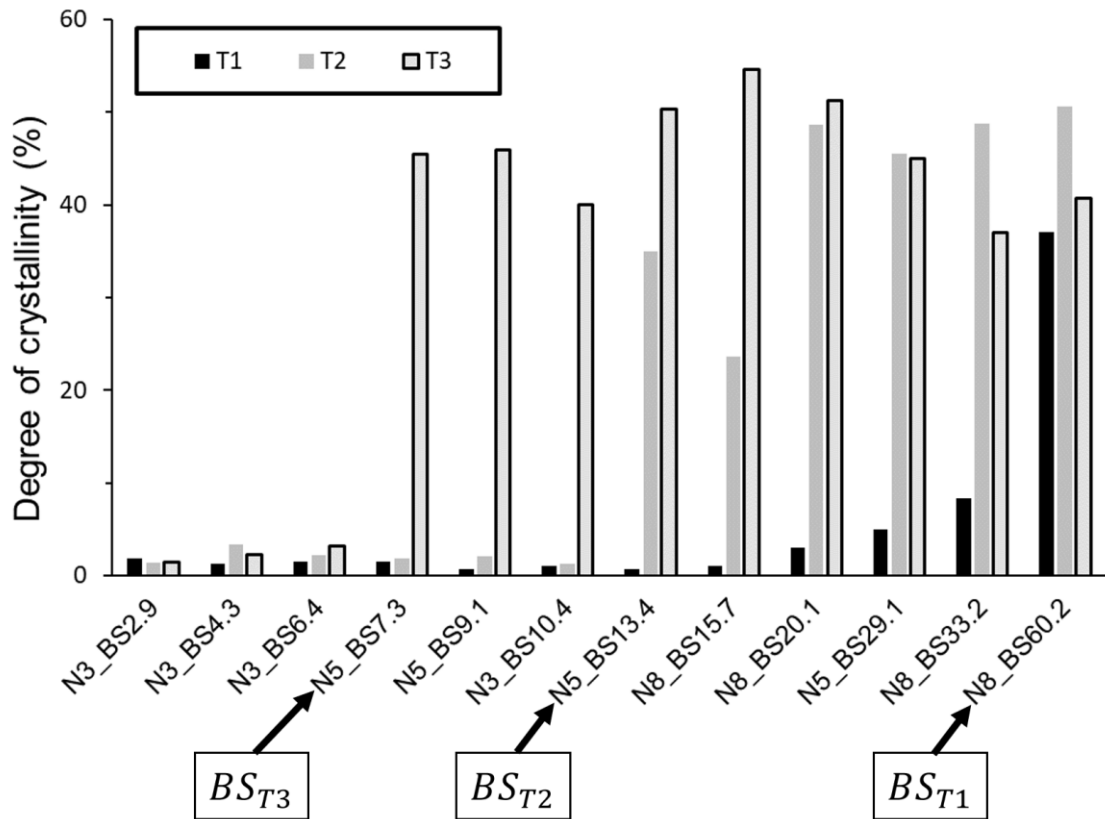
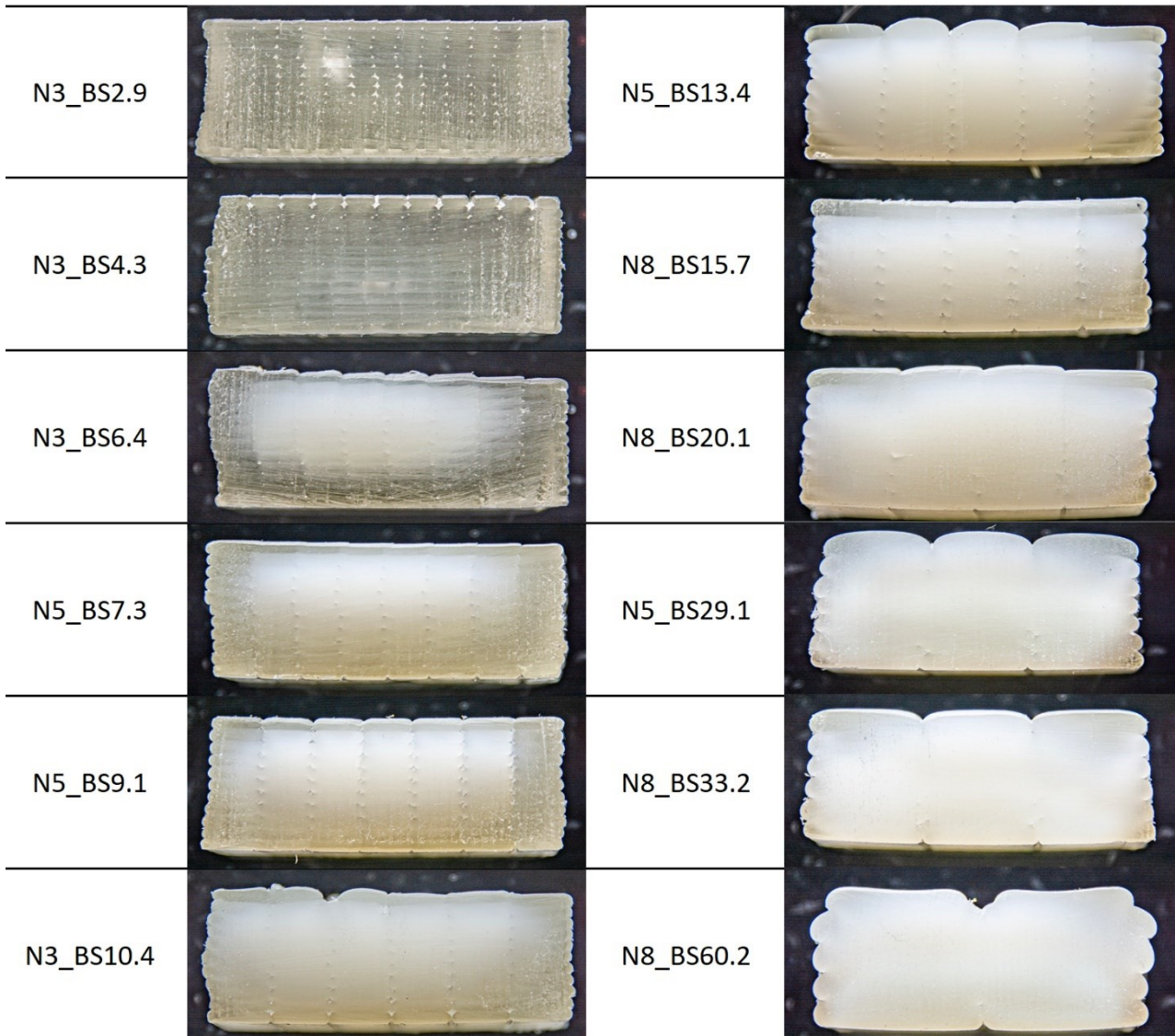


Figure 27. Crystallinity on 3D printed samples at T1, T2, T3 measured through thermal protocol C

Considering now the specific locations, T1 is in the half of the first bead, close to the edge, in contact with the build plate, that in the present case was not heated. For these reasons it has a faster cooling rate and hence an average temperature that is lower than the other two. This is the reason why the degree of crystallinity obtained in T1 is rather low and almost always less than T2 and T3 for all BS. Indeed, only in the largest BS (i.e. 60.2 mm<sup>2</sup>) the T1 crystallinity is high, due to the very slow cooling rate in the middle of the bead. In fact, moving from T1 to T3, thus from the exterior to the middle part of the samples, BS<sub>T1</sub> decreases until BS<sub>T3</sub> equal to 7.3 mm<sup>2</sup>, while BS<sub>T2</sub> is equal to 13.4 mm<sup>2</sup>. This behaviour is due to the beads that are laid around the particular location: the T3 location is completely surrounded by the other deposited beads, thus it is deposited over a warm surface and is kept for a longer time at a temperature where crystallization can occur. T1 and T2, on the other hand, are only heated up by the subsequently deposited beads and being located on the boundary, they cool down quickly. Interestingly, the crystallinity behavior at T1, T2 and T3 locations is independent of nozzle diameter and mainly depends on the BS. It can be

deduced that the main reason for this behavior is the thermal inertia of the deposited bead. A larger bead would simply cool down more slowly than a smaller one, determining a higher crystallinity. In order to improve clarity, a picture of the central cross section for each sample type is reported in Fig. 28 and listed in increasing order of BS.



*Figure 28. The cross sections of the various 3D printed samples for each BS*

The more crystalline material is clearly visible as a whitish portion of the section, while the amorphous material has a more transparent appearance and is mostly located at the cross-section boundary. All the DSC data agree with Fig. 28 in the sense that at greater BS the crystalline portion increase its size. In particular, with a BS that is less than 4.3 mm<sup>2</sup> the sample is in a mainly amorphous state, while starting from a BS of 6.4 mm<sup>2</sup> the crystalline zone starts to grow. The base and the edges are the last parts of the sample to crystallize, as

the plate is not heated and the lateral surfaces exchange heat with air at room temperature. With a BS equal to  $60.2 \text{ mm}^2$  the sample becomes almost completely crystalline. The crystallization phenomenon is much more evident with a larger BS, because the cooling time is longer. Notice also that the crystalline portion in the cross section is not symmetrical in the horizontal direction (Fig. 28): the right-hand side of the sample appears to be more amorphous than the left-hand side. In fact, the sample has been built in the direction from the right to the left, thus the portions that are located more on the right have a cooling time that is shorter compared to those on the left. In order to have a clear idea of these findings, a better understanding of the evolution of thermal history is fundamental.

### 3.2.3 Thermal history

The thermal history as a function of time for four sample types is reported in Fig. 29 for the three considered locations. For illustrating purposes, the sample types that have been chosen are the minimum BS made by the 3 mm nozzle (Fig. 29-a), the maximum one printed with the 8 mm nozzle (Fig. 29-d) and those corresponding to the central BS obtained through the 5 mm nozzle (Fig. 29-b and Fig. 29-c). It is important to remark that the thermal history is non-trivial and consists of a series of successive cycles of heating and cooling, due to the deposition of material during printing and nozzle thermal radiation, followed by a final cooling down once the production run is finished.

In each location for all BS, the first peak has the highest temperature as it directly reads the temperature of the material that has just been laid. The subsequent peaks are divided into two types, according to the time interval in which they are repeated. The first type of peaks is characterized by a smaller amplitude and is due to the deposition of beads next to the considered one every 41s equal to  $2.4 \cdot 10^{-2} \text{ Hz}$ , within the same layer. The second type consists in a higher heating and is due to the deposition of beads above the considered location. The time interval between these peaks decreases as the BS becomes larger, because the print time of a single layer is less. The peaks are increasingly attenuated because at each successive peak the distance between the thermocouple and the subsequently deposited beads increases. This is particularly visible in the thermal history T1 of Fig. 29-a and Fig. 29-b, due to the smaller thermal inertia of small beads and to the faster cooling of this location with respect to the other ones, as it is closer to the exterior boundary.

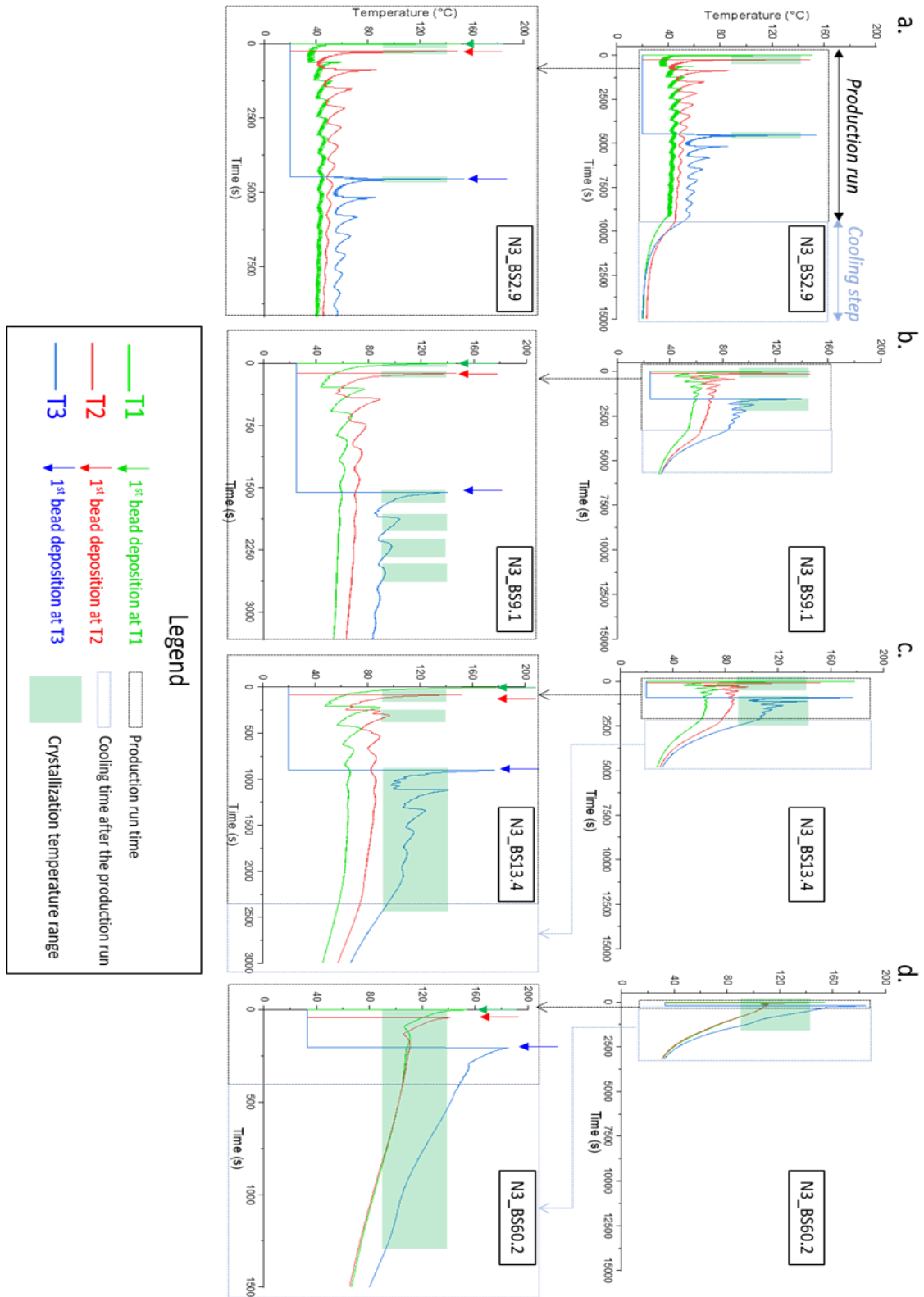


Figure 29. Thermal histories T1, T2, T3 during printing until cooling down for (a) N3\_BS2.9; (b) N5\_BS9.1; (c) N5\_BS13.4; (d) N8\_BS60.2.

The thermal histories are in good agreement with the crystallinity results (Fig. 27). It is evident that the measured temperature at T1, for each BS, is lower than that at location T2, which in turn is lower than T3. In fact, a high degree of crystallinity occurs earlier in T3 rather than in T2 and T1, in other words  $BS_{T3}$  is smaller than  $BS_{T2}$  and  $BS_{T1}$ .

In Fig. 29 the temperature range at which crystallization occurs is highlighted in green. The degree of crystallinity is influenced both by the temperature and by the time of permanence within this region. As BS increases, the thermal history curves fall within such a region for a non-neglectable period of time, sufficient for inducing crystallization. In fact, for the smallest BS all curves are located below this region and the resulting material is completely amorphous. In Figs. Fig. 29-b and Fig. 29-c only some locations remain within crystallization region for a sufficient time and for the biggest BS all curves are within this region, considering both printing and cooling time, and indeed the material is completely crystalline, as also shown in Fig. 28.

As a final remark, to understand the results properly it must be clear that not only temperature is important but also time, and the time dependence is a bit more difficult. Thermal inertia increases with BS, thus at larger BS the average temperature in the sample is higher and also the cooling of the single bead requires more time. The result in terms of crystallinity is heavily dependent on final cooling after the end of the 3D printing phase (Fig. 29-d). On the other hand, at lower BS the number of beads is higher, thus the total printing time increases. This induces more heating cycles which keep the average temperature within crystallization range, especially in the center of the sample, i.e. at T3 (Fig. 29-b and Fig. 29-c). As a result, crystallization is not easy to predict.

### 3.2.4 Bending tests

In Fig. 30 typical stress versus strain curves are reported. Two different mechanical behaviors can be recognized. In one case the material is stiffer and more brittle with strain at break below 2% and characterized by a completely linear elastic behavior; in the other case the material is less stiff and has a strain at break greater than 2%, displaying also some yielding behavior with a slight deviation from linearity. Quenched compression molded samples together with small BS belong to this last group, while the slowly cooled compression molded ones and the larger BS are part of the former one. Notice that samples printed through the 5 mm nozzle may belong to both groups depending on their BS. Interestingly, the stiffer material is not stronger, and this is probably due to the higher toughness of the less stiff material.

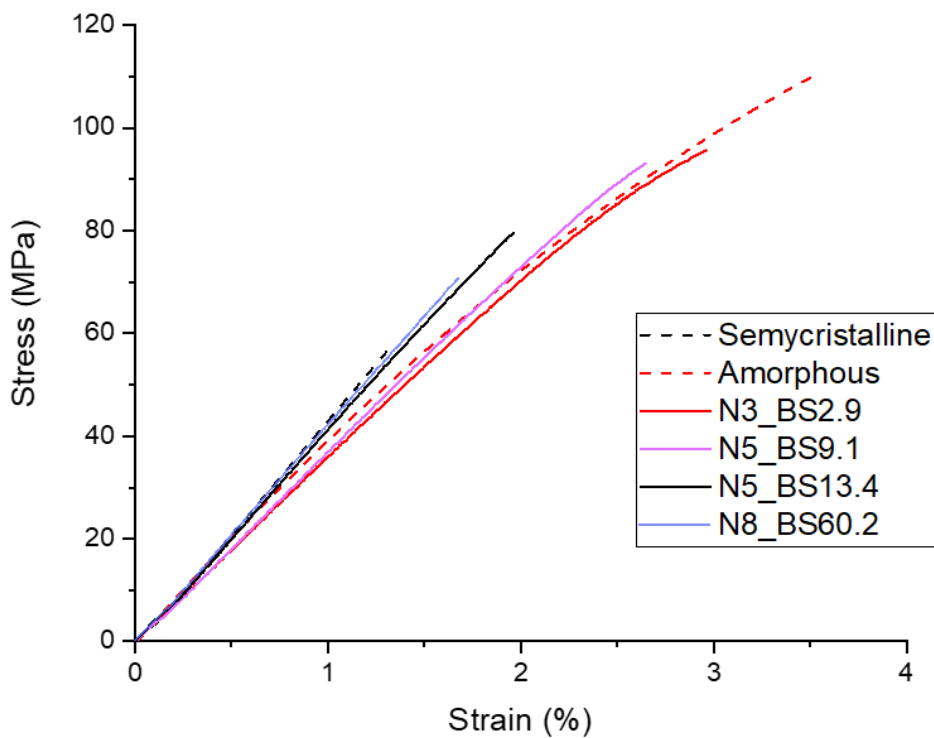


Figure 30. Stress vs strain curves for compression molded samples and a selection of 3D printed specimens



The complete results in terms of Young's modulus, ultimate stress and strain at break for all 3D printed and compression molded samples are pictured in the histograms of Fig. 31.

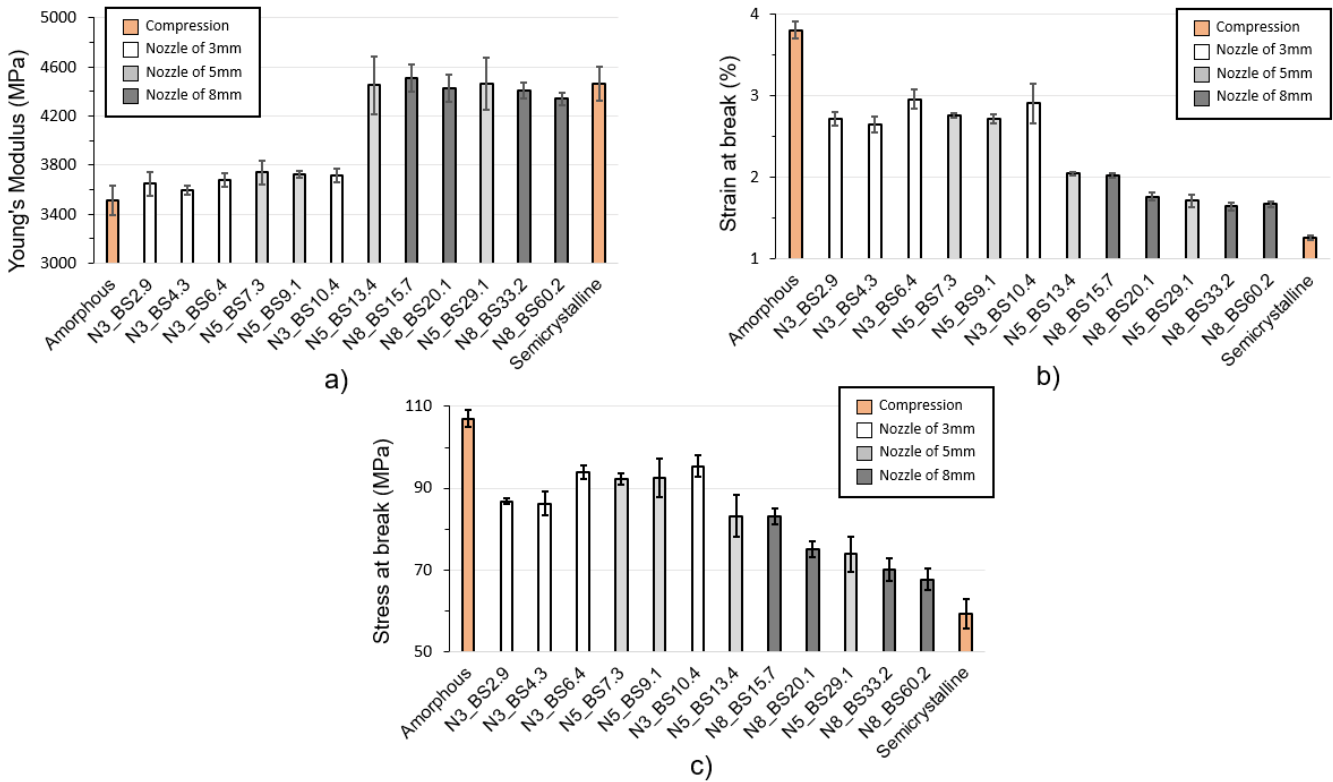


Figure 31. Mechanical properties for compression molded and 3D printed samples at different BS. a) Young's modulus, b) Stress at break and c) strain at break

In general, the standard deviation of all measurements is quite small, thus denoting a good repeatability within the sample types. Concerning the compression molded samples, their Young's moduli are about 3500 for the amorphous material and about 4500 for the semicrystalline one, i.e. a difference of 1 GPa, or about 25%. This is in line with crystallinity results of the same materials. On the other hand, the strain at break of the amorphous material is about three times as much the strain at break of the semicrystalline one (3.8% vs. 1.3%) and the strength value is about twice (107 MPa vs. 59 MPa). This behavior has been observed also by Perego [54], with PLA of low molecular weight.

Concerning the 3D printed samples, all mechanical properties are completely included within the interval that is identified by the compression molded specimens. It can be seen that the most important parameter that describes the behavior is anyway the BS, in fact the mechanical properties display a certain trend as a function of the BS, and this occurs independently of the specific nozzle that has been used, similarly as what was observed for crystallinity.

The Young's modulus behavior (Fig. 31-a) resembles that of crystallinity (Fig. 27) in that a BS threshold can be defined between 10.4 and 13.4 mm<sup>2</sup>. Below such a threshold the material is more compliant and behaves similarly to the amorphous compression molded samples, while above the threshold the material is stiffer and shows modulus values that are close to that of the slowly cooled compression molded specimens. Within each group there are only little differences among the various sample types, on the other hand across the threshold the difference is definitely larger and is similar to that observed for the compression molded samples. From Fig. 28, it is clear that the threshold is attained when the crystalline region reaches the location T2 in the cross section of the 3D printed specimen. This can be explained easily, since when loaded in bending, stress is higher in the peripheral region of the cross section (i.e. farthest from the neutral plane).

The same behavior is reflected also in the strain at break histogram of Fig. 31-b, where one can recognize the same threshold, this time identifying a transition from a relatively large ultimate strain (i.e. in excess of 2%) to a smaller one. Crystalline compression molded samples have indeed a very low strain at break, that is slightly above 1%, making this material particularly brittle.

The behavior in terms of ultimate stress (Fig. 31-c) is more difficult to understand. Again, the behavior seems to respect the threshold BS that was identified previously, but the difference between the two groups is less sharp than in the other two histograms. Predominantly amorphous 3D printed materials possess strength values that are quite high and uniform, being in the 85 – 95 MPa range, but none of them comes close to the almost 110 MPa strength displayed by the amorphous compression molded samples. The semicrystalline samples, on the other hand, display lower strength values and have a decreasing trend with the BS, going from 83 MPa down to 68 MPa, thus almost reaching the strength of the slowly cooled compression molded material at 59 MPa. In any case, the bending test results are in good agreement with the crystallinity results that were described in the previous section.

---

### 3.3 Conclusions

Thermal properties of FFF 3D printed semi-crystalline PLA parts have been studied concerning their relationship with geometric processing parameters such as the bead surface (BS). The samples have been printed using a large-scale 3D printer, using different nozzle diameters ranging from 3 mm up to 8 mm, fed with polymer pellets. Using a regular 3D printer filament equipped with a small nozzle, only a little BS can be printed, and only an amorphous sample can be achieved. It has been found that the bead surface affects the degree of crystallinity, influencing the average temperature and permanence time at the temperature range at which crystallization can occur.

Keeping all the printing parameters constants, except the bead width and height, samples with different internal distributions of the degree of crystallinity in the transversal cross-section have been obtained. Such differences in crystallinity distribution have a direct consequence on the mechanical properties. In particular, the more crystalline material appears to be stiffer but also more brittle and less strong.

To better understand these distributions within the sample, thermal histories have been measured at three different locations and they are composed of an alternation of heating and cooling during printing. These thermal histories depend not only on the bead volume but also on the various parameters that influence the heat transfer between the deposited polymer and the surrounding environment. This in turn gives rise to crystallinity inhomogeneities within the sample cross section, and consequently affects the resulting mechanical properties.

## CHAPTER IV

### 4. MATHEMATICAL MODELLING THROUGH CLT OF 3D PRINTED PLA FILLED WOOD SAMPLES

The self-built 3D printer described in Chapter II has been used for this activity. The samples, according to ASTM D3039 and ASTM D3518, have been printed with PLA filled with wood flour. The mechanical properties are maximum along the printing direction and minimum in all directions that are normal to the printing direction, thus the material is transversely isotropic [24]. FFF 3D printed parts can be thought of as laminate and modelled using CLT (Section 1.4), considering a raster filled layer as a unidirectional lamina. Here both stiffness and strength are studied. Most papers dealing with CLT-based modelling are concerned about stiffness [55], while limited work has been done on strength [56]. To study the strength, the Tsai-Hill criterion coupled with ULF is chosen, as it considers the failure sequence of all laminae.

#### 4.1 Experimental

##### 4.1.1 Filament material

The mechanical properties of a 3D print part are anisotropic and to emphasize it even more, a material filled with short fibers have been chosen as reference. To keep the material fully compostable, natural wood fibers have been used. A commercial 1.75 mm diameter (0.05% tolerance) FFF filament has been purchased from ColorFabb (Belfeld, The Netherlands). The material is named “woodFill” and according to the manufacturer is a blend of poly-lactic acid (PLA) and poly-(hydroxyalkanoate) filled with 15Wt.% fine pinewood fibers. Before printing, the filament has been dried at 80°C for 24 h, and during the printing process, the reel has been stored in silica gel. This material belongs to the class of green composites, which are of great interest in the current scientific literature due to their low environmental impact [57, 58].

##### 4.1.2 3D Printing

###### 4.1.2.1 3D Printer

The 3D printer that has been used is the self-built prototype described in Chapter II. The hotend has been equipped with a 0.8 mm steel nozzle and printing has been performed over a 22 cm x 22 cm heating bed. Masking tape has been used on the heated plate to improve the first layer adhesion and to limit the warping effect.

**4.1.2.1.1 Calibration test**

To calibrate the flow of the extruder, the flow parameter in the slicer (CURA) must be adjusted. To perform this calibration, a cube of 20mm x 20mm x 20mm is printed with 1 wall thickness, 0% infill, and two bottom layers. In this way, the wall thickness, which should be equal to the line width, is measured with a centesimal caliper. If the wall thickness is equal to the line width value set in the slicer, the flow is correct. In the other case through a proportion, the correct value of flow is found, set in the slicer and the cube is reprinted. The procedure must be repeated until the measured wall thickness is equal to the line width set in the slicer.

**4.1.2.2 3D printing parameters**

As specific tensile testing standards are not available for 3D printed materials [59], ASTM D3039 rectangular specimens have been chosen for longitudinal and transverse properties due to a lesser incidence of stress concentrations than dog-bone ones [24, 60]. Instead, ASTM D3518 specimens have been used for shear characterization. All specimens are 200mm long and 25mm wide, while the thickness would depend on the particular lay-up that is considered. The G-Code has been obtained using open-source software Ultimaker Cura 4.8.0 and processing and structural parameters are listed in Tab. 9 and Tab. 10, respectively. A total of five lay-up types with 100% raster infill have been printed, and their number of layers and lamination sequence are reported in Tab. 10. The first two laminates in Tab. 10 are unidirectional, while the last two are symmetrical and balanced. Moreover, the first three laminates are used for characterization, and the last two lay-ups are both quasi-isotropic and are used for validation purposes.

*Table 9. The processing parameters to print various samples.*

<b>Parameters</b>	<b>Values</b>	<b>Parameters</b>	<b>Values</b>
Layer height (mm)	0.45	Bed temperature (°C)	60
Line width (mm)	1	Raster infill (%)	100
Nozzle diameter (mm)	0.8	Printing speed (mm/s)	10
Nozzle temperature (°C)	200	Contour lines	1

*Table 10. List of tested laminates and their characteristics, the standard deviation is indicated in parenthesis*

<b>Laminates</b>	<b>Number of layers</b>	<b>Thickness (mm)</b>	<b>Width (mm)</b>
[0]8	4	1.53 (0.02)	25 (0.07)
[90]8	4	1.54 (0.01)	25.13 (0.06)
[+45/-45] <sub>2s</sub>	8	3.54 (0.01)	25.1 (0.01)
[0/+45/-45/90] <sub>s</sub>	8	3.53 (0.02)	25.3 (0.1)
[+30/-30/90] <sub>s</sub>	6	2.55 (0.03)	25.3 (0.01)

#### 4.1.3 Digital Image Correlation (DIC)

It is an optical technique to measure without contact the displacements, therefore the deformations in three-dimensions of specimens made by almost any material. The hardware that has been used is a DANTEC 3D Q-400 (DANTEC DYNAMICS, Denmark) with ISTR 4D software, pictured in Fig. 32. The system comprises two digital cameras with 12 Mpx resolution.

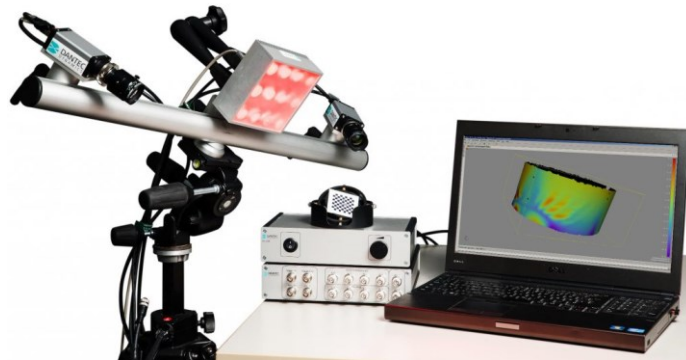


*Figure 32. Hardware DANTEC 3D Q-400*

The acquisition consists of a series of photos of a surface before and after several stages of deformation with a certain interval between each photo, depending on the test. Once the images are captured, through ISTR 4D software, the deformation can be obtained by comparing the different images through the points on the surface. The preparation of the samples is required, painting them randomly and punctually, obtaining samples such as those shown in Fig. 33.



*Figure 33. Samples painted for DIC acquisition*

#### **4.1.4 Quasi-static tensile test**

Tensile tests have been performed on filament and 3D printed samples. The specimens have been printed following ASTM D3039 and the printing parameter reported in Tab. 9 and Tab. 10. Rubber tabs, 30mm long and 25 mm wide have also been used in agreement with the standards. Before testing, the samples have been dried at 60°C for 24h. Tensile tests on filament and lay-ups have been performed at room temperature at 1 mm/min crosshead speed using a universal testing machine (INSTRON 4467, INSTRON, USA) pictured in Fig. 34. Filament specimens of 150mm length have been attached to the dynamometer using drill chucks with a 120mm gage length and tested with a 500N load cell, while the lay-ups have been tested using a 30kN load cell. Testing has been done on at least five specimens and DIC has been used to measure both longitudinal and transverse strain. The smooth part of the specimens (the one that was in contact with the hot bed) has been stained with white ink, to insure a better reading from the DIC cameras.



*Figure 34. Testing machine INSTRON 4467*

#### 4.1.5 Testing equipment

The instruments that have been used are listed below:

- Balances: To weigh the specimens two types of balances have been used, reported in Fig. 35. To measure the filament, the most precise Mettler model AE 240 has been used, which has a full scale of 205 g and a resolution of 0.01 mg. While the Adventure PRO AV4102C has been used to measure the samples, with a full scale of 4100g and a resolution of 0.01 g.



*Figure 35. Balance Mettler model AE 420 and Adventure PRO AV4102C*



- **Micrometre:** To measure the thickness and width of the samples a micrometer has been used, due to a higher accuracy than a caliper. The micrometer is a Mitutoyo 293, reported in Fig. 36, with a measuring range between 0 and 25 mm and a resolution of 0.001 mm. It is a digital instrument and has an error limit at 20°C of  $\pm 2\mu\text{m}$ .



*Figure 36. Micrometre Mitutoyo 293*

- **Caliper:** To measure the length of the samples a digital caliper has been used with a resolution of 0.01 mm.

#### 4.1.6 Density measurements

The FFF 3D printing process generates parts with internal porosity even if the slicer settings are set to create the object with a 100% infill. Lower porosity values can be achieved by calibrating the machine by varying some printing parameters, such as extrusion flow, extrusion temperature, and print speed, but in general, there is always a certain percentage of voids. To calculate the percentage of voids of the specimens printed at 100 % infill the following formula has been applied:

$$\rho = \frac{M}{V} \quad (4-1)$$

where M is the mass of the sample and V is its volume. Knowing the density of the 3D printed samples and the density of the bulk material, through Eq. (4-2) the percentage of voids can be calculated.

$$\%_{voids} = \left(1 - \frac{\rho_{sample}}{\rho_{bulk}}\right) \times 100 \quad (4-2)$$

Density of 3D- FFF printed products has an important influence on their mechanical properties.

**4.2 Results of tensile test and CLT validation**

To better understand the mechanical properties of filament and the various lay-ups, they are plotted all together in a stress-strain diagram in Fig. 37. Mean and standard deviation of Young's modulus, stress at break, Poisson's ratio, and density are reported in Tab. 11. Concerning Young's modulus and strength, the table reports both the experimental results and values that have been corrected applying the contour correction (Chapter 1.4.4), with  $\phi_{con} = \frac{2}{25} = 0.08$  and  $\phi_{lam} = 1 - \phi_{con} = 0.92$ , according to Tab. 9 and Tab. 10. All the measurements present a very small standard deviation, indicating a good repeatability in the tests. Poisson's ratio of  $[90]_4$  laminate is calculated through Eq. (1-3).

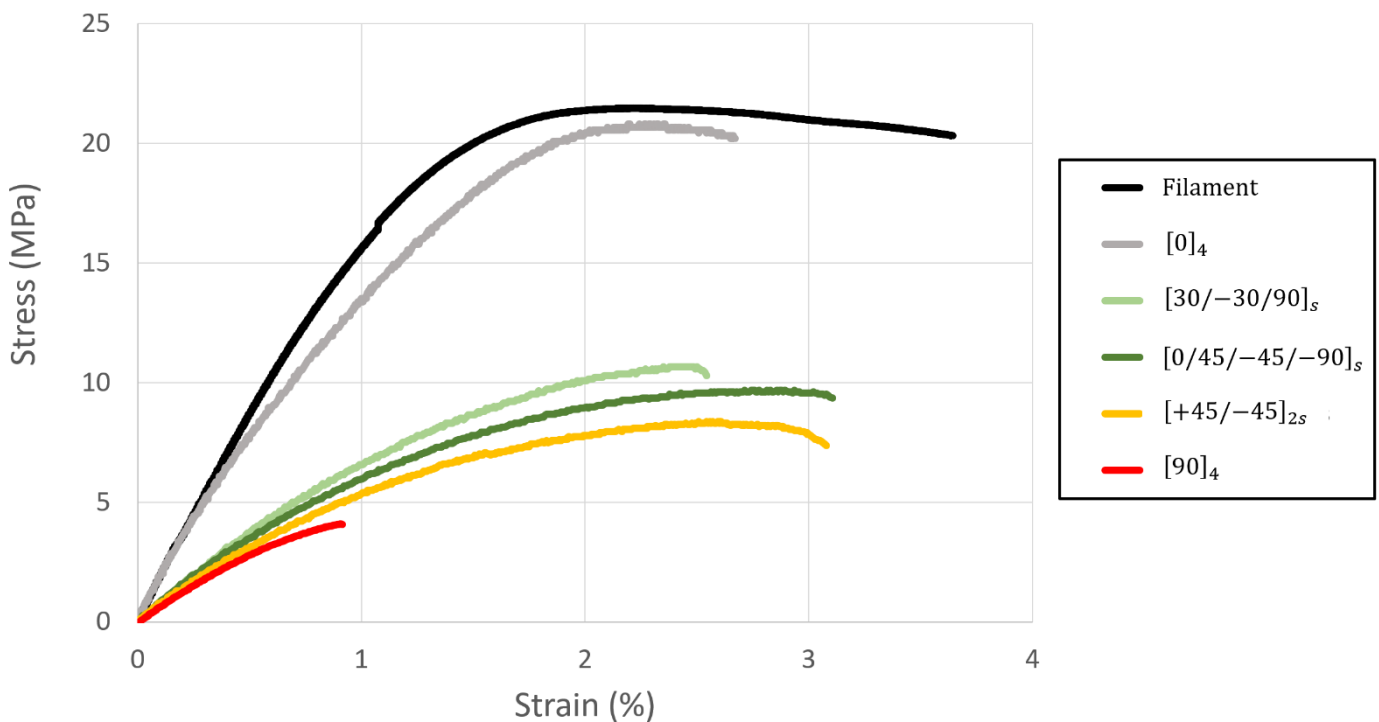


Figure 37. Representative tensile test of the wood flour filled filament and 3D-printed lay-ups

*Table 11. Experimental results of the tensile tests on the filament and lay-ups and the contour line corrected values that are used for laminates characterization. The numbers in parenthesis represent standard deviation*

Sample type	Density (g/cm <sup>3</sup> )	Young's modulus (MPa)		Strength (MPa)		Poisson's ratio (mm/mm)
		Lay-up	Laminate	Lay-up	Laminate	
<b>Filament</b>	1.04 (0.01)	2079 (14.8)	--	23.6 (1.05)	--	--
<b>0°</b>	0.87 (0.015)	2065 (90.4)	--	20.6 (0.15)	--	0.35 (0.015)
<b>90°</b>	0.83 (0.017)	730.5 (66)	614.5	3.62 (0.42)	3.04	--
<b>[+45/-45]<sub>2s</sub></b>	0.79 (0.01)	1081 (95.2)	995.4	8.29 (0.09)	7.63	0.37 (0.03)
<b>[0/45/-45/90]<sub>s</sub></b>	0.78 (0.005)	1282 (107)	1241	9.29 (0.45)	8.8	0.31 (0.02)
<b>[30/-30/90]<sub>s</sub></b>	0.79 (0.006)	1351 (45.3)	1289	9.98 (0.81)	9.52	0.29 (0.02)

The tests on the filament test indicate that, the material is elastoplastic, with yield occurring at 2% strain. The ultimate stress and strain are around 23MPa and 4%, respectively. The 3D-printed laminates based on the sequence of lamination can achieve different mechanical properties, and the two extremes are [0]<sub>4</sub> and [90]<sub>4</sub>. The [0]<sub>4</sub> unidirectional lay-up is very similar to the filament, with almost equal strength and a smaller value of ultimate strain. It has the highest mechanical properties compared to all the other lay-ups, while the [90]<sub>4</sub> has much smaller properties. All the other lay-ups are very similar especially at low strains, in fact, they present almost the same Young's modulus. As expected, the density of a 3D-printed part decreases by about 20%, due to the presence of voids, despite 100% infill. Usually, higher density means higher mechanical properties, but not in this case because this PLA filled with wood, is highly anisotropic. In fact, although [90]<sub>4</sub> has a higher density than all other laminates, except [0]<sub>4</sub> laminate, it exhibits much lower mechanical properties.

At this point, the unidirectional lamina can be characterized completely by 7 parameters reported in Tab. 12.

*Table 12. The seven independent parameters that characterize the unidirectional lamina*

<b>Property</b>	<b>Value</b>
$E_1$ (MPa)	2065
$E_2$ (MPa)	314.5
$\nu_{12}$	0.35
$G_{12}$ (MPa)	363.3
$\sigma_L$ (MPa)	20.6
$\sigma_T$ (MPa)	3.04
$\sigma_{ST}$ (MPa)	5.37

These values have been corrected through contour correction. Five parameters can easily be found through bending test of the unidirectional  $0^\circ$  and  $90^\circ$  laminates, while  $G_{12}$  and  $\sigma_{ST}$  can be estimated through Eq. (1-14) and the procedure in Section 1.4.3, respectively. These parameters will be used for the quantitative prediction of stiffness and strength through the formula and algorithm described in Section 1.4.4. The Young's modulus  $E_{lam}$  in a tensile test of a symmetric laminate composed of N laminae of thickness t is given by the following equation:

$$E_{lam} = \frac{1}{N t} \left( A_{11} - \frac{A_{12}^2}{A_{22}} \right) = \overline{Q_{11}} - \frac{\overline{Q_{12}^2}}{\overline{Q_{22}}} \quad \text{with } \overline{Q_{ij}} = \frac{\sum_{k=1}^N [Q_{ij}^\theta]_k}{N} \quad (4-3)$$

Using CLT is possible to calculate also the Poisson's ratio  $\nu_{lam}$  through Eq. (4-4):

$$\nu_{lam} = \frac{A_{12}}{A_{22}} \quad (4-4)$$

Then, applying ULF the ultimate strength of the lay-ups is calculated. The first laminae to be removed are those at  $90^\circ$ , because they are the first to break. At this point, the ultimate failure for each laminate is obtained without removing any laminae and applying the contour lines correction, the lay-up ultimate stress is calculated. Both model and measured values of Young's modulus, strength and Poisson's ratio are reported in Tab. 13.

Table 13. Comparison between experimental data, and predictions of classical lamination theory, including contour correction

Sample type	Young's modulus (MPa)		Strength (MPa)		Poisson's ratio (mm/mm)	
	Measured	Model	Measured	Model	Measured	Model
[+45/-45] <sub>2s</sub>	--	--	--	--	0.37	0.38
[0/45/-45/90] <sub>s</sub>	1282	1343	9.29	8.36	0.31	0.26
[30/-30/90] <sub>s</sub>	1351	1343	9.98	9.48	0.29	0.26

Concerning [+45/-45]<sub>2s</sub> lay-up, only Poisson's ratio equal to 0.38 from CLT is calculated, using the material constant of Tab. 12, and it is very close to the one that has been measured with DIC (i.e., 0.37). Instead for the two quasi-isotropic lay-ups, both measured Young's modulus and strength are in very good agreement with the theoretical ones, with a maximum deviation of 4 and 11%, respectively. The model tends to slightly underestimate the experimental results, but this is most probably due to the conservative nature of ULF. The values of Poisson's ratio have a higher standard deviation than Young's modulus and strength, with a maximum of 16%.

### 4.3 Conclusions

The strength of 3D-printed parts with PLA filled with wood in simple tension is successfully modeled by CLT coupled with ULF. [0]<sub>4</sub>, [90]<sub>4</sub>, and [+45/-45]<sub>2s</sub> lay-ups have been used to characterize the single lamina, while the other ones are intended for validation in terms of stiffness and strength, using the Tsai-Hill criterion for modeling the breakage of a single 3D-printed layer. Young's modulus and strength, which have been calculated, are in good agreement with the measured ones, especially the 6-lamina quasi-isotropic one. But a better agreement with experimental results can be achieved applying the contour lines correction. Strain at break is also underestimated due to the non-linearity of the stress-strain curves of the various lay-ups. All the results hold for the case of simple tension, interlaminar stresses were not considered. A further development would be to test the laminates in bending and also consider delamination between two consecutive layers as a failure mechanism, due to the weak nature of the interlayer bond.

## CHAPTER V

### 5. COMPACTION AND REMELTING

When using FFF for structural applications, one of the major drawbacks is the mechanical properties of the printed object compared to parts obtained by injection molding [16, 17] and this is due to the inevitable presence of voids and poor filament-to-filament welding [61]. In the last few years, to solve this issue, the scientific literature has mainly focused on the optimization of the printing parameters and in performing some post-printing treatments. The majority of these post-process methods focus on annealing of different materials such as PLA [49, 62, 63, 64, 65, 66, 67, 68, 69], ABS [66, 70, 71], PETG and carbon fiber PETG [63, 72, 73], PPS [74], ASA and cu-PLA [66]. Annealing consists of heating and maintain for a certain period of time the part at a slightly higher temperature than glass transition one, both for amorphous and semi-crystalline polymer, increasing inter-layer bonding and crystallinity, and lowering residual stresses causing an improvement of the mechanical properties (both strength and Young's modulus). However, annealing reduces the problem of intra-layer adhesion, has almost no effect on the presence of voids [49], and can only reduce but not fill the gap of the mechanical properties due to building orientation/raster infill orientation.

If the annealing temperature is higher than the processing temperature (e.g. the melting temperature of a semicrystalline material), a complete remelting of the part is achieved. In such a case, voids would certainly decrease, but dimensional tolerances would be lost. In order to reduce this drawback, a confined remelting could be of some advantage, for example by performing this post-process within a mold made of a granular material, such as powdered salt [75].

In order to improve this procedure even further, it is necessary to study a novel post-process method to enhance the mechanical properties of 3D-printed parts. This post-process consists in compaction and a remelting of the material. To investigate the effectiveness of this post-process, the tensile properties of treated samples have been compared to those of untreated specimens. The samples have been printed with different raster angles infill to estimate the reduction of anisotropy. The same PLA filled with wood of CHAPTER IV also used here, to compare the results and to evaluate if this post-process method is able to reduce the anisotropy of the 3D printed object. Compression-molded samples have also been made, for a better understanding the phenomenon.

---

## 5.1 Experimental

### 5.1.1 Filament material and instruments

A commercial 1.75mm diameter (0.05% tolerance) FFF filament has been purchased from ColorFabb (Belfeld, The Netherlands). The material is named “woodFill” and according to the manufacturer is a blend of poly-lactic acid (PLA) and poly-(hydroxyalkanoate) filled with 15Wt.% fine pinewood fibers. Before printing, the filament has been dried at 80°C for 24h, and during the printing process, the reel has been stored in silica gel.

To weigh the specimens a Mettler model AE 240 has been used, which has a full scale of 205g and a resolution of 0.01mg. To measure the dimensions of the samples both a Mitutoyo 293 micrometer and a digital centesimal caliper have been used. An optical microscope Leica Microsystem (Switzerland) CH-9435 has been used to photograph the specimens.

### 5.1.2 Remelting procedure

An FFF 3D printed object part has a lot of defects such as voids and cold-welding, leading to lower mechanical properties than standard manufacturing techniques such as injection molding. To increase mechanical properties, in terms of stiffness and strength, a post-process method is applied. The melting of the material takes place at different temperatures depending on the material, in fact, if amorphous or semi-crystalline, a temperature of at least  $T_g + 100^\circ\text{C}$  or  $T_m$  must be reached, respectively. Melting the polymer, the sample is distorted, and completely loses its geometrical form and for this reason, a mould must be used.

Post-processing consists of two phases, compaction, and melting of the material and is pictured in Fig. 38. First, fine salt (average particle size  $45\text{ mm} \pm 5\text{ mm}$ ) is pre-heated within an aluminum box (size 200mm x 120mm) at 165°C (measured by a K thermocouple in the middle). Then, the samples are inserted into the mold, focusing to have a planar surface of the salt to avoid samples distortion. A pressure of 10bar is applied and waits until the temperature of the salt reaches 15 – 20°C above  $T_m$ , 185°C in the case of PLA. This temperature is kept for 5 minutes and once the heating is turned off and the samples are extracted when the temperature of the salt is close to ambient temperature. The pressure is maintained until completely cooling down to room temperature to eliminate voids and any defects. The whole procedure takes about one hour for all samples. This method can only be implemented in specimens printed with 100% infill and despite this due to voids and defects in the printed specimen, a reduction of the sample proportional to

the voids is present. Finally, all the surfaces of the samples were cleaned of salt using fine sandpaper.

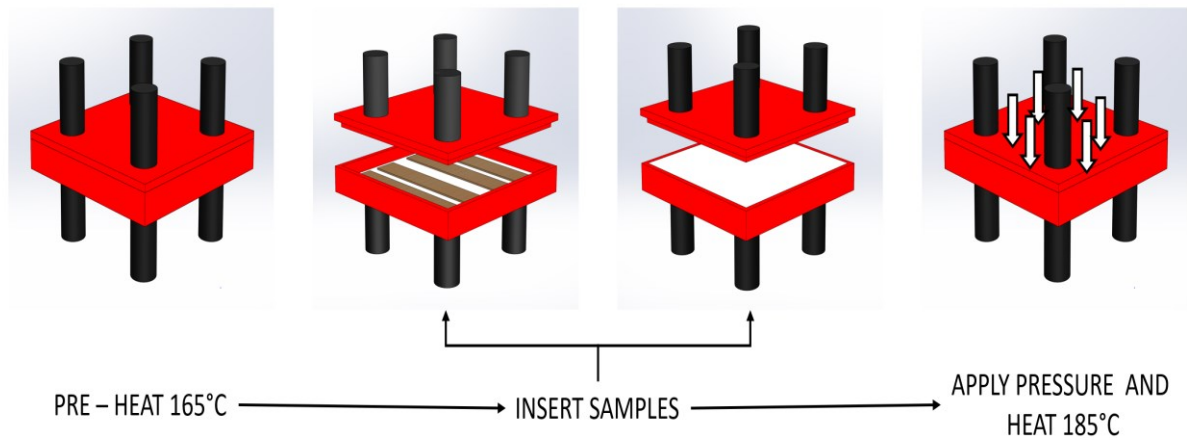


*Figure 38. Post-process procedure*

### 5.1.3 Compression molding part

After drying the wood-filled PLA pellets in an oven at 15 – 20°C below  $T_g$  ( $\sim 55^\circ\text{C}$ ) for 24h, five compression molded samples (Fig. 39) have been made using Collin model P200 E compression molding machine, following ISO 527 type 1A with 1.8mm thickness, due to thermal degradation problem. The overall length, gauge length, and his width are 170mm,75mm, and 4mm, respectively.



*Figure 39. Compression molded specimens of PLA filled with wood*



### 5.1.4 Quasi-static tensile test

Tensile tests have been performed on 3D-printed rectangular samples following ASTM D3039 both as printed and with the post-processing method. The specimens are 200 mm long and 25 mm wide, while the thickness can vary. Rubber tabs, 30 mm long and 25 mm wide have also been used in agreement with the standards. Before testing, the samples have been dried. In addition, compression molded parts following ISO 527 type 1A have been tested. Tensile tests on compression molded samples and lay-ups have been performed at room temperature at 1 mm/min crosshead speed using a universal testing machine (INSTRON 4467, INSTRON, USA) equipped with a 30 kN load cell. Testing has been done on at least five specimens.

### 5.1.5 3D printing

The 3D printer and the calibration test to obtain a good quality of the 3D-printed samples are the same as those of Chapter IV. The printing parameters are also the same but here there are 8 layers instead of 4 in the unidirectional laminates, as reported in Tab. 14. A total of ten lay-up types with 100% raster infill have been printed for each sequence of lamination. Five samples for each laminate are tested as printed while others are post-processed before being tested.

*Table 14. List of tested laminates and their characteristics, the standard deviation is indicated in parenthesis*

Sample type	Number of layers	Thickness (mm)	Width (mm)
[0] <sub>8</sub>	8	3.51 (0.02)	25.1 (0.03)
[90] <sub>8</sub>	8	3.52 (0.02)	25.14 (0.05)
[0/+45/-45/90] <sub>s</sub>	8	3.5 (0.02)	25.27 (0.08)

## 5.2 Results

Two unidirectional and  $[0/+45/-45/90]_s$  quasi-isotropic laminates, following the printing parameters of Tab. 9 in Subsection 4.1.2.2, have been printed and tested. Prior to testing, the samples have been subjected to post-process method described in Section 5.1.2. The graph in Fig. 40 shows the stress-strain diagram of the post-processed laminates and compression molded samples and clearly, the latter has the highest stress and strain at break. All the stress-strain diagrams of the laminates after post-treatment tend to be a single curve, regardless of the raster infill orientation. This basically implies that the post-treated material becomes more isotropic.

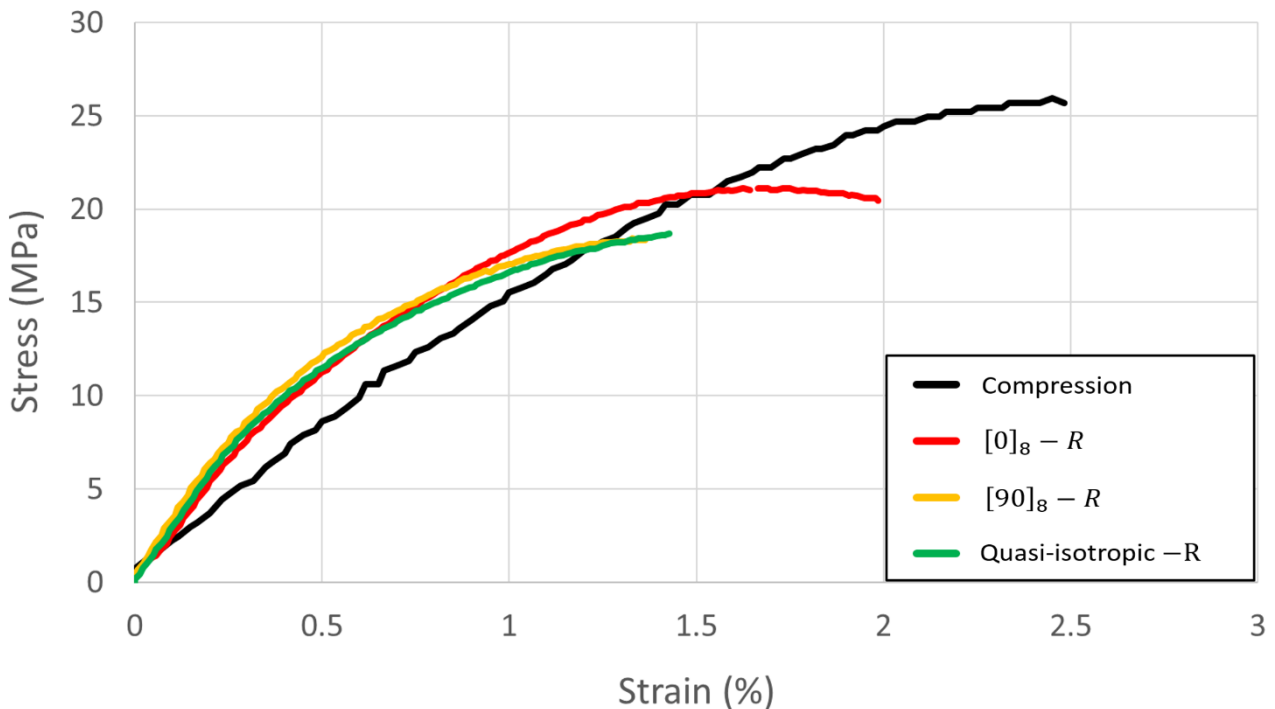


Figure 40. Representative tensile test of the post-processed laminates and compression molded sample

To understand more clearly the behavior of 3D-printed laminates, the Young's modulus, stress, and strain at break are reported in Fig. 41. Post-treated and compression molded specimens have almost the same Young's modulus but present different stress and strain at break. Being a material loaded with short wood fiber, the fibers are laid along the direction of deposition of the extruder, so the strain and stress at break are maximum and minimum respectively in the laminate with fiber at  $0^\circ$  and  $90^\circ$  with respect to the load direction.

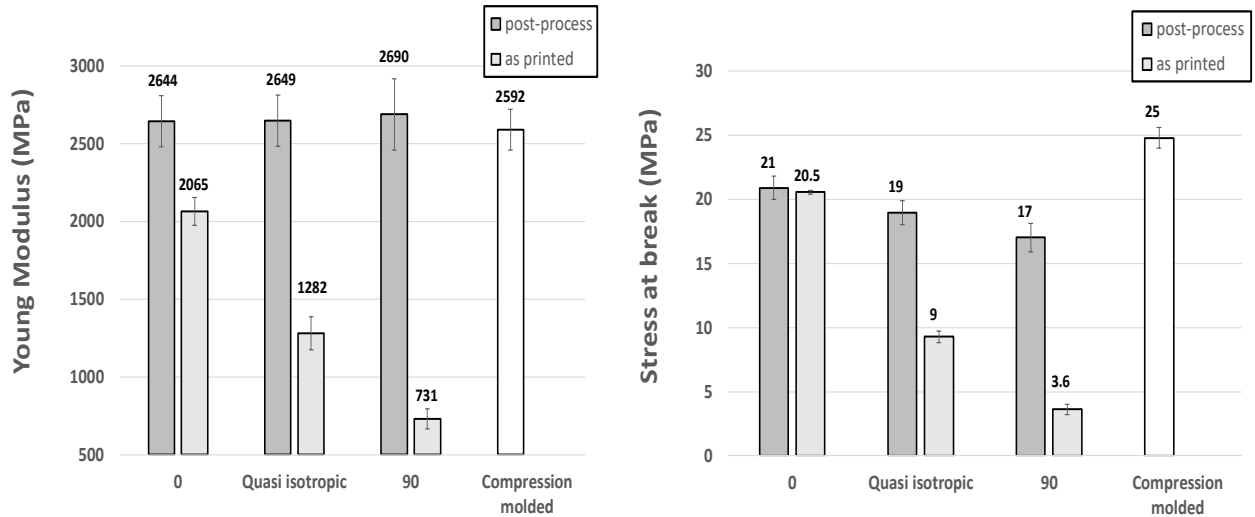


Figure 41. Young Modulus and stress at break of each laminate both post-processed and as printed and compression molded samples. The error bars represent the standard deviation.

The histogram in Fig. 42 shows almost the same density for the post-treatment laminates of about 1.2 g/cm<sup>3</sup> and is very close to the one obtained by compression molding of 1.26g/cm<sup>3</sup>, gives evidence that most of the voids have been eliminated.

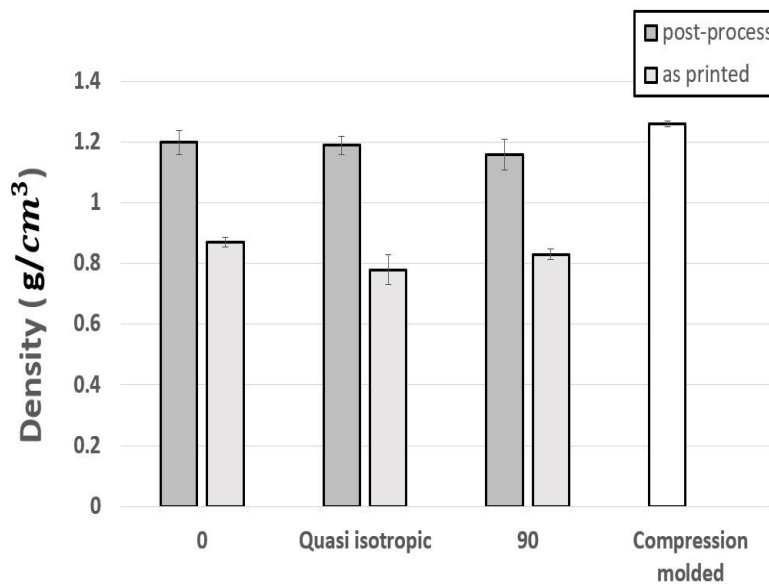
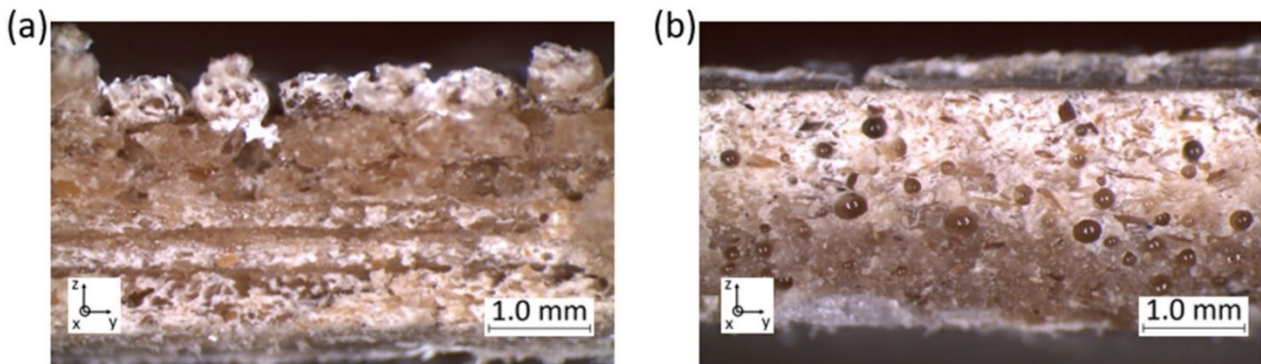


Figure 42. Histogram of the density for each laminate and compression molded samples. The error bars represent the standard deviation.

Nevertheless, not all voids in the laminates have been eliminated after the post-processing method, therefore the compression molded samples present higher mechanical properties.

There is a reduction in the thickness of the samples proportional to the eliminated voids, so it is very important to print as best as possible. In Fig. 43 the fracture surfaces of a symmetric and balanced laminate are pictured before and after the post-method and it is clearly visible the reduction of voids. By comparing Fig. 43-a with Fig. 43-b, a further aspect that can be noticed is that while in the pre-treated sample the stratification is recognizable, the different layers are not identifiable anymore in the post-treated sample.



*Figure 43. Fracture surface of a quasi-isotropic specimen: (a) as printed (b) post-processed*

The stress-strain diagrams both before and after post-processing for each laminate are pictured in Fig. 44. The mechanical properties of pre-treated laminates are maximum when the beads are deposited parallel to the load direction and minimum when the beads are laid transversely [26]. Also in the treated samples, even if in a much less evident way, the stress at break decreases from the  $[0]_8$  to  $[90]_8$  laminates (Fig. 40). A laminate that has been printed with the optimal raster infill orientation, angle parallel to the load direction, have a very low improvement in the properties deriving from post-treatment, as visible in in Fig. 44-a. All layers are aligned parallel to the direction of tensile loading for the  $[0]_8$  laminate, therefore, the effect of the bonding force between the layers is minimized, and the strength is more dependent on the filament properties. The post-treated laminate has a higher Young's modulus and a more brittle behavior due to the higher crystallinity. However, the more we move away from the better configuration, the more the stiffness and strength increase due to the post-treatment, up to almost 380% in the strength of  $[90]_8$  laminate. In contrast to  $[0]_8$  laminate, in the  $[90]_8$  all layers were aligned perpendicular to the direction of tensile loading, so the effect of the intrinsic filament properties is minimized, and the strength depends more on the bonding force between layers. The breaking mechanism can vary after the application of the post-process method. In fact, the  $[90]_8$  laminate from a

brittle fracture due to the poor bonding between beads leads to a yield fracture, as pictured in in Fig. 44-b. Both Young's modulus and stress at break have a large increase from 730MPa to 2690MPa and from 3.6MPa to 17MPa, respectively. Quasi-isotropic laminate due to post-treatment increases both Young's modulus and stress at break more than 100% but shows a more brittle behavior, as pictured in in Fig. 44-c.

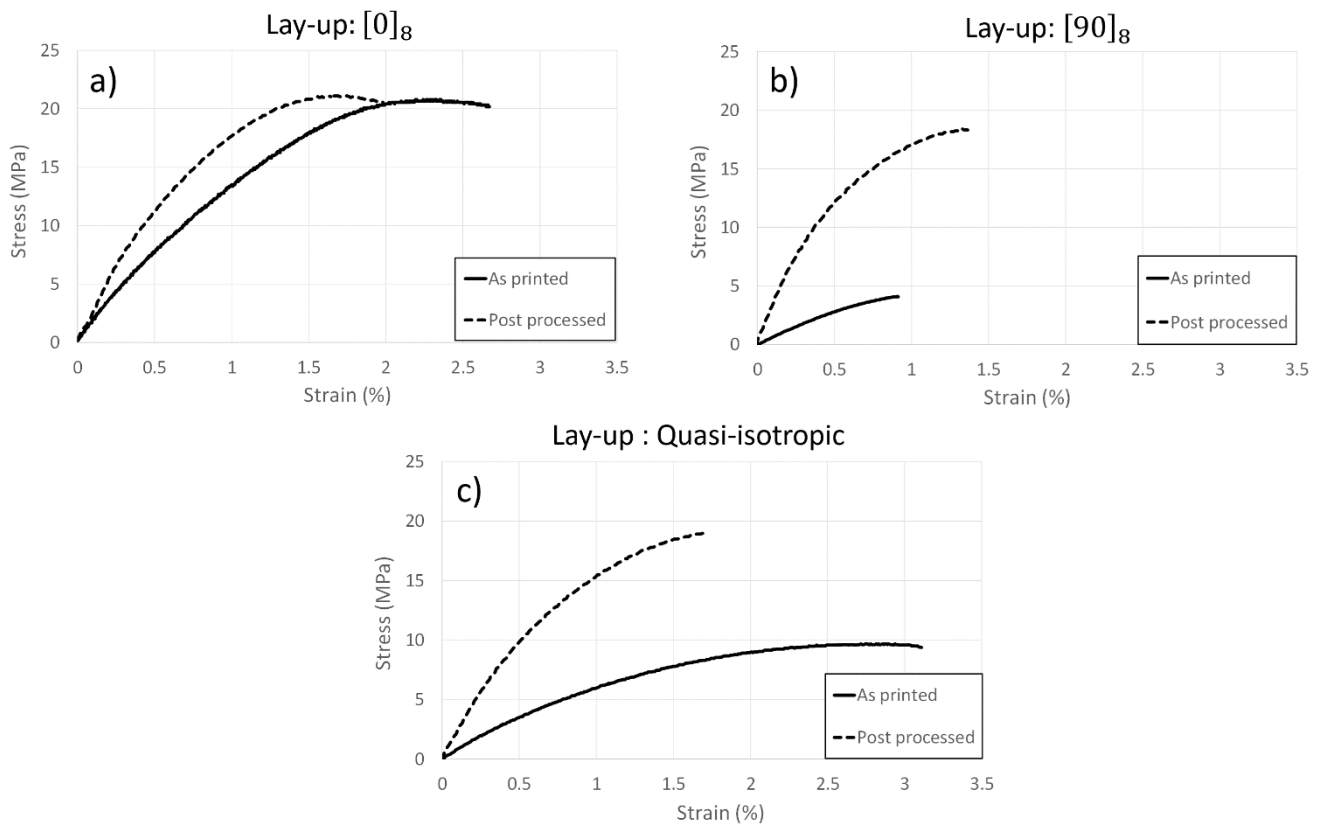


Figure 44. Tensile test comparison between post-processed and as printed of the lay-ups: a) unidirectional  $0^\circ$ , b) Quasi-isotropic and c) unidirectionally  $90^\circ$

---

### 5.3 Conclusions

3D-printed parts have low mechanical properties than injection molded ones, due to the nature of the manufacturing process. A 3D-printed part has several drawbacks, in fact, it is anisotropic, contains voids, and welding between two beads has low properties. A novel post-process method, that consist of melting and compaction, has been successfully applied. It exploits the melting of the material to allow intermolecular diffusion and pressure through compaction to increase the contact surfaces. The post-processing has the greatest effect on the increase in strength of the 3D-printed part and can help to reduce the anisotropy. The influence of this novel method has been investigated based on Young's modulus and the tensile strength. The strength increased in all specimens except for the  $[0]_8$  laminate. Considering the increase of strength in the specimens, this novel method is effective in strengthening the interlayer bonding force of the 3D-printed parts. In the case of toughness, it significantly increased in  $[90]_8$  laminate, thanks to a change in the type of fracture. Compared with the as-built 3D-printed part, based on the considered laminate, Young's modulus and ultimate strength can increase up to 270% and 380%, respectively. However, this process has limitations, such as dimensional distortion and a reduction in the thickness of the samples proportional to the eliminated voids. There are also future works that need to be further investigated both at the method and printing level. Regarding the method, it can be investigated with different pressure, permanence time, and temperatures. Instead at the printing level, it should be interesting to investigate the enhancement of the mechanical properties varying not only the raster infill but also other parameters such as extruder temperature and printing speed. Nevertheless, this can be considered a promising starting point for the development of a new post-processing method.

## CHAPTER VI

### 6. COPPER ELECTROPLATING POST-PROCESS OF 3D-PRINTED PART

A thermoplastic 3D printed object does not have mechanical properties comparable to the same object made of metal, except for some techno polymers filament filled with carbon fibre which, however, cost hundreds of euros per kilo. To reduce this difference also in case of commodities, a thin layer of metal can be deposited on the surface of the printed object.

Usually, polymeric materials are insulating and therefore a 3D-printed object must be made electroconductive before the deposition of a layer of metal [76] through a specific treatment. The main treatments are graphite paint, electroless plating [77], and polypyrrole coating. Graphite painting is the easiest process to perform, on the other hand this treatment is operator dependent, and it is difficult to ensure that paint thickness is uniform. Electroless plating directly plates the surface of the object, making it electrically conductive. This technique is the most difficult to perform because it requires several steps such as etching, neutralization, activation, and acceleration and this ensures the best interface between metal and plastic layers. On the other hand, the chemical products are often not easily available and sometimes toxic [78]. In this work the treatment with polypyrrole [79] has been chosen for simplicity.

After this treatment, the surface of the 3D printed object is electroconductive, a layer of metal can be deposited through various techniques such as brushing metal paint, electroless plating, electroplating and electroforming. Among all techniques, electroplating has been chosen because it has a straightforward procedure and can deposit a layer of metal up to  $500\mu\text{m}$ . If only few microns of metal are deposited, the metal coating acts as protection, while increasing the thickness, it can also become a structural reinforcement.

In this work, the metal that has been deposited via electroplating is copper because it is easily available, and the process does not require too expensive materials. Copper permits to increase both the resistance to corrosion, the stiffness and the strength. To evaluate the effectiveness of this method, the electroplating process has been applied on 3D-printed ABS samples with raster infill varying from 30 to 100 percent. The object can be printed with a certain infill based on the desired mechanical properties, which in turn depend on the type of application.

### 6.1 Copper electroplating process

To perform electroplating an electrochemical cell is necessary and it consists in three main components:

1. Anodes: are the regions with more electrostatic potential energy and they are connected to the positive connection of the power supply.
2. Cathode: is the object that it needs to be electroplated with less electrostatic potential energy and this is connected to the negative connection of the power supply.
3. Electrolytic bath: is made with two main components that are a solution of copper sulphate ( $\text{CuSO}_4$ ) and sulfuric acid ( $\text{H}_2\text{SO}_4$ ). For better plating, some additives can be added such as brightening, purifying and levelling [80, 81]. The electrolytic bath should have a stable temperature at  $20^\circ\text{C}$ , pH around 4, and chemical composition over time to avoid variations in the characteristics of the deposit and a reduction in the performance of the process. Copper plating in acid baths are optimized at pH around 3.8 to 4.2 and difficulties occur at pH above 5.

A typical electrolytic cell is pictured in Fig. 45 and the result is the deposition of a layer of metal on the surface of the object attached to the negative connection of the power supply through a reduction process, in which the copper atoms in the solution lose and acquire electrons.

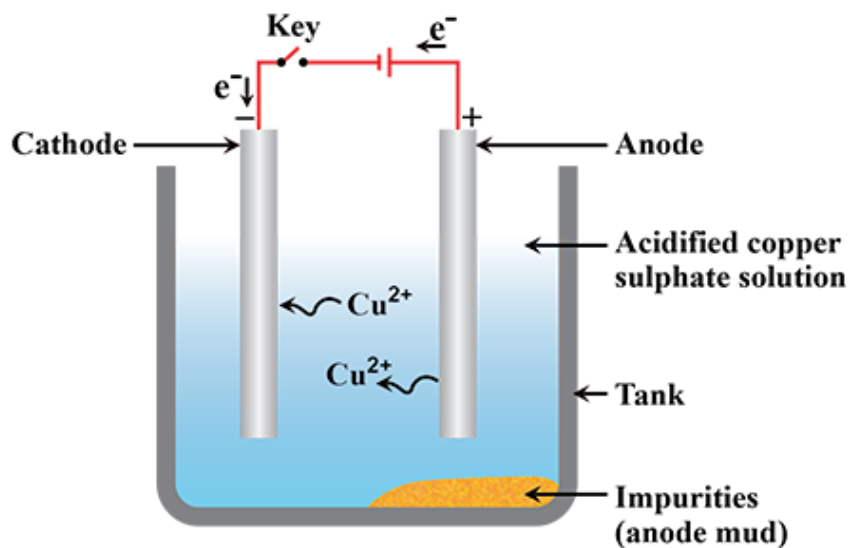


Figure 45. Electrolytic cell: components and reactions



---

In an electrochemical cell, due to an external force from the power supply, the potential energy of the electrons of the cathode increases to a value that is higher than the energy of the anode.

The copper of the anode loses two electrons, which move to the cathode, and becomes a  $\text{Cu}^{2+}$  cation.  $\text{CuSO}_4$  (copper sulphate) dissolved in solution breaks its ionic bond, dividing into the  $\text{Cu}^{2+}$  cation and the  $\text{SO}_4^{2-}$  anion. The  $\text{SO}_4^{2-}$  anion binds with the  $\text{Cu}^{2+}$  cation that formed at the anode and turns back into  $\text{CuSO}_4$  copper sulphate. The  $\text{Cu}^{2+}$  cation, that was part of the copper sulphate, initially dissolved in the solution moves to the cathode and deposits on the object.

The bath contains an equal number of particles charged both negative and positive. Thanks to the energy of the power supply, the anions and cations move to anode and cathode, respectively. The sum of all these ions in both directions produces a current flow equal to the flow produced by the power supply. The concentration of copper sulphate in the solution remains unchanged because the copper atoms that the bath yielded to the cathode were replaced by the atoms it received from the anode. The reaction involves a transfer of copper: the copper of the anode leaves the electrode and binds to the copper sulphate dissolved in the solution, while the copper of the copper sulphate leaves the solution and settles on the cathode. Other reactions can also occur at the anode depending on the voltage difference with the bath: for example, water molecules or hydroxide ions can be oxidized to gaseous oxygen. In the electroplating process, there are some important variables that influence the distribution of the metal coating, and they can be divided into three groups: bath, electrode, or current related. Concerning the bath, it is important to control the quality of the components and their additives such as level agents, anti-pitting, and brighteners. Other parameters to pay attention are the temperature of the bath and his agitation and filtration.

Regarding the electrodes, it is fundamental to check not only the quality, shape, and dimensions but also their position and cleaning. The velocity of deposition together with the morphological structure is controlled by the current flow applied by the power supply. A typical value of current has a density between 10-30  $\text{mA}/\text{cm}^2$  and a high value lead to fine grains. The current must not be too high, because it produces rough grains and the hydrogen reduction on the cathode, ruining the coating with internal stresses. To calculate the time necessary to obtain a certain amount of metal deposited on the object with a fixed current flow, Faraday's law must be used and is described in the following paragraph.

### 6.1.1 Faraday's law

In order to foresee the time to deposit a certain mass of copper on the 3D printed object it is necessary to use Faraday's law, which follows these two points:

1. The mass of a certain substance produced or consumed by an electrode is proportional to the quantity of electrical charge named current intensity that passed through the cell. The current intensity is measured by Ampere and is the quantity of charge that flows in the circuit in a second.
2. The passage of a given amount of electric charge through the cell produces or consumes equivalent masses of different substances at the electrodes.

The elementary charge of an electron  $e$  is equal to  $1.602 \times 10^{-19}$  C. The amount of charge of a mole of electrons  $Q$  follows Eq. (6-1):

$$Q = N_A e = \left(6.0221420 \times 10^{23} \left[\frac{1}{mol}\right]\right) (1.602 \times 10^{-19} [C]) = 96485.34 \left[\frac{C}{mol}\right] \quad (6-1)$$

Where  $N_A$  is the Avogadro constant, equal to the number of particles in a mole.  $Q$  is called "Faraday's constant" and is denoted by the letter "F".

It follows that the total charge through a circuit is represented by Eq. (6-2):

$$Q_{tot} = i t \quad (6-2)$$

where  $i$  is the current intensity and  $t$  the time. For the calculation of the moles of electrons transferred, it will be sufficient to divide the  $Q_{tot}$  value by the Faraday constant  $F$ . Using these formulas is possible to calculate the number of moles and therefore the grams of reagents consumed and the products formed during the electrochemical reactions [82].

---

## 6.2 Experimental

### 6.2.1 Materials and instrumentations

The vast majority of articles have been made using ABS as the reference material, and for this reason ABS has been used. A commercial 1.75 mm diameter (0.05% tolerance) FFF filament has been purchased from SUNLU. The filament is transparent, and this indicates the absence of colour masterbatch that can affect the mechanical properties of the 3D printed part. Before printing, the filament has been dried at 80°C for 24h, and during the printing process, the reel has been stored in silica gel.

In order to make the 3D-printed part electroconductive, pyrrole has been purchased from Sigma-Aldrich. To perform electroplating copper sulphate solution and copper anode (99.9% pure) has been bought from P.C.M. Chimica. The anodes are two 100mm x 50 mm copper plates with a thickness of 5mm.

A Mettler model AE 240 has been used to weigh the specimens, which has a full scale of 205g and a resolution of 0.01mg. To measure the dimensions of the samples both a Mitutoyo 293 micrometer and a digital centesimal caliper have been used. An optical microscope Leica Microsystem (Switzerland) CH-9435 has been used to photograph the specimens.

### 6.2.2 3D printing

#### 6.2.2.1 3D printer and calibration test

An AnyCubic model i3 Mega S 3D printer has been used and is pictured in Fig. 46. The build volume is 210mm x 210mm x 205mm, and this printer is equipped with a bowden extruder. Thanks to the installation of the Octoprint program on a single-board Raspberry Pi4 computer, the printer can be control remotely, which simplifies the printing process and makes it possible to change the process parameters during the construction of the part. If the part is printed with fiber-filled plastic, e.g. fiberglass or carbon, the brass nozzle should be replaced with one made of hardened steel. Before printing the samples, the same calibration test described in Subsection 4.1.2.1.1 has been done.

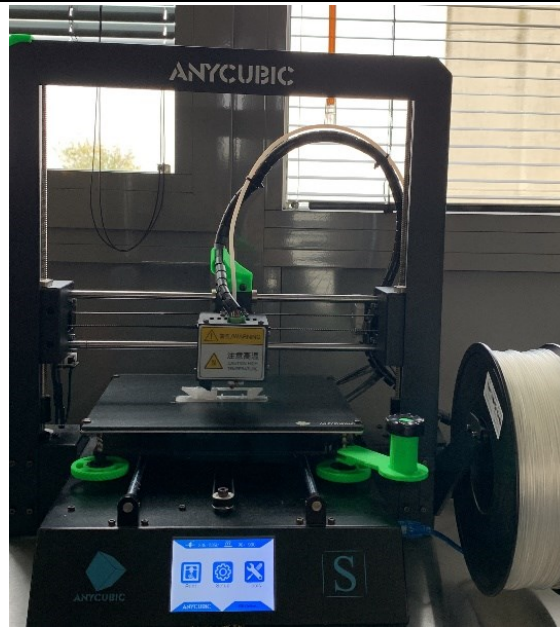


Figure 46. Anycubic i3 Mega S 3D printer

### 6.2.2.2 Printing parameters

Anycubic i3 Mega S is equipped with a 0.4mm nozzle height. The 3D-printing parameters for the samples are reported in Tab. 15.

Table 15. Processing parameters to print various samples.

Parameters	Values	Parameters	Values
Layer height (mm)	0.25	Bed temperature (°C)	105
Line width (mm)	0.4	Raster infill (%)	30 - 100
Nozzle diameter (mm)	0.4	Printing speed (mm/s)	15
Nozzle temperature (°C)	247	Contour lines	0

To characterize ABS samples, the UNI EN ISO 178 standard for flexural tests has been chosen. The sample dimensions are 120mm x 10mm x 4mm and laminates are unidirectional 0°, 90° and  $\pm 45^\circ$  symmetric and balanced. The unidirectional 90° laminate have been printed also with 115% of flow rate. Moreover, specimens with a raster infill of  $\pm 45^\circ$  and a percentage of infill variable between 30% up to 70%, with steps of 10%, have been printed. For each type of laminate, six specimens have been printed. Three are subject to bending tests as printed, while the others have been electroplated before the test.

### 6.2.3 Deposition of an electroconductive layer on the surface of 3D printed object

This pretreatment consists of a deposition of a thin layer (a few microns) of polypyrrole (PPy) obtained from the polymerization of pyrrole (Py), reported in Fig. 47. Pyrrole is a five-term heterocyclic aromatic compound, and its formula is  $C_4H_5N$ . At room temperature it is a colorless and flammable liquid, it is partly soluble in water but soluble in ether, alcohol, and in other common organic solvents. Pyrrole is an electrical insulator, while polypyrrole that is obtained from the oxidative polymerization of pyrrole [83, 84], is a good electrical conductor. The conductivity of the material depends on the conditions and reagents used in oxidation and typically ranges from 2 to 100 S/cm.

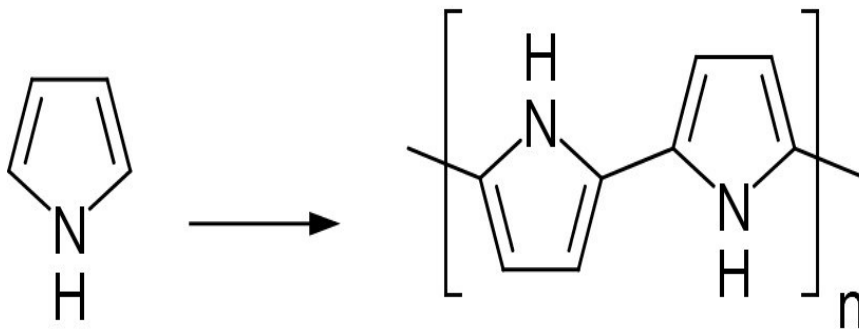
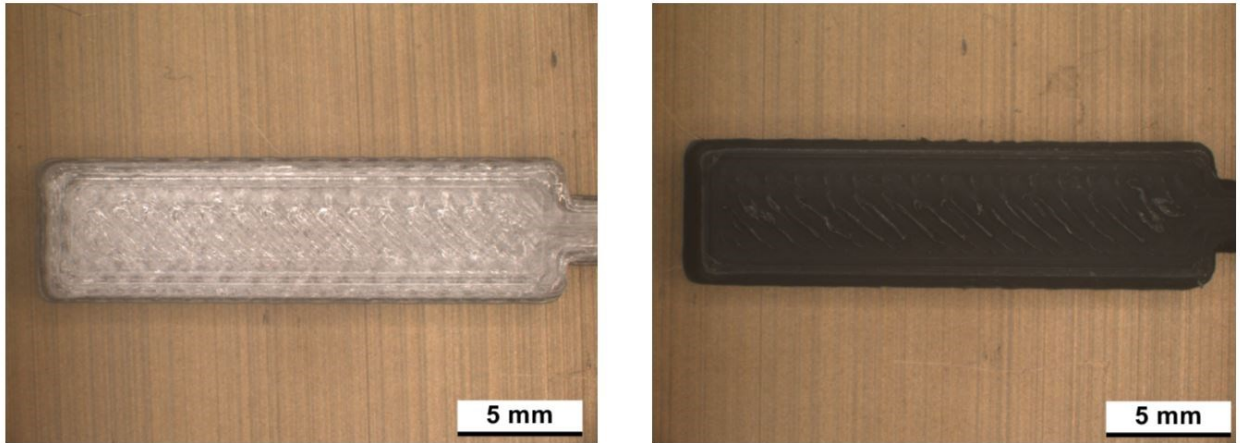


Figure 47. Polymerization of Py in PPy

To obtain a thin layer of polypyrrole the routine below has been applied:

- 1) Preparation of solution 0.6M of Pyrrole
- 2) Preparation of solution 0.9M of  $FeCl_3$
- 3) Deposition and polymerization of Py on the surface of 3D printed object:
  - Cleaning sample with ethanol
  - Blowing sample with compressed air and dry it before weighing it
  - Immersing 3D printed object in 0.6M solution of Py and turn it over after 5min
  - After 10 minutes adding a solution of 0.9M  $FeCl_3$ . The ratio is one 0.9M  $FeCl_3$  to three 0.6M Py. If too much  $FeCl_3$  is add, the polymerization is accelerated, and it can polymerize in the solution rather than on the surface of the 3D-printed object.
  - Start the oxidative polymerization reaction of pyrrole:
 
$$nPy + 2.33nFeCl_3 \rightarrow (Py^{+0.33} + 0.33 Cl^-)_n + 2.33nFeCl_2 + 2nHCl$$
 (6.2-1)
  - After 30min extracting and cleaning the samples

- 4) Repeat the same procedure of point 3) to have a homogeneous layer of PPy on the 3D printed part. The samples have been dried and weight to measure the mass of PPy being deposited. The aspect of the part is the same as the 3D printed object with black colour, and this difference can clearly be seen in Fig. 48.



*Figure 48. Sample as-printed and coated with a layer of PPy*

#### 6.2.4 Electroplating process

The cell that has been used is pictured in Fig. 49 and contains the electrolytic bath, the cathode, and the anode. The temperature of the bath is around 22°C. The cathode is the 3D printed part coated with a few microns of polypyrrole (PPy), while the anodes are two 100mm x 50mm copper plates with a thickness of 5mm, placed parallel to each other with a distance between the 3D print object's surfaces of about 60mm. To maintain this constant distance, a special FFF printed support has been made. Threaded M2 holes have been made on the anodes to attach them to the cables, which will come out of the holes in the closure of the box. A power supply Model 273A in control of current has been used and connected the negative and positive pole to the cathode and anode, respectively. The controlling software that has been used is Powersuite. Two tubes are inserted into the bath and filtered compressed air has been pumped into it to agitate the bath in order to ensure the recirculation of a new solution and to have a uniform plating without holes.

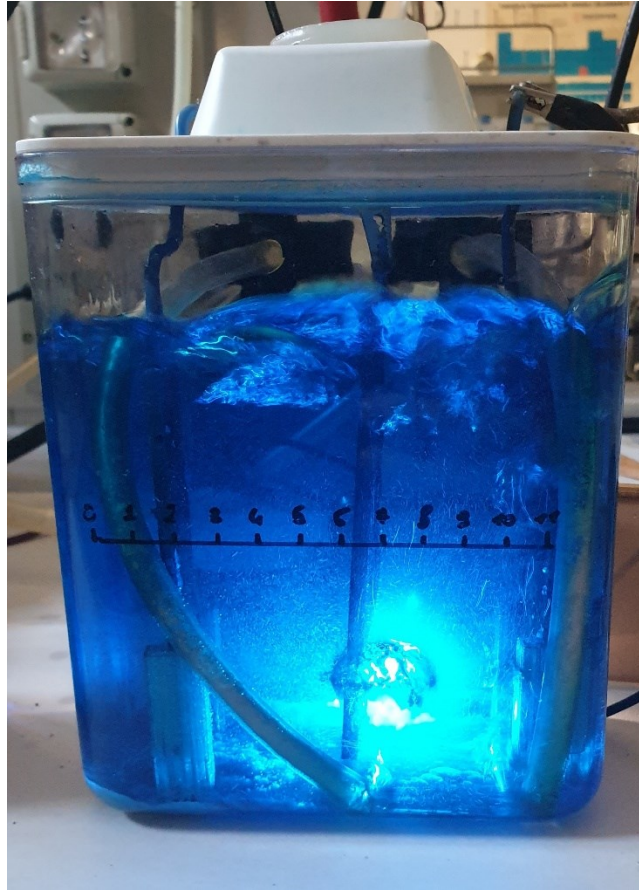


Figure 49. Electrolytic cell

The current density, applied by the power supply is  $10\text{mA}/\text{cm}^2$  and this is a reasonable value to achieve both the quality and the velocity of the process. Through the multiplication of the 3D-printed sample surface by the current density, the current  $i$  applied by the power supply is obtained.

To estimate the time needed to deposit a certain thickness  $\delta$  of copper on a specimen, it is necessary to identify the reduction reaction that takes place at the cathode through Eq. (6-3):



To calculate the surface  $S$  of the 3D printed samples to be electroplated a python program has been used that derives the STL of the part. Finally, fixed the amount of thickness  $\delta$  to be deposited at  $0.1\text{mm}$ , can be calculated the mass to be deposited  $M_{\text{Cu}}$  applying the following equation:

$$M_{\text{Cu}} = S \delta \rho_{\text{Cu}} \quad (6-4)$$

Where the density of the copper  $\rho_{\text{Cu}}$  is equal to  $8.96 \cdot 10^{-3} \text{g}/\text{mm}^3$ .

After that, converting the value of the mass in grams into the number of copper moles to be deposited, and knowing that 2 electrons are needed to reduce 1 mole of  $Cu$ , it is possible to calculate the amount of total charge needed  $Q_{tot}$  follows Eq. (6-5):

$$Q_{tot} = 2 \frac{M_{Cu}}{m_{Cu}} F \quad (6-5)$$

Where,  $M_{Cu}$  is the mass in grams of one mole of  $Cu$  equal to 63.546 g/mol and  $F$  is the Faraday's constant. At this point, by reversing the Eq. (6-2) and assuming to apply a certain current intensity  $i$ , the time  $t$  necessary to deposit the necessary copper moles is calculated and Eq. (6-6) is obtained:

$$t[s] = \frac{Q_{tot}}{i[A]} \quad (6-6)$$

During plating a current density of 10 mA/cm<sup>2</sup> has been applied, while in the first 10min of the process, to start plating more uniformly only 1mA/cm<sup>2</sup> has been used. The final part is a 3D printed object coated with a layer of copper, an example is reported in Fig. 50.

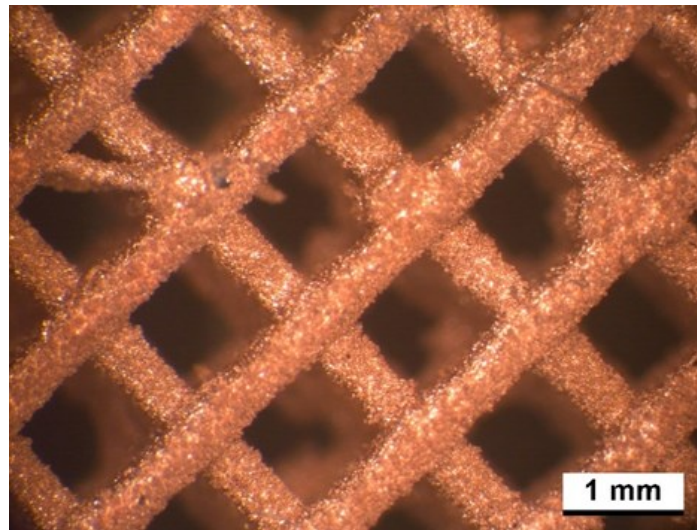


*Figure 50. 3D-printed electroplated part*

### 6.2.5 Quasi-static bending test

Bending tests have been performed on 3D printed samples both as printed and electroplated. As specific bending testing standards are not available for 3D printed materials, UNI EN ISO 178 has been used. Bending test on all the specimens has been performed, after drying for 24h, at room temperature at 1mm/min crosshead speed with a 500N load cell using the INSTRON 4467. The span has been 70mm.



## 6.3 Results

### 6.3.1 ABS as printed with 100% infill

The as-printed laminates that have been tested are reported in Fig. 51 and all the curves have an elastoplastic behavior, with an elastic zone until around 0.025 of strain. They present a plastic zone until 0.07, except for the unidirectional 90° laminate that fails immediately after the elastic zone, due to lower filament-to-filament welding properties. The curves are very similar, showing that the laminates have been printed well.

The mechanical properties in terms of Young's modulus, strength, and strain at break are reported in Tab. 16. Young's modulus is almost the same, while the ultimate stress and strain vary depending on the specific laminate. Stress and strain at break of the unidirectional 0° laminate are maximum, while are minimum with the 90°. However increasing the flow up to 115%, the unidirectional 90° laminate has significant improvement in the stress and strain at break. The fracture mechanism changes from brittle to ductile, thanks to the improvement of bead-to-bead welding properties. In fact, due to larger flow, the laminate has been printed like with a negative air gap between two consecutive bead. Due to the different fracture mechanism, can be obtained different mechanical properties, fragile in the case of unidirectional 90° laminates at 100% flow and ductile in the other case.

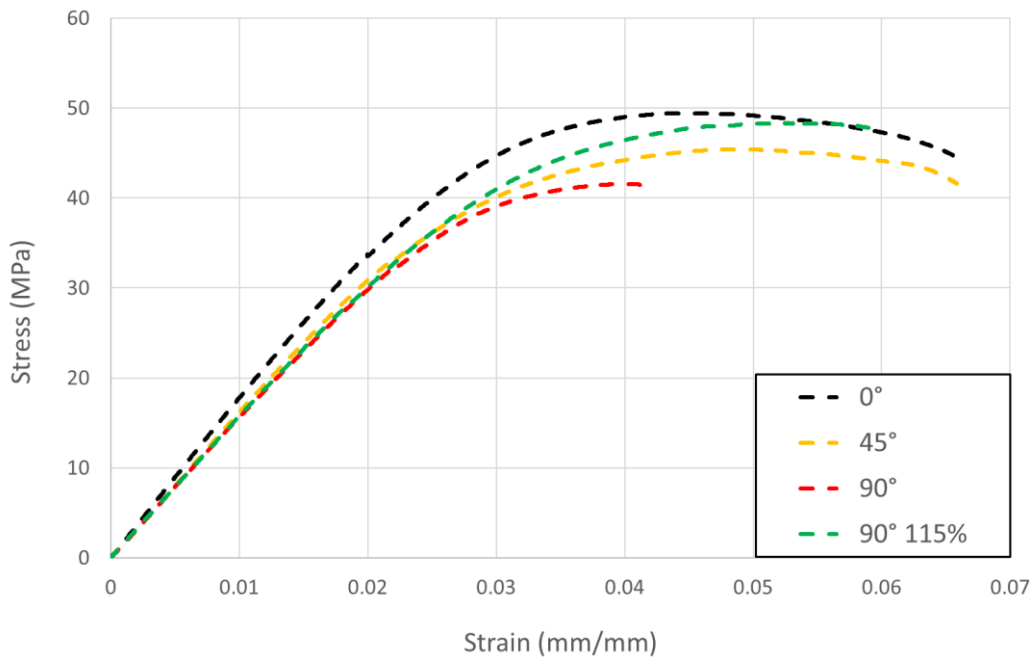


*Figure 51. Representative stress-strain of the as-printed laminates with 100% infill at different raster angle*

*Table 16. Experimental results of the bending tests on the as-printed laminates with 100% infill density: Young's modulus, strength and strain at break. The numbers in parenthesis represent standard deviation*

<b>Sample type</b>	<b>Young's modulus (MPa)</b>	<b>Strength (MPa)</b>	<b>Strain at break (mm/mm)</b>
<b>0°</b>	1801 (21)	50.1 (0.8)	0.065 (0.005)
<b>±45°</b>	1582 (39)	44.7 (0.6)	0.07 (0.002)
<b>90°</b>	1616 (50)	41.6 (0.9)	0.04 (0.001)
<b>90° 115% flow</b>	1555 (43)	48.2 (0.4)	0.058 (0.002)

With FFF technique it is not possible to obtain a completely filled object (100%). In Tab. 17 are reported the density for the filament and for each laminate and they are in good agreement with the mechanical properties. In fact, increasing the density also the mechanical properties of the laminates are higher. In the case of unidirectional 90° laminate, it is evident that the one printed with a flow of 115% has higher density and therefore much greater mechanical properties.

*Table 17. Density and voids of the as-printed laminates with 100% infill density at different raster angle. The numbers in parenthesis represent standard deviation.*

<b>Sample type</b>	<b>Density (g/cm<sup>3</sup>)</b>	<b>Voids (%)</b>
<b>Filament</b>	1.07 (0.01)	0
<b>0°</b>	1.00 (0.02)	6.9
<b>±45°</b>	0.97 (0.01)	8.9
<b>90°</b>	0.97 (0.01)	9
<b>90° 115% flow</b>	1.00 (0.01)	6.7

### 6.3.2 ABS plated with 100% infill

The stress-strain curves of the unidirectional  $90^\circ$  and  $0^\circ$  laminates have been and pictured in Fig. 52, The calculation of the stress vs. strain has been chosen instead of load-displacement although the samples are made up of inhomogeneous material, in particular copper outside and ABS inside. In this way they can be compared with the curves obtained previously, with some necessary simplifications.

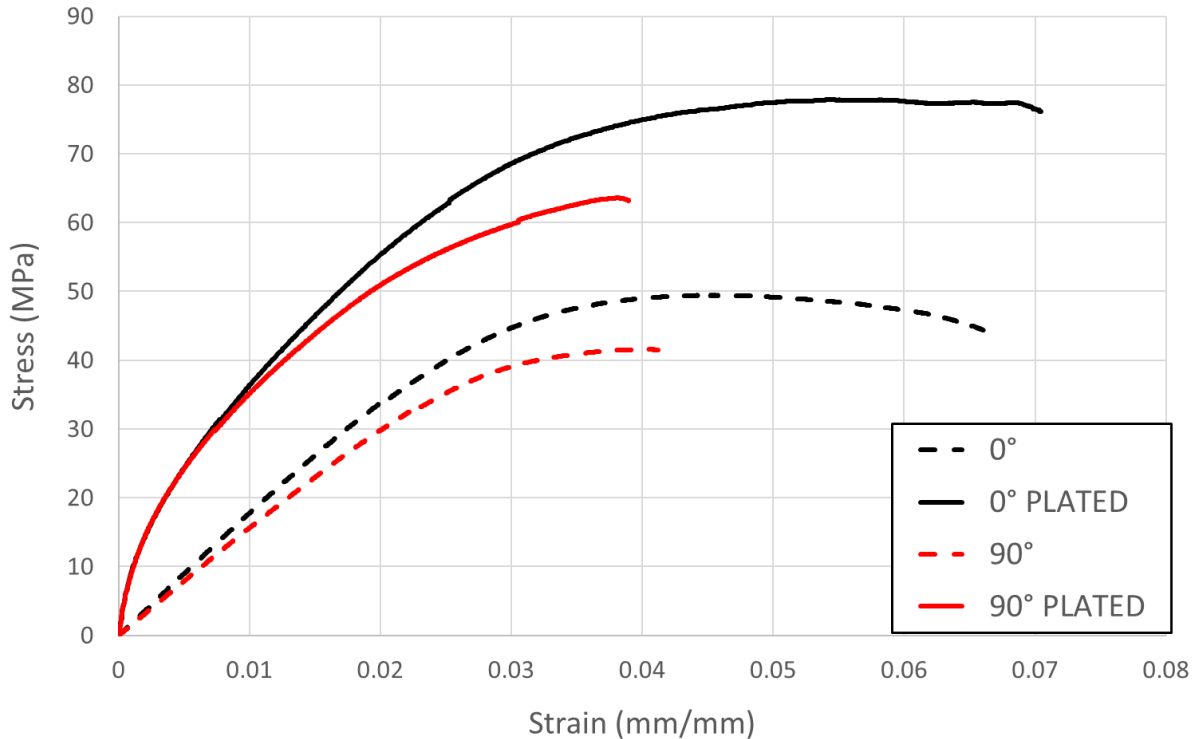


Figure 52. Representative stress-strain of as-printed and post-processed unidirectional  $0^\circ$  and  $90^\circ$  laminates with 100% infill density

The same curves have been obtained from a qualitative point of view but shifted upwards. Mechanical properties and the weights are reported in Tab. 18. Young's modulus is approximately the same for the two plated samples and is four times greater than the as-printed ones, due to the thickness of copper deposited of about 0.1mm. The maximum stress increases from 50MPa up to 79MPa and from 42MPa up to 64MPa for  $0^\circ$  and  $90^\circ$  laminates, respectively. However, for both laminates, the strain at break remains almost the same. Attention must be paid to the weight of the specimens, as this has increased by about 80% from 4.5 to about 8g. Therefore, if values are normalized with respect to weight, there would be a gain only in Young's modulus which approximately doubles.

*Table 18. Experimental results of as-printed and post-processed unidirectional 0° and 90° laminates with 100% infill density: Young's modulus, strength, strain at break and weight.*

*The numbers in parenthesis represent standard deviation.*

<b>Sample type</b>	<b>Young's modulus (MPa)</b>	<b>Strength (MPa)</b>	<b>Strain at break (mm/mm)</b>	<b>Weight (g)</b>
<b>0°</b>	1801 (21)	50.1 (0.8)	0.065 (0.005)	4.47 (0.02)
<b>90°</b>	1616 (50)	41.6 (0.9)	0.040 (0.001)	4.54 (0.02)
<b>0° Plated</b>	7319 (802)	79 (2.2)	0.058 (0.005)	7.91 (0.09)
<b>90° Plated</b>	7870 (329)	64 (0.3)	0.037 (0.0026)	8.48 (0.07)

### 6.3.3 ABS with variable raster infill

Specimens with variable infill between 30% and 70% and raster infill angle of 45° have been printed to evaluate the effectiveness of the electroplating process. Load-displacement instead of stress-strain curves of pre-treated samples are chosen and shown in Fig. 53, because the objects have different densities based on the infill density percentage used, thus the material cannot be considered homogeneous. The samples that have been printed are pictured in Fig. 54. All the curves have an elastoplastic behavior, with an elastic zone until around 4mm of displacement. They present plastic zone until around 13mm, except infill density of 60% and 70% up to 16mm.

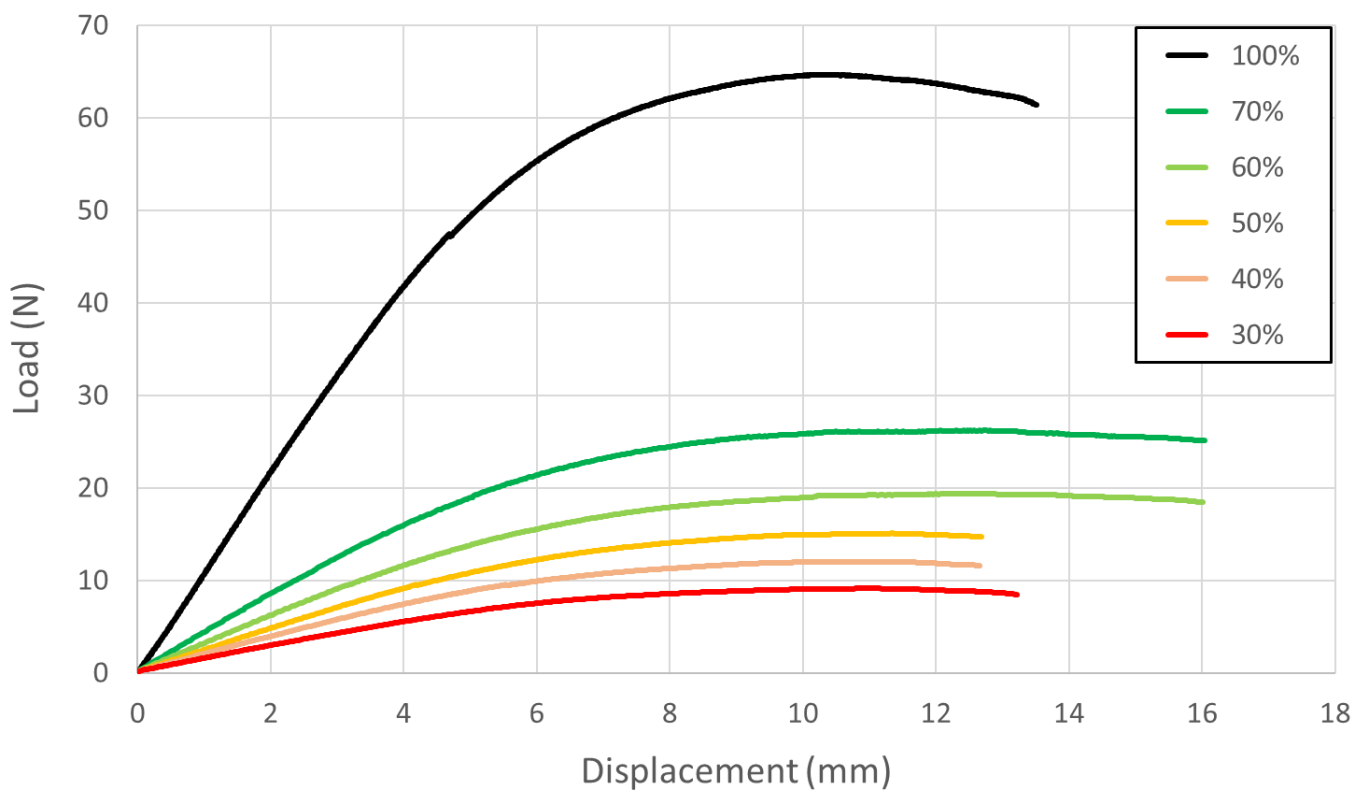


*Figure 53. Representative load-displacement of the as-printed laminates with different infill density percentage and raster angle of 45°*

The mechanical properties are reported in Tab. 19. As the infill density increases, mechanical properties in terms of rigidity, maximum load, and displacement at break increase, with the exception of the displacement at break in the laminate at 100% infill density. Increasing the infill density, also if the results are normalized with respect to the weight, the mechanical properties increase.

Table 19. Experimental results of the bending tests on the as-printed laminates with different infill density percentage: Rigidity, maximum load, displacement at break and weight. The numbers in parenthesis represent standard deviation.

Infill (%)	Rigidity (N/mm)	Maximum load (N)	Displacement at break (mm)	Weight (g)
30%	1.47 (0.04)	8.96 (0.16)	11.99 (1.09)	2.75 (0.01)
40%	1.90 (0.01)	11.75 (0.23)	12.77 (0.20)	3.07 (0.01)
50%	2.33 (0.02)	15.03 (0.13)	13.46 (0.69)	3.38 (0.01)
60%	3.07 (0.04)	19.60 (0.21)	15.55 (0.78)	3.68 (0.01)
70%	4.22 (0.09)	25.75 (0.44)	15.85 (0.36)	3.99 (0.01)
100%_45°	10.32 (0.20)	64.05 (0.62)	13.50 (0.20)	4.54 (0.02)

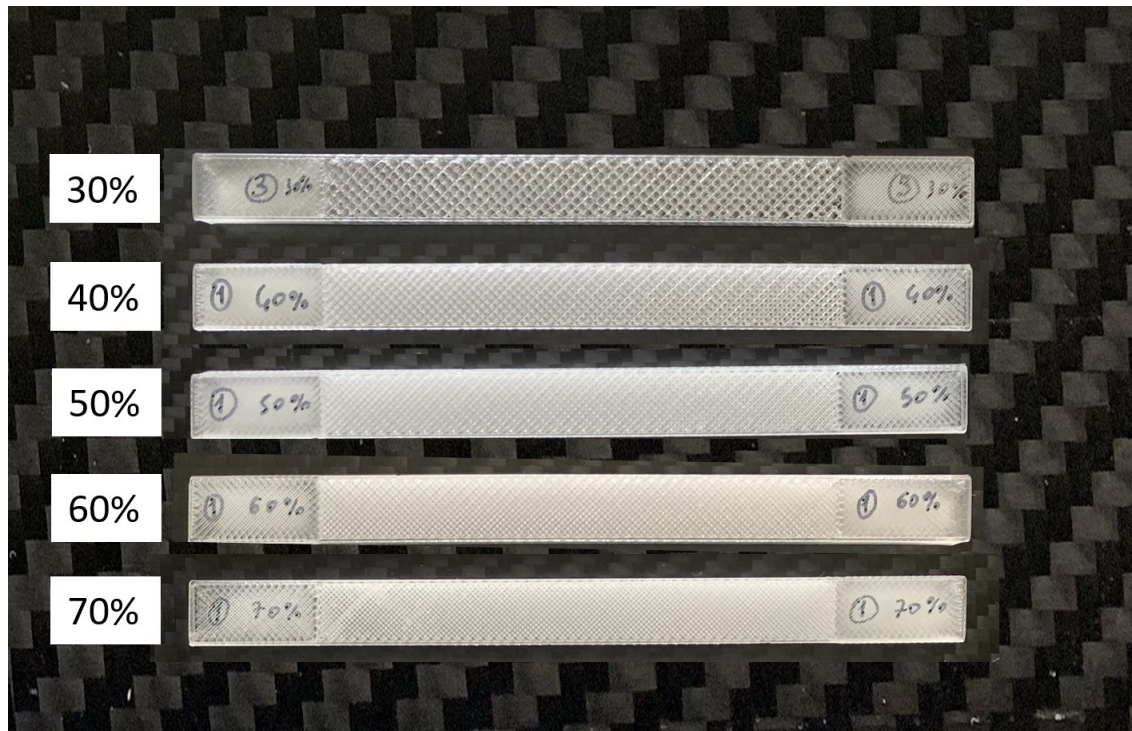


Figure 54. Laminates with different infill density from 30% to 70%

### 6.3.3 Plated ABS with variable raster infill

The load-displacement curves of the ABS specimens plated with different infill density percentage and raster angle of  $45^\circ$  are shown in Fig. 55. An increase in stiffness and strength from 30 to 70% of infill density is clearly visible, while the curve at 100% has different behavior. Sample at 100% infill density has been plated only externally and not internally like all the other laminates. Except for 100% infill density, as infill density increases, the rigidity and the maximum load increase while the displacement has no definite trend and remains quite the same.

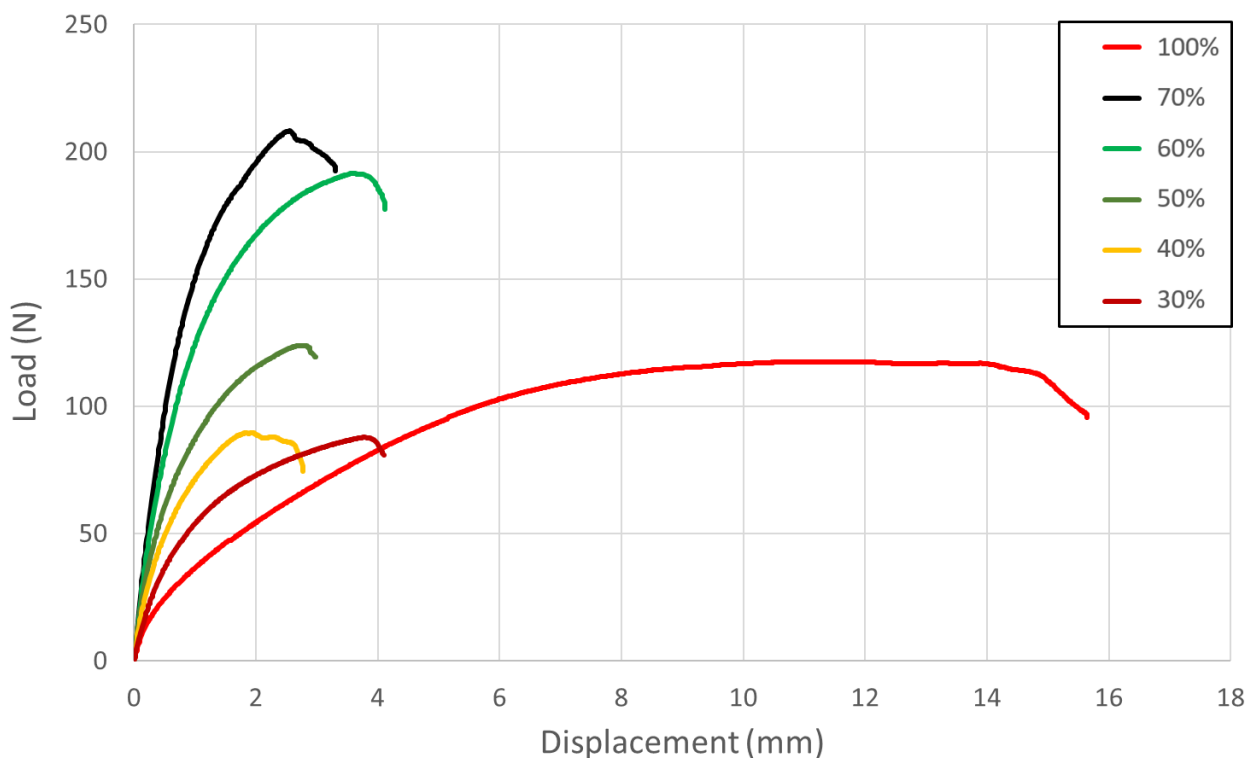


Figure 55. Representative load-displacement of the post-processed laminates with different infill density percentage and raster angle of  $45^\circ$

The goal is to plate a thin 0.1mm layer of copper on the surfaces of the 3D-printed sample. Maximum load and the weights of the coated laminate and copper deposited are reported in Tab. 20. The weight of copper deposited is in good agreement with the theoretical one in laminates with infill at 30%, 40%, and 100%. Instead, the weight of deposited copper deviates more and more from the theoretical value and there is a plateau of about 11.5 g in the laminates with an infill from 50% up to 70%. Except for the 100, 70 and 60% infill, the

copper can cover all surfaces evenly, as shown in Fig. 56. The top and bottom part for each plated laminate, are pictured in Fig. 57.

*Table 20. Experimental results of the bending tests on the post-processed laminates with different infill density percentage: Rigidity, maximum load, total weight and copper weight. The numbers in parenthesis represent standard deviation.*

Infill (%)	Rigidity (N/mm)	Maximum load (N)	Laminate and coating (g)	Copper deposited (g)	Copper theoretic (g)
30%	93 (4)	79 (12)	12.61 (0.22)	9.87 (0.2)	9.77
40%	108 (15)	94 (16)	14.23 (0.2)	11.18 (0.18)	11.51
50%	143 (11)	126 (10)	14.79 (0.03)	11.45 (0.04)	13.22
60%	207 (10)	179 (16)	15.06 (0.01)	11.42 (0.01)	14.21
70%	225 (3)	205 (13)	15.72 (0.3)	11.77 (0.3)	15.11
100%_0°	59 (8)	120 (2)	7.91 (0.09)	2.94 (0.08)	2.95

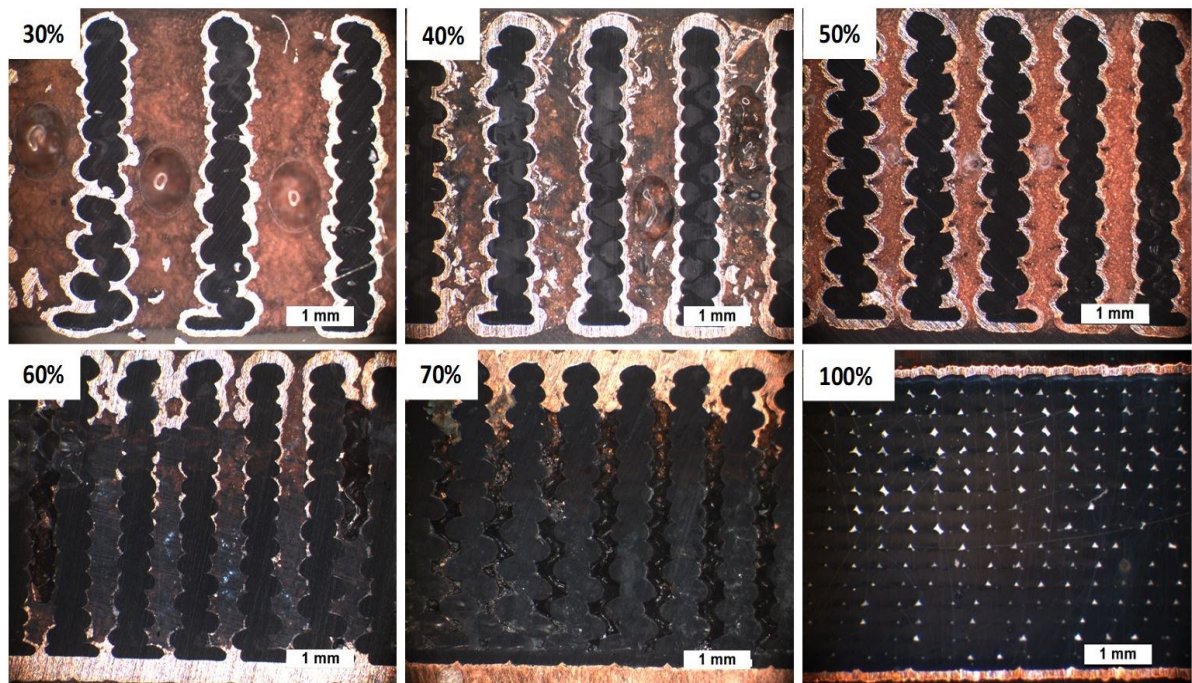


*Figure 56. Cross-section of plated laminates at different infill density percentage*



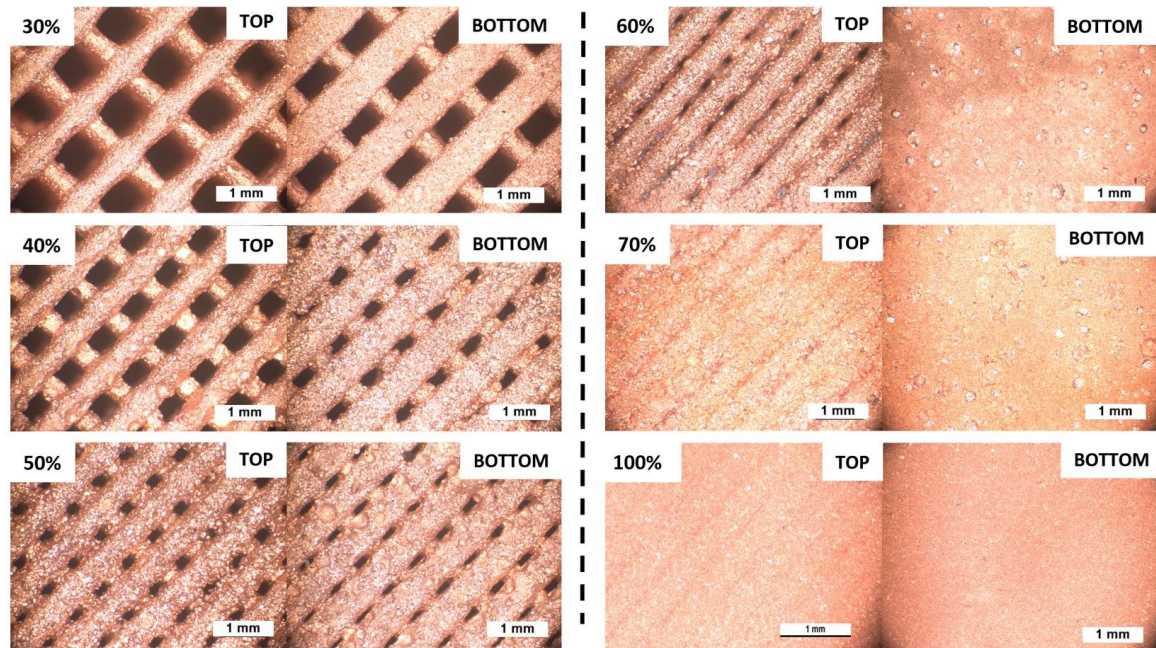


Figure 57. Top and bottom surface of plated laminates at different infill density percentage

From Fig. 57, the closing of the gaps between two beads starts with the plated laminate at 50% infill density. This effect is more present on the bottom of the specimen because the first layer is slightly flattened to better adhere to the plate and to avoid problems during printing. Concerning infill density from 30% up to 70%, the deposited copper at the outer surfaces of the sample is thicker as the infill increase, especially at the base. During the electroplating process, a control in current has been applied, thus the current remains constant. The current doesn't change even when some internal surfaces are no longer reachable, due to the closing of some gaps during plating. Therefore, the remaining surfaces that can be plated, are subjected to a current intensity greater than the rated current of  $10\text{mA}/\text{cm}^2$ . This leads to an increase in thickness of the deposited copper in this surface more than 0.1mm. For this reason, as the infill grows, more and more copper is deposited on the external surface rather than inside, away from the neutral axis, increasing the mechanical properties accordingly. This copper distribution is clearly visible from the comparison with 100% infill density in Fig. 56.

For all plated laminates, except that at 100% infill, there is a deposited copper weight of about 11.5g which is greater than the weight of the as-printed specimen. The mechanical properties are reported in Tab. 20. As the infill density increases, mechanical properties in terms of rigidity, maximum load, and displacement at break increase, with the exception of the displacement at break in the laminate at 100% infill density. Increasing the infill

---

density, also if the results are normalized with respect to the weight, the mechanical properties increase (Tab. 19). From 30% to 70% infill, both the rigidity and the maximum load increase from 93N/mm to 225N/mm and from 79N to 205N, respectively. The increase in mechanical properties is more than proportional to the increase in weight, but this is also due to an inhomogeneous distribution of copper.

#### **6.4 Conclusions**

3D-printed parts have lower mechanical properties than parts made of aluminum or steel, but there are some techno-polymers loaded with high-content of carbon fiber that can be very interesting from the mechanical point of view. In particular, in metal replacement these materials can offer a better strength-to-weight ratio than aluminum but they are extremely expensive. To improve the mechanical and other properties of an unfilled and cheaper material, a novel post-processing method, has been successfully developed. This procedure consists of two phases: pre-treatment to make conductive the part and electroplating process to deposit a layer of copper. The post-process method increases electrical, thermal and mechanical, but only the latter has been presented. All laminates have a significant increase in stiffness and strength due to the deposited copper layer, both in the rigidity and in the maximum load, while the displacement at break decreases. The object can be printed with a certain infill density based on the desired mechanical properties, which in turn depend on the type of application.

However, this process has some limitations, such as dimensional tolerances, due to the plated copper layer, that can be variable and must be foreseen in the project phase. Depending on the thickness of the copper layer, this process can take many hours and it requires an operator. Another disadvantage is the significant increase in weight compared to 3D printed laminate, especially for small part.

There are also future works that need to be further investigated both at the method and printing level. Regarding the method, the use of different additives such as leveling agent, nucleating agent, and brightening can be investigated. A better knowledge of the position between the anodes and the cathodes to have a more uniform plating should be studied.

Instead at the printing level, it should be interesting to investigate the enhancement of the mechanical properties varying not only the infill density but also the infill pattern. Nevertheless, this can be considered a promising starting point for the development of a new post-processing method.

## CHAPTER VII

### 7. GENERAL CONCLUSIONS AND FUTURE PERSPECTIVES

The aim of this thesis has been to investigate the mechanical properties of 3D-printed objects and find new solutions to increase stiffness and strength. The work has been developed in several phases.

As a first step during the first year, a large experimental 3D printer has been built with a build volume of 700mm x 700mm x 900mm in X, Y, and Z, respectively. Some samples have been printed using this printer with an accuracy of 0.1mm and a speed of 25mm/s. This printer is still being developed and the next step will be the assembly of a pellet extruder, to ensure a wider range of materials to print.

Next, the mechanical properties of 3D-printed semi-crystalline PLA parts in bending have been studied, focusing on geometric processing parameters such as bead section. The samples have been printed using a large-scale 3D printer fed with polymer pellets, using different nozzle diameters ranging from 3 mm up to 8 mm. In this way, keeping all the printing parameters constants, except the bead width and height, different thermal histories within the 3D-printed part have been found. These thermal histories have been measured at three different locations, they are not trivial and consist of alternating heating and cooling steps. Thermal history depends not only on the bead volume but also on other process parameters and on the external environment. Thanks to these different thermal histories, samples with different internal distributions of the degree of crystallinity in the transversal cross-section have been obtained. Such differences in crystallinity distribution have a direct consequence on the mechanical properties. In particular, the more crystalline material appears to be stiffer but also more brittle and less strong. Different behavior in terms of mechanical properties can be found if an amorphous material is used and can be the subject of future developments.

Then, Young's modulus and strength of 3D-printed parts with PLA filled with wood have been tested in simple tension and successfully modeled by CLT coupled with ULF. The mechanical properties of two quasi-isotropic laminates have been calculated and are in good agreement with the measured ones. If the contour lines correction is applied, Young's modulus and strength have a maximum deviation of 4 and 11%, respectively. A further development would be to test the laminates in bending, considering also the interlaminar stresses.

There are many process parameters in the 3D printing slicing software that can be changed but despite their optimization, mechanical properties compared to parts obtained by injection molding cannot be achievable. This is due to the inevitable presence of voids and poor filament-to-filament welding properties. For this reason, in the last part of the work, two novel post-processing methods have been developed and tested.

The first technique consists of two phases, compaction and remelting within a mold made of fine salt. This method has been applied to 3D-printed wood flour-filled polyester parts. The influence of this novel method has been investigated based on Young's modulus and tensile strength. The strength increased in all specimens except for the  $[0]_8$  laminate. An enhancement of the quality of bead-to-bead welding has been found. Compared with the as-built 3D-printed part, Young's modulus and strength can increase up to 270% and 380%, respectively. This method has some limitations such as dimensional distortion and a reduction in the thickness of the sample proportional to eliminated voids.

The second novel post-processing method consists of two phases, pre-treatment to make the part conductive and the electroplating process to deposit a layer of copper. This technique has been applied to 3D-printed ABS samples at different infill raster angle and density. To evaluate the effectiveness of this method, mechanical properties in bending have been measured. Compared to the as-printed part there is a significant increase in rigidity and maximum load in all the samples considered. The object can be printed with a certain infill density based on the desired mechanical properties, which in turn depend on the type of application. However, this process has some limitations, such as dimensional tolerances, due to the inhomogeneous plated copper layer. Depending on the thickness of the copper layer, this process requires an operator, can take many hours, and significantly increases the weight compared to 3D-printed laminate, especially for a small part.

Both of these two novel methods are very interesting, as they greatly increase the mechanical properties compared to as-printed parts, but both have some defects. In this regard, future works of research and development would be necessary to standardize and improve them.

## REFERENCES

- [1] V. Mazzanti, L. Malagutti and F. Mollica, "FDM 3D printing of polymers containing natural fillers: a review of their mechanical properties," *Polymers*, vol. 11, p. 1094, 2019.
- [2] I. International, " Additive Manufacturing – General principles – Terminology," 2021.
- [3] T. D. Ngo, A. Kashani, G. Imbalzano, K. Nguyen and D. Hui, "Additive manufacturing (3D printing): A review of materials, methods, applications and challenges," *Compos. B Eng.*, vol. 143, pp. 172-196, 2018.
- [4] K. V. Wong and A. Hernandez, "A review of additive manufacturing," *ISRN Mechanical engineering*, pp. 1-10, 2012.
- [5] B. Berman, "3-D printing: The new industrial revolution," *Business horizons*, pp. 155-162, 2012.
- [6] S. Wilkinson and N. Cope, "3D Printing and Sustainable Product Development," *Green Information Technology*, Vols. 161-183, 2015.
- [7] I. Gibson, D. Rosen and B. Stucker, "Additive Manufacturing Technologies: 3D Printing, Rapid Prototyping, and Direct Digital Manufacturing," *Springer*, 2014.
- [8] L. M. Galantucci and G. Percoco, "Experimental study aiming to enhance the surface finish of fused deposition modeled parts," *Manuf. Technol*, vol. 58, pp. 189-192, 2009.
- [9] I. ASTM, "ASTM F2792-10 Standard Terminology for Additive Manufacturing Technologies," 2010.
- [10] R. Dermanaki and M. Dubé, "Printing polymer nanocomposites and composites in three Dimensions," *Adv. Eng. Mater*, pp. 1700539-1700547, 2017.
- [11] C. Weller, R. K. Frank and T. Piller, "Economic implications of 3D printing: Market structure models in light of additive manufacturing revisited," *Int. J. Production Economics*, vol. 164, pp. 43-56, 2015.
- [12] M. Gebler and C. Visser, "A global sustainability perspective on 3D printing technologies," *Energy Policy*, vol. 74, pp. 158-167, 2014.
- [13] R. Gibson, *Principles of composite materials mechanics.*, CRC Press, 2016.
- [14] B. D. Agarwal, L. Broutman and K. Chandrashekhara, *Analysis and Performance of Fiber Composites*, Wiley, 2017.
- [15] T. Campbell, C. Williams, O. Ivanova and B. Garrett, "Could 3D Printing Change the World? Technologies, Potential, and Implications of Additive Manufacturing," *Atlantic Council*, 2011.

- 
- [16] M. Behzadnasab and A. A. Yousefi, "Effects of 3D printer nozzle head temperature on the physical and mechanical properties of PLA based product," *12th International seminar on polymer science*, pp. 3-5, 2016.
- [17] R. Matsuzaki, M. Ueda, M. Namiki, T. Jeong, H. Asahara, Horiguchi and H. Y. K., "Three-dimensional printing of continuous-fiber composites by in-nozzle impregnation," *Sci. Rep.*, vol. 6, p. 23058, 2016.
- [18] A. Torrado, D. Roberson and R. Wicker, "Fracture Surface Analysis of 3D-Printed Tensile," *J. Fail. Anal. Prev.*, vol. 14, pp. 343-353, 2014.
- [19] O. Mohamed, S. Masood and J. Bhowmik, "Optimization of fused deposition modeling process parameters: a review of current research and future prospects," *Adv. Manuf.*, vol. 3, pp. 42-52, 2015.
- [20] Y. P. Shaik, J. Schuster and A. Shaik, "A Scientific Review on Various Pellet Extruders Used In 3D," *Open Access Libr.*, vol. 8, pp. 1-19, 2021.
- [21] A. K. Gupta and M. Taufik, "Effect of process variables on performances measured in filament and pellet based extrusion process," *Mater. Today*, 2021.
- [22] R. B. Kristiawan, F. Imaduddin, D. Ariawan, Ubaidillah and Z. Arifin, "A review on the fused deposition modeling (FDM) 3D printing: Filament processing, materials, and printing parameters," *Open Eng.*, pp. 639-649, 2021.
- [23] H. Giles, E. M. Mount and J. R. Wagner, *Extrusion: The Definitive Processing Guide and Handbook*, Elsevier Science, 2008.
- [24] G. Alaimo, S. Marconi, L. Costato and F. Auricchio, "Influence of meso-structure and chemical composition on FDM3D-printed parts," *Composites Part B: Engineering*, pp. 371-380, 2017.
- [25] Q. He, H. Wang, K. Fu and L. Ye, "3D printing continuous CF/PA6 composites: effect of microscopic voids on mechanical performance," *Compos. Sci. Technol.*, vol. 191, p. 108077, 2020.
- [26] L. Malagutti, V. Mazzanti and F. Mollica, "Tensile properties of FDM 3D printed wood flour filled polymers and mathematical modeling through classical lamination theory," *Rapid Prototyp. J.*, vol. 28, 2022.
- [27] P. D. Kulkarni and D. Dutta, "Deposition strategies and resulting part stiffnesses in fused deposition modeling," *J. Manuf. Sci. Eng.*, vol. 121, pp. 93-103, 1999.
- [28] G. F. Rodriguez, J. P. Thomas and J. E. Renaud, "Mechanical behavior of acrylonitrile butadiene styrene fused deposition materials," *Rapid Protot. J.*, vol. 9, pp. 219-230, 2003.
- [29] G. F. Rodriguez, J. P. Thomas and J. E. Renaud, "Mechanical behavior of acrylonitrile butadiene styrene (ABS) fused deposition materials. Experimental investigations," *Rapid Protot. J.*, vol. 7, pp. 148-158, 2001.
- [30] L. Li and Q. Sun, "Composite modeling and analysis for fabrication of FDM prototypes with locally controlled properties," *J. Manuf. Process*, vol. 4, pp. 129-141, 2002.
-

- 
- [31] G. W. Melenka and J. S. Schofield, "Evaluation of dimensional accuracy and material properties of the MakerBot 3D desktop printer," *Rapid Protot. J.*, vol. 21, pp. 618-627, 2015.
- [32] M. Somireddy, C. W. Singh and A. Czekansky, "Mechanical behavior of 3D printed composite parts with short carbon fiber reinforcement," *Eng. Fail. Anal.*, vol. 107, p. 104232, 2020.
- [33] J. Y. Choi and M. T. Kortschot, "Stiffness prediction of 3D printed fiber-reinforced thermoplastic composite," *Rapid Prototyp. J.*, vol. 26, pp. 549-555, 2020.
- [34] L. Pyl, K. A. Kalteremidou and D. Hemelrijck, "Exploration of specimen geometry and tab configuration for tensile testing exploiting the potential of 3D printing free form shape continuous carbon fibre – reinforced nylon matrix composite," *Polym. Test.*, vol. 71, pp. 318-328, 2018.
- [35] E. Polyzos, A. Katalagianakis, D. Polyzos, D. Hemelrijck and L. Pyl, "A multi-scale analytical methodology for the prediction of mechanical properties of 3D-printed materials with continuous fibers," *Addit. Manuf.*, vol. 36, p. 101394, 2020.
- [36] G. W. Melenka, B. K. Cheunga, J. S. Schofield, M. R. Dawson and J. P. Carey, "Evaluation and prediction of the tensile properties of continuous fiber-reinforced 3D printed structures," *Compos. Struct.*, vol. 153, pp. 866-875, 2016.
- [37] P. K. Mishra and P. Senthil, "Prediction of in-plane stiffness of multi-material 3D printed laminate parts fabricated by FDM process using CLT and its mechanical behavior under tensile load," *Mater. Today Commun.*, vol. 23, p. 100955, 2020.
- [38] A. K. Sooda, R. K. Ohdarb and S. S. Mahapatrac, "Parametric appraisal of mechanical property of fused deposition modelling processed parts," *Mater. Des.*, vol. 31, pp. 287-295, 2010.
- [39] J. M. Chacón, M. A. Caminero, E. García-Plaza and P. J. Núñez, "Additive manufacturing of PLA structures using fused deposition modelling: Effect of process parameters on mechanical properties and their optimal selection," *Mater. Des.*, vol. 124, pp. 143-157, 2017.
- [40] L. Yang, S. Li, Y. Li, Y. Mingshun and Q. Yuan, "Experimental Investigations for Optimizing the Extrusion Parameters on FDM PLA Printed Parts," *J. Mater. Eng. Perform.*, vol. 28, 2018.
- [41] D. Popescu, A. Zapciu, C. Amza, F. Baciuc and R. Marinescu, "FDM process parameters influence over the mechanical properties of polymer specimens: A review," *Polym. Test.*, vol. 69, pp. 157-166, 2018.
- [42] M. Samykano, "Mechanical Property and Prediction Model for FDM 3D Printed Polylactic Acid (PLA)," *Arab. J. Sci. Eng.*, vol. 46, p. 7875–7892, 2021.
- [43] C. G. Schirmeister, T. Hees, E. H. Licht and R. Mülhaupt, "3D printing of high density polyethylene by fused filament fabrication," *Addit. Manuf.*, vol. 28, pp. 152-159, 2019.
- [44] C. M. Vicente, T. S. Martins, M. Leite, A. Ribeiro and L. Reis, "Influence of fused deposition modeling parameters on the mechanical properties of ABS parts," *Polym. Adv. Technol.*, vol. 31, pp. 1-7, 2019.
- [45] J. Triyono, H. Sukanto, R. M. Saputra and D. F. Smaradhana, "The effect of nozzle hole diameter of 3D printing on porosity and tensile strength parts using polylactic acid material,"

---

*Open Eng.*, vol. 10, pp. 762-768, 2020.

- [46] J. M. Chacón, M. Á. Caminero, P. J. Núñez, E. García-Plaza and J. P. Bécar, "Effect of nozzle diameter on mechanical and geometric performance of 3D printed carbon fibre-reinforced composites manufactured by fused filament fabrication," *Rapid Prototyp. J.*, 2021.
- [47] V. E. Kuznetsov, A. N. Solonin, O. D. Urzhumtsev, R. Schilling and A. G. Tavitov, "Strength of PLA Components Fabricated with Fused Deposition Technology Using a Desktop 3D Printer as a Function of Geometrical Parameters of the Process," *Polymers*, vol. 10, 2018.
- [48] L. Wang, W. M. Gramlich and D. J. Gardner, "Improving the impact strength of Poly(lactic acid) (PLA) in fused layer modeling (FLM)," *Polymer*, vol. 114, pp. 242-248, 2017.
- [49] Y. Liao, C. Liu, B. Coppola, G. Barra, L. Di Maio, L. Incarnato and K. Lafdi, "Effect of Porosity and Crystallinity on 3D Printed PLA Properties," *Polymers*, vol. 11, p. 1487, 2019.
- [50] L. A. Northcutt Sara, V. Orski Kalman, B. Migler and A. P. Kotula, "Effect of processing conditions on crystallization kinetics during materials extrusion additive manufacturing," *Polymer*, vol. 154, pp. 182-187, 2018.
- [51] R. Vadori, A. K. Mohanty and M. Misra, "The Effect of Mold Temperature on the Performance of Injection Molded Poly(lactic acid)-Based Bioplastic," *Macromol. Mater. Eng.*, vol. 298, pp. 981-990, 2013.
- [52] A. M. Forster, "Materials Testing Standards for Additive Manufacturing of Polymer Materials: State of the Art and Standards Applicability," *NISTIR 8059*, 2015.
- [53] M. Bayart, M. R. Foruzanmehr, P. Y. Vuillaume, P. Ovlaque, M. Robert and S. Elkoun, "Poly(lactic acid)/flax composites: effect of surface modification and thermal treatment on interfacial adhesion, crystallization, microstructure, and mechanical properties," *Compos. Interfaces*, vol. 29, pp. 17-36, 2022.
- [54] G. Perego, G. D. Cella and C. Bastioli, "Effect of Molecular Weight and Crystallinity on Poly(lactic acid) Mechanical Properties," *J. Appl. Polym. Sci.*, vol. 59, pp. 37-43, 1996.
- [55] M. Somireddy, C. V. Singh and A. Czekansky, "Analysis of the material behavior of 3D printed laminates via FFF," *Exp. Mech.*, vol. 59, pp. 871-881, 2019.
- [56] H. Gonabadi, A. Yadav and S. J. Bull, "The effect of processing parameters on the mechanical characteristics of PLA produced by a 3D FFF printer," *Int. J. Adv. Manuf. Technol.*, vol. 111, pp. 695-709, 2020.
- [57] M. P. Dicker, P. F. Duckworth, A. B. Baker, G. Francois, M. K. Hazzard and P. M. Weaver, "Green composites: a review of material attributes and complementary applications," *Composites Part A*, vol. 56, pp. 280-289, 2014.
- [58] V. Mazzanti, L. Malagutti, A. Santoni, F. Sbardella, A. Calzolari, F. Sarasini and F. Mollica, "Correlation between Mechanical Properties and Processing Conditions in Rubber-Toughened Wood Polymer Composites," *Polymers*, vol. 12, p. 1170, 2020.
- [59] C. Tosto, L. Saitta, E. Pergolizzi, I. Blanco, G. Celano and G. Cicala, "Methods for the characterization of polyetherimide based materials processed by fused deposition



- 
- modelling," *Applied Sciences*, vol. 10, p. 3195, 2020.
- [60] S. H. Ahn, M. Montero, D. Odell, S. Roundy and P. K. Wright, "Anisotropic material properties of fused deposition modeling ABS," *Rapid Prototyp J.*, vol. 8, pp. 248-257, 2002.
- [61] J. Giri, A. Chiwande, Y. Gupta, C. Mahatme and P. Gir, "Effect of process parameters on mechanical properties of 3d printed samples using FDM process," *Mater. Today*, vol. 47, pp. 5856-5861, 2021.
- [62] J. Dong, C. Mei, J. Han, S. Lee and Q. Wu, "3D printed poly(lactic acid) composites with grafted cellulose nanofibers: Effect of naofiber and post-fabrication annealing treatment on composite flexural properties," *Addit. Manuf.*, vol. 28, pp. 621-628, 2019.
- [63] S. Bhandaria, R. A. Lopez-Anidoa and D. J. Gardnera, "Enhancing the interlayer tensile strength of 3D printed short carbon fiber reinforced PETG and PLA composites via annealing," *Addit. Manuf.*, vol. 30, p. 100922, 2020.
- [64] N. Yu, X. Sun, Z. Wang, D. Zhang and J. Li, "Effects of auxiliary heat on the interlayer bonds and mechanical performance of polylactide manufactured through fused deposition modeling," *Polym. Test.*, vol. 104, p. 107390, 2021.
- [65] J. Torres, J. Coteló, J. Karl and P. Gordon, "Mechanical Property Optimization of FDM PLA in Shear with Multiple Objectives," *Miner. Met. Mater. Ser.*, vol. 67, 2015.
- [66] J. Butt and R. Bhaskar, "Investigating the Effects of Annealing on the Mechanical Properties of FFF-Printed Thermoplastics," *J. Manuf. Mater. Process*, vol. 4, p. 38, 2020.
- [67] V. Slavković, N. Grujović, A. Dišić and A. Radovanović, "Influence of Annealing and Printing Directions on Mechanical Properties of PLA Shape Memory Polymer Produced by Fused Deposition Modeling," *International Congress of Serbian Society of Mechanics*, 2017.
- [68] R. A. Wach, P. Wolszczak and A. Adamus-Włodarczyk, "Enhancement of Mechanical Properties of FDM-PLA Parts via Thermal Annealing," *Macromol. Mater. Eng.*, vol. 303, 2018.
- [69] A. Chalgham, A. Ehrmann and I. Wickenkamp, "Mechanical Properties of FDM Printed PLA Parts before and after Thermal Treatment," *Polymers*, vol. 13, p. 1239, 2021.
- [70] K. R. Hart, R. M. Dunn, J. M. Sietins, C. M. Hofmeister Mock, M. E. Mackay and E. D. Wetze, "Increased fracture toughness of additively manufactured amorphous thermoplastics," *Polymer*, vol. 211, p. 123091, 2018.
- [71] S. Singh, M. Singh, C. Prakash, M. K. Gupta, M. Mia and R. Singh, "Optimization and reliability analysis to improve surface quality and mechanical characteristics of heat-treated fused filament fabricated parts," *Int. J. Adv. Manuf. Technol.*, 2019.
- [72] K. S. Kumar, R. Soundararajan, G. Shanthosh, P. Saravanakumar and M. Ratteesh, "Augmenting effect of infill density and annealing on mechanical properties of PETG and CFPETG composites fabricated by FDM," *Mater. Today: Proceedings*, vol. 45, pp. 2186-2191, 2021.
- [73] M. S. Srinidhi, R. Soundararajan, K. S. Satishkumar and S. Suresh, "Enhancing the FDM infill pattern outcomes of mechanical behavior for as-built and annealed PETG and CFPETG
-

- 
- composites parts," *Mater. Today: Proceedings*, vol. 45, pp. 7208-7212, 2021.
- [74] E. R. Fitzharris, I. Watt, D. W. Rosen and M. L. Shofner, "Interlayer bonding improvement of material extrusion parts with polyphenylene sulfide using the Taguchi method," *Addit. Manuf.*, vol. 24, pp. 287-297, 2018.
- [75] A. Szust and G. Adamaski, "Using thermal annealing and salt remelting to increase thermal properties of 3D FDM prints," *Eng. Fail. Anal.*, vol. 132, p. 105932, 2022.
- [76] A. Equbal, N. K. Dixit and A. K. Sood, "Electroless Plating on Plastic," *Int. j. sci. eng. res.*, vol. 8, pp. 12-18, 2013.
- [77] X. Tang, J. Wang, C. Wang and B. Shen, "A novel surface activation method for Ni/Au electroless plating of acrylonitrile-butadiene-styrene," *Surf. Coat. Technol.*, vol. 206, pp. 1382-1388, 2011.
- [78] S. Olivera, H. B. Muralidhara, K. Venkatesh, K. Gopalakrishna and C. S. Vivek, "Plating on acrylonitrile-butadiene-styrene (ABS) plastic: a review," *J. Mater. Sci*, vol. 51, 2016.
- [79] M. Bazzaoui, J. I. Martins, E. A. Bazzaoui, A. M. Albourine and P.-D. Hong, "A simple method for acrylonitrile butadiene styrene metallization," *Surf. Coat. Technol.*, pp. 71-76, 2013.
- [80] J. J. Kelly, C. Tian and A. C. West, "Leveling and Microstructural Effects of Additives for Copper Electrodeposition," *J. Electrochem. Soc.*, vol. 146, pp. 2540-2545, 1999.
- [81] T. W. Zeng and S. C. Yen, "Effects of Additives in an Electrodeposition Bath on the Surface Morphologic Evolution of Electrodeposited Copper," *Int. J. Electrochem. Sci.*, 2021.
- [82] D. W. Oxtoby, H. P. Gillis and L. J. Butler, *Chimica Moderna*, Edises, 2017.
- [83] S. Machida and S. Miyata, "Chemical Synthesis of Highly Electrically Conductive Polypyrrole," *Synth. Met.*, vol. 31, pp. 311-318, 1989.
- [84] C. Zhenpeng, C. Coletta, A. Dazzi, P. Lefrancois, M. Gervais, J. Neron and S. Remita, "Radiolytic Method as a Novel Approach for the Synthesis of Nanostructured Conducting Polypyrrole," *Langmuir*, vol. 30, 2014.

## APPENDIX A

Printer-specific configuration files for main board Duet 3 6HC:

### Config.g

; Configuration file for Duet 3

; executed by the firmware on start-up

; General preferences

G90 ; send absolute coordinates...

M83 ; ...but relative extruder moves

M550 P"Duet 3" ; set printer name

; Drives

M569 P0 S1 ; physical drive 0 goes forwards --> axis X1

M569 P5 S1 ; physical drive 5 goes forwards --> axis X2

M569 P1 S0 ; physical drive 1 goes backwards --> axis Z1

M569 P4 S0 ; physical drive 4 goes backwards --> axis Z2

M569 P2 S1 ; physical drive 2 goes forwards --> axis Y

M569 P3 S0 ; physical drive 3 goes backwards --> Extruder

M584 X0:5 Y2 Z1:4 E3 ; set drive mapping from driver 0 to 6

M671 X-502.5:502.5 Y-502.5:502.5 S50 ; Z-screw locations left / right

M350 X16 Y16 Z16 E16 I1 ; configure microstepping with interpolation

M92 X320 Y320 Z320 E476.5 ; set steps per mm

M566 X1500 Y1500 Z120 E1500 ; set maximum instantaneous speed changes  
(mm/min)

M203 X3000 Y3000 Z200 E3000 ; set maximum speeds (mm/min)

M201 X800 Y800 Z800 E800 ; set accelerations (mm/s<sup>2</sup>)

M906 X2000 Y2000 Z2000 E1000 I30 ; set motor currents (mA) and motor idle factor

M84 S30 ; Set idee timeout

; Axis Limits

M208 X-487 Y-326 Z0 S1 ; set axis minima

M208 X450 Y312 Z800 S0 ; set axis maxima

; Endstops :

; x1 x2

M574 X1 S1 P"!io0.in+!io1.in" ; configure active-high endstop for low end

; y

M574 Y1 S1 P"!io2.in" ; configure active-high endstop for low end

; z1 z2

;M574 Z1 S2 P"!io3.in+!io4.in" ; configure active-high endstop for low end

M574 Z1 S2

; Z-Probe

M950 S0 C"io5.out" ; create servo pin 0 for BLTouch

M558 P9 C"^io5.in" H5 F120 T6000 ; set Z probe type to bltouch

G31 P500 X20 Y-20 Z0.2 ; set Z probe trigger value, offset and trigger height

M557 X-100:50 Y-50:120 S60 ; define mesh grid

; Heaters

;bed

M308 S0 P"temp0" Y"thermistor" T100000 B4138 ; configure sensor 0 as thermistor

M950 H0 C"out0" T0 ; create bed heater output on out0 and map it to sensor 0

M307 H0 A96.9 C314.3 D1.8 V24 B0 S1.00 ; enable bang-bang mode for the bed heater

M140 H0 ; map heated bed to heater 0

M143 H0 S120 ; set temperature limit for heater 0 to 120C

---

;Extruder

M308 S1 P"temp1" Y"thermistor" T100000 B4311 ; configure sensor 1 as thermistor

M950 H1 C"out1" T1 ; create nozzle heater output on out1 and map it to sensor 1

M307 H1 B0 S1.00 ; disable bang-bang mode for heater and set PWM limit

M143 H1 S340 ; set temperature limit for heater 1 to 280C

;M308 S2 P"temp2" Y"thermistor" T100000 B4311 ; configure sensor 2 as thermistor

;M950 H2 C"out2" T2 ; create nozzle heater output on out1 and map it to sensor 1

;M307 H2 B0 S1.00 ; disable bang-bang mode for heater and set PWM limit

;M143 H2 S300 ; set temperature limit for heater 1 to 280C

; Fans

M950 F0 C"out7" Q500 ; create fan 0 on pin out7 and set its frequency

M106 P0 S1 H-1 ; set fan 0 value. Thermostatic control is turned off

M950 F1 C"out8" Q500 ; create fan 1 on pin out8 and set its frequency

M106 P1 S1 H-1 ; set fan 1 value. Thermostatic control is turned off

M950 F2 C"out9" Q500 ; create fan 2 on pin out9 and set its frequency

M106 P2 S1 H-1 ; set fan 2 value. Thermostatic control is turned off

; Tools

M563 P0 S"SuperVolcano" D0 H1 F0 ; define tool 0

G10 P0 X0 Y0 Z0 ; set tool 0 axis offsets

G10 P0 R0 S0 ; set initial tool 0 active and standby temperatures to 0°C

---

**Homeall.g**

; called to home all axes

G91 ; relative positioning

M564 S0 H0

G1 Z20 F200

G1 H1 X-99999 F2000 ; move quickly to X axis endstop and stop there (first pass)

G1 H2 X15 F1500 ; go back a few mm

G1 H1 X-99999 F300 ; move slowly to X axis endstop once more (second pass)

G1 H1 Y-9999 F2000 ; move quickly to Y axis endstop and stop there (first pass)

G1 H2 Y15 F1500 ; go back a few mm

G1 H1 Y-9999 F300 ; move slowly to Y axis endstop once more (second pass)

G90

G1 Y0 F2500 ; Go to the center of y axis

G1 X0 F2500 ; Go to the center of x axis --> center of the bed

G30 ; probe bed

G91

G90 ; absolute positioning

**Bed.g**

; called to perform automatic bed compensation via G32

M561 ; clear any bed transform

M401 ; deploy zprobe

G30 P0 X0 Y-50 Z-99999

G30 P1 X0 Y+100 Z-999999 S2

M402

;G29 ; probe the bed and enable compensation

## APPENDIX B

%% MATLAB CODE FOR LASCALA 3D printer robotic arm:

```
clc
clear all
close all

Extruder = 2; %% 2 = 22mm // 1 = 14mm

x_offset      = 1150; %% X_start_offset
y_offset      = 500;  %% Y_start_offset
z_offset      = 0;   %% Z_start_offset

arrive_x      = 1500; %% X_print_finish
arrive_y      = 1500; %% Y_print_finish
arrive_z      = 300;  %% Z_print_finish
Travel_speed  = 1200; %% mm/min
Rapid_movement = 6000; %% mm/min
distance_further_X0 = x_offset - 890; %% move ???mm before 0 --> avoid stringing
into the piece --> si trova alla coordinata x = 890
start_before_Y = 20; %% start ???mm before real position --> prevent lack beads
initial

finish_after_y = 50; %% not lift instantly but move further and then lift
add_brim       = 0; %% add a brim to the first layer
lift_height    = 50; %% lift height after last point of a bead
Z_brush       = 55; %% height_brush
first_brush_offset_Y = 100; %% add length to avoid stringing in the sample in the final
part of bead
last_brush_offset_Y = 50; %% add length to avoid stringing in the sample in the initial
part of bead

line_first_x = 40;
purge_line = 0;
bead_length = 420; %% Bead_distance
bead_width = 13; %% Bead_width
number_line_X = 3; %% Bead_number_in_X_direction
Z_1 = 5.35; %% Z first layer
number_layer = 6; %% Number of layer
Z_height = 2.3; %% Z other layers

Z_max = (Z_1+(number_layer-1)*Z_height); %% Z_max
X_max = (number_line_X-1)*bead_width; %%
Z = Z_1:Z_height:Z_max;
Y = [ 0 bead_length ];
X = 0 : bead_width : X_max;
X = X*-1;

% Build path
MATRIX = zeros(1,6); %%% 1° column = G // 2° F // 3° X // 4° Y // 5° Z // 6° E
count_x = 0;
count_y = 0;
```

---

```

count_z = 0;
Z_start = Z(1);
for z = 1: length(Z)
count_z = count_z + 1;
if z == 1
    brim = add_brim;
else
    brim = 0;
end
for x = 1 : length(X)
    count_x = count_x + 1;

for i = 1 : 7
    scrivi = (count_z-1)*length(X)*7 + (count_x-1)*7 + i;
    if i == 1
        MATRIX(scrivi,1) = 0;
        MATRIX(scrivi,2) = Rapid_movement;
        MATRIX(scrivi,3) = X(x);
        MATRIX(scrivi,4) = Y(1)-start_before_Y-brim;
        MATRIX(scrivi,5) = Z_brush;
    end
    if i == 2
        MATRIX(scrivi,1) = 0;
        MATRIX(scrivi,2) = Rapid_movement;
        MATRIX(scrivi,3) = X(x);
        MATRIX(scrivi,4) = Y(1)-start_before_Y-brim;
        MATRIX(scrivi,5) = Z(count_z);
    end
    if i == 3
        MATRIX(scrivi,1) = 1;
        MATRIX(scrivi,2) = Travel_speed;
        MATRIX(scrivi,3) = X(x);
        MATRIX(scrivi,4) = Y(2)+brim;
        MATRIX(scrivi,6) = 1000;
    end
    if i == 4
        MATRIX(scrivi,1) = 0;
        MATRIX(scrivi,2) = Rapid_movement;
        MATRIX(scrivi,3) = X(x);
        MATRIX(scrivi,4) = Y(2) +brim + finish_after_y;
        MATRIX(scrivi,5) = Z(count_z);
    end
    if i == 5
        MATRIX(scrivi,1) = 0;
        MATRIX(scrivi,2) = Rapid_movement;
        MATRIX(scrivi,3) = X(x);
        MATRIX(scrivi,4) = Y(2)+brim+ finish_after_y;
        MATRIX(scrivi,5) = Z(count_z) + lift_height;
    end
    if i == 6
        MATRIX(scrivi,1) = 0;

```

---



---

```

MATRIX(scrivi,2) = Rapid_movement;
MATRIX(scrivi,3) = -distance_further_X0;
MATRIX(scrivi,4) = Y(2)+brim+ finish_after_y+first_brush_offset_Y;
MATRIX(scrivi,5) = Z_brush ;
end
if i == 7
MATRIX(scrivi,1) = 0;
MATRIX(scrivi,2) = Rapid_movement;
MATRIX(scrivi,3) = -distance_further_X0;
MATRIX(scrivi,4) = Y(1)-start_before_Y-brim-last_brush_offset_Y;
MATRIX(scrivi,5) = Z_brush;
end

end
end
end

non_empty = [];
for i = 1 : size(MATRIX,1)
riga = MATRIX(i,:);
vuoto = find(riga > 0);
if isempty(vuoto) == 0
non_empty = [ non_empty i ];
end
end

GCODE = MATRIX(non_empty,:);
GCODE_initial_0 = [ 0 Rapid_movement -distance_further_X0 (Y(2)+brim+
finish_after_y+first_brush_offset_Y) Z_brush 0 ];
GCODE_initial_1 = [ 0 Rapid_movement -distance_further_X0 (Y(1)-start_before_Y-
brim-last_brush_offset_Y) Z_brush 0 ];

GCODE_line_initial_0 = [ 0 Rapid_movement line_first_x (Y(1)-start_before_Y-
add_brim) Z_brush 0 ];
GCODE_line_initial_1 = [ 0 Rapid_movement line_first_x (Y(1)-start_before_Y-
add_brim) Z_1 0 ];
GCODE_line_initial_2 = [ 1 Travel_speed line_first_x (Y(2)+brim) Z_1 1000
];
GCODE_line_initial_3 = [ 0 Rapid_movement line_first_x (Y(2)+brim+ finish_after_y)
Z_1 0 ];
GCODE_line_initial_4 = [ 0 Rapid_movement line_first_x (Y(2)+brim+ finish_after_y)
Z_1+ lift_height 0 ];
GCODE_line_initial_5 = [ 0 Rapid_movement -distance_further_X0 (Y(2)+brim+
finish_after_y+first_brush_offset_Y) Z_brush 0 ];
GCODE_line_initial_6 = [ 0 Rapid_movement -distance_further_X0 (Y(1)-
start_before_Y-brim-last_brush_offset_Y) Z_brush 0 ];

GCODE_line_INITIAL = [ GCODE_line_initial_0; GCODE_line_initial_1;
GCODE_line_initial_2 ; GCODE_line_initial_3; GCODE_line_initial_4;
GCODE_line_initial_5; GCODE_line_initial_6 ] ;

GCODE_last = [0 Rapid_movement arrive_x-x_offset arrive_y-y_offset arrive_z 0 ];

```

---

---

```

if purge_line == 0
    GCODE = [ GCODE_initial_0; GCODE_initial_1 ; GCODE ; GCODE_last ] ;
else
    GCODE = [ GCODE_initial_0; GCODE_initial_1 ; GCODE_line_INITIAL; GCODE ;
GCODE_last ] ;
end
savePath = './gcode/print_test/'; % Put the string of the path you want to save your file in
Name_save =
append(savePath,'Sample_Y',num2str(bead_length),'mm_X',num2str(number_line_X),'x',n
um2str(bead_width),'mm_Z',num2str(number_layer),'x',num2str(Z_heigth),'mm .gcode');
fileID = fopen(Name_save,'w');

%%% write initial gcode
if Extruder == 2
fprintf(fileID,'T0\n');
else
fprintf(fileID,'T1\n');
end
fprintf(fileID,'M82\n'); %%%absolute extrusion mode
fprintf(fileID,'G28\n'); %%%Homing

%%% ALL THIS COMMAND IS USELESS for software Acquarese

for i = 1 : size(GCODE,1) %%% per tutte le righe del GCODE
    riga = GCODE(i,:);
    if riga(1) == 0
        write = 'G%1.0f F%2.0f X%3.5f Y%4.5f Z%5.5f\n';

fprintf(fileID,write,riga(1),riga(2),riga(3)+x_offset,riga(4)+y_offset,riga(5)+z_offset);
    else
        write = 'G%1.0f F%2.0f X%3.5f Y%4.5f E%6.5f\n';
        fprintf(fileID,write,riga(1),riga(2),riga(3)+x_offset,riga(4)+y_offset,riga(6));
        a = 0;
    end
end

fprintf(fileID,'M82\n'); %%%absolute extrusion mode
fprintf(fileID,'M84\n'); %%%disable stepper motors
fclose(fileID);

```